

Thermo-Hydrodynamics in a Closed Loop Pulsating Heat Pipe

THÈSE N° 6491 (2014)

PRÉSENTÉE LE 18 DÉCEMBRE 2014

À LA FACULTÉ DES SCIENCES ET TECHNIQUES DE L'INGÉNIEUR
LABORATOIRE DE TRANSFERT DE CHALEUR ET DE MASSE
PROGRAMME DOCTORAL EN ENERGIE

ÉCOLE POLYTECHNIQUE FÉDÉRALE DE LAUSANNE

POUR L'OBTENTION DU GRADE DE DOCTEUR ÈS SCIENCES

PAR

Giulia SPINATO

acceptée sur proposition du jury:

Prof. F. Maréchal, président du jury
Prof. J. R. Thome, Dr N. Borhani, directeurs de thèse
Dr B. Agostini, rapporteur
Prof. S. Haussener, rapporteuse
Dr R. Revellin, rapporteur



ÉCOLE POLYTECHNIQUE
FÉDÉRALE DE LAUSANNE

Suisse
2014

“To invent, you need a good imagination and a pile of junk.”
— Thomas Edison

To my parents...

Acknowledgements

I begin by thanking Prof. John R. Thome for providing the opportunity to do this thesis and for his guidance and Dr. Navid Borhani for his encouragement and endorsement during these three years. I would like to thank the Swiss Commission for Technology and Innovation (CTI) and ABB Switzerland Ltd. for the financial support of the project.

I also thank my colleagues at the LTCM and IEL, who have created a great working atmosphere in the ELH 010 Lab. Special thanks to Luca Amalfi for the good time spent together. Moreover, I would like to express my gratitude to Dr. Brian d'Entremont and Dr. Bruno Agostini for their insights and to Mr. Ville Forsström for his advice on image processing questions.

Thanks to the entire staffs of the ATME and AEM workshops for their technical work on the facility, in particular to Laurent Chevalley. Thank you to Cécile Taverney and Nathalie Matthey-de-l'Endroit for taking care of the administrative work.

Finally I thank my parents for their encouragement and support during all these years.

Abstract

Pulsating heat pipes (PHPs) represent a promising solution for passive on-chip, two-phase cooling of micro-electronics, providing advantages such as a simple construction and operation in any gravitational orientation. Unfortunately, the unique coupling of thermodynamics, hydrodynamics and heat transfer responsible for their operation has so far eluded comprehensive description or accurate prediction.

The complexity of the self-sustained two-phase flow in PHPs presents many challenges to the understanding on the physical phenomena taking place. It is important to evaluate the heat and mass transfer mechanisms occurring during their operation in order to better describe their performance as a function of the operating conditions. In the present study, a new facility at the Laboratory of Heat and Mass Transfer (LTCM) was built to allow the synchronized thermal and visual investigation of a Closed Loop Pulsating Heat Pipe (CLPHP).

A single-turn channel CLPHP was investigated using R245fa as the working fluid. The tests were carried out at filling ratios from 10 to 90 % and heat inputs from 2 to 60 W, for vertical and inclined orientation. Flow visualization was attained via the transparent front side of the test section which provided full optical access to the flow inside of the CLPHP channels. A novel time-strip image processing technique was applied to the high speed videos to extract qualitative details of the flow regimes and quantitative flow data concerning the liquid/vapor interface dynamics. Local temperature oscillations were also measured and their frequency spectra further helped in characterizing the self-sustained two-phase flow. Thermal resistance measurements were used to qualitatively and quantitatively assess the effect of the flow dynamics on the system thermal performance, which are presented as '*operational maps*'.

The dynamics governing the PHP operation during oscillating and circulating flows and their effects on the system thermal performance were investigated and insight gained. Four distinct flow regimes and their thermal and flow-dynamics characteristics were identified, suggesting the strong coupling between the two-phase flow pattern and the system thermal behavior. Thin film evaporation was observed to be the most dominant thermal mechanism while heat transfer into the oscillating liquid slug was of second importance, together with localized nucleate boiling. Moreover, the net forces acting on the system could be identified through the novel time-strip technique, revealing new details on the mechanisms producing self-sustained two-phase flow oscillation and circulation, and the two-phase flow pattern transition. The role of gravity for the operation of this single-turn CLPHP was also assessed.

Key words: Closed Loop Pulsating Heat Pipes (CLPHP); flow visualization; time-strip technique; flow pattern; two-phase flow dynamics; thermal performance; evaporation mechanism

Sommario

I *tubi di calore pulsanti* o *condotti termici pulsanti* rappresentano una soluzione dall'ottimo potenziale per il raffreddamento passivo di componentistica micro-elettronica. Tali dispositivi presentano vantaggi in termini di semplicità costruttiva ed inoltre possono essere messi in funzione anche in assenza di gravità. Durante il loro funzionamento le proprietà termodinamiche e fluidodinamiche sono strettamente correlate e la complessità del sistema è tale che una descrizione accurata dei fenomeni alla base del loro funzionamento o accurati metodi predittivi non sono stati ancora introdotti nella letteratura.

La comprensione della fisica del flusso bifase che si produce all'interno del sistema, senza l'ausilio di pompe o altri dispositivi meccanici, presenta molte incognite. Per una corretta comprensione del funzionamento dei condotti termici pulsanti, è importante analizzare i meccanismi di scambio termico e di massa, allo scopo di quantificarne le prestazioni in funzione di prestabilite condizioni operative.

Il comportamento di un tubo di calore pulsante a circuito singolo chiuso è stato investigato sperimentalmente ed analiticamente nella presente tesi. Esperimenti sono stati effettuati utilizzando il fluido frigorifero R245fa con rapporti di riempimento compresi tra 10 e 90 %, differenti inclinazioni del sistema e potenza termica entrante netta tra 2 W e 60 W. Una finestra trasparente permette di visualizzare il flusso all'interno del canale e la tecnica di *'time-strip'* è stata impiegata per l'elaborazione dei video, al fine di individuare e caratterizzare i regimi di flusso ed il moto dell'interfaccia liquido-vapore. Le oscillazioni di temperatura e i relativi spettri di frequenza hanno contribuito alla caratterizzazione del flusso bifase, ed in aggiunta sono state effettuate misure della resistenza termica per stimare l'effetto delle proprietà del flusso sulle prestazioni termiche del sistema.

Le dinamiche che regolano il funzionamento dei condotti termici pulsanti, durante il moto oscillante o circolatorio del fluido al loro interno, ed i relativi effetti sulle prestazioni del sistema, sono state oggetto di studio. Quattro distinti regimi di flusso e le loro caratteristiche termiche e fluidodinamiche sono stati identificati, suggerendo il forte accoppiamento esistente tra la fluidodinamica ed il comportamento termico in tali sistemi. I risultati ottenuti hanno dimostrato come il processo di evaporazione sia governato principalmente dal fenomeno dell'*evaporazione a film sottile* mentre il contributo alla trasmissione di calore della fase liquida e dell'ebollizione sia di minore entità. Le forze in gioco sono state identificate attraverso una nuova tecnica di ispezione, rivelando nuovi dettagli sui meccanismi alla base dei moti oscillatori e unidirezionali. Inoltre, una completa caratterizzazione delle dinamiche transizionali tra i diversi regimi di flusso ed il ruolo della gravità sono stati analizzati in dettaglio.

Parole chiave: Tubo di calore pulsante a circuito chiuso; visualizzazione del flusso; tecnica di *'time-strip'*; regimi di flusso; flusso bifase; prestazioni termiche; evaporazione

Contents

Acknowledgements	i
Abstract (English/Italian)	iii
List of figures	xi
List of tables	xv
1 Introduction	1
Introduction	1
1.1 The need for a paradigm shift	1
1.2 Thermal management of micro-electronics	2
1.3 Objectives of this study	3
1.4 Thesis structure	3
2 State-of-the-art of Pulsating Heat Pipes	5
State-of-the-art of Pulsating Heat Pipes	5
2.1 Introduction	5
2.2 Relative importance of sensible and latent heat exchange in a PHP	6
2.3 Dominant boiling mechanism	6
2.4 PHP operation and thermal performance	9
2.4.1 PHP geometry	9
2.4.2 Orientation with respect to vertical	11
2.4.3 Working fluid	11
2.4.4 Filling Ratio	12
2.5 Flow visualization studies	13
2.5.1 Flow patterns and trends in performance	13
2.6 Two-phase flow dynamics in oscillatory flows	15
2.6.1 Bubble displacement and velocities	15
2.7 Frequency analysis	16
2.8 Conclusions	17
3 Experimental Set-up and Data Reduction	19
Experimental Set-up and Data Reduction	19

Contents

3.1	Introduction	19
3.2	Test facility	19
3.2.1	CLPHP test-section	19
3.2.2	Working fluid and system charging procedure	21
3.2.3	Water circuit	23
3.2.4	Electrical Circuit	24
3.3	Instrumentation and Data Acquisition	24
3.3.1	Data acquisition	24
3.3.2	Instrumentation	25
3.4	Experimental set-up validation and experimental protocol	27
3.4.1	Energy balance	27
3.4.2	High frequency data sampling	27
3.4.3	Experimental protocol	28
3.4.4	Experimental data sets	29
3.5	Data reduction	29
3.5.1	Video sequence processing	29
3.5.2	Thermal Data Processing	34
3.6	Conclusions	35
4	Flow Pattern Results	37
	Flow Pattern Results	37
4.1	Introduction	37
4.2	Flow patterns	37
4.2.1	Evaporator dynamics	38
4.2.2	Condenser dynamics	40
4.3	Flow pattern transition	42
4.3.1	Effect of heat load and filling ratio	42
4.3.2	Effect of system orientation	43
4.4	Flow pattern dynamics	43
4.4.1	Synchronized visual and thermal measurements	43
4.5	Conclusions	44
5	CLPHP Thermo-hydrodynamics	45
	CLPHP Thermo-hydrodynamics	45
5.1	Introduction	45
5.2	Operational maps	45
5.3	Thermal performance and two-phase flow dynamics	47
5.4	Thermo-hydrodynamics in a single-turn CLPHP	50
5.4.1	Frequency analysis	57
5.5	Qualitative analysis of the heat transfer in the evaporator U-turn	58
5.6	Conclusions	63
6	CLPHP Flow dynamics	65

CLPHP Flow dynamics	65
6.1 Introduction	65
6.2 Net forces acting on the two-phase flow in a single-turn CLPHP	65
6.3 Dynamics of the oscillatory two-phase flows	67
6.3.1 Slug flow oscillation	67
6.3.2 Slug flow oscillation measurements	68
6.4 Dynamics of circulating flow and flow reversals	73
6.4.1 Flow reversals	73
6.4.2 Thermal measurements of the flow reversals	73
6.4.3 Local flow direction switch	75
6.4.4 Bubble velocities in the condenser	78
6.5 Gravity and flow pattern transition	81
6.6 Conclusions	81
7 Conclusions and Recommendations	83
Conclusions and Recommendations	83
7.1 Main findings of the present study	84
7.2 Recommendations for future research	86
A Uncertainty analysis	87
A.1 Uncertainty measurement	88
A.2 Uncertainty propagation	89
A.2.1 Electrical Power	89
A.2.2 Heat Load water side	89
A.2.3 Input Heat Load	90
A.2.4 Thermal resistances	90
A.2.5 Image Processing	90
B Prediction of the heat transfer coefficient	93
Bibliography	99
Curriculum Vitae	101

List of Figures

2.1	Measured thermal resistance for different geometries, materials and operating conditions. (a) R123 in a 2 mm copper tube CLPHP at different filling ratios (Khandekar et al., 2003b), (b) R134a in an aluminum flat PHP operated at different orientations (Xu et al., 2006), and (c) Water in 2 x 2 mm cross-section copper flat plate PHP operated at 70 % filling ratio and different orientations (Chien et al., 2011)	8
2.2	Parameters affecting PHP operation and thermal performance	9
2.3	Observed flow patterns and relative thermal performance (Khandekar et al., 2009; Khandekar and Groll, 2003)	14
2.4	Temporal evolution of heat transfer coefficient and flow pattern at different heat inputs (Mameli et al., 2014)	14
2.5	Bubble displacement and velocities for methanol in a multi-turn open loop PHP at 10 W heat load (Xu et al., 2005)	15
2.6	Power spectrum analysis multi-turn CLPHP (Xu and Zhang, 2005)	16
2.7	Power spectra of pressure variation in single loop CLPHP for unidirectional flow (Khandekar et al., 2009)	17
3.1	CLPHP experimental facility	20
3.2	Schematics of test-section	21
3.3	Refrigerant charging line	22
3.4	Water circuit	23
3.5	Electrical circuit	24
3.6	Test-section instrumentation	25
3.7	Test-section thermocouples mount	26
3.8	Energy balance results	27
3.9	Schematics of U-turns	30
3.10	Frame sequence schematics and relative time-strips	32
3.11	Benchmarking of the interface tracking algorithm for oscillating flow	33
3.12	Benchmarking of the interface tracking for circulating flow	34
4.1	Flow Patterns observed in the evaporator section as a function of the net heat input Q_{in} , for $FR = 60\%$ and $\alpha = 0^\circ$	39
4.2	Flow Patterns observed in the condenser section as a function of the net heat input Q_{in} , for $FR = 60\%$ and $\alpha = 0^\circ$	41

List of Figures

4.3	Flow pattern map for CLPHP operating at (a) Vertical Evaporator Down (VED) position $\alpha = 0^\circ$ and (b) at $\alpha = 45^\circ$	42
4.4	Frequency spectra of the high frequency temperature measurements and of the time-strip intensity in the evaporator and condenser for $FR = 60\%$ and $\alpha = 0^\circ$	44
5.1	Flow pattern maps for the CLPHP operating at Vertical Evaporator Down (VED) and $\alpha = 45^\circ$ positions. Thermal performance maps showing R_{ratio} trends for Vertical Evaporator Down (VED) and $\alpha = 45^\circ$ orientations.	46
5.2	Frequency spectra and thermal resistance of the PHP effect versus heat load when operating at $FR = 20\%$ for vertical and inclined operation at $\alpha = 45^\circ$	48
5.3	Frequency spectra and thermal resistance of the PHP effect versus heat load when operating at $FR = 60\%$ for vertical and inclined operation	49
5.4	Resistance of the PHP effect R_{PHP} (a) and dominant frequency component (b) for different inclination angles α and operation at $FR = 60\%$ at 30 and 40 W heat inputs.	50
5.5	Frequency spectra of the high frequency temperature measurements and of the time-strip intensity, and time-averaged temperature of the evaporator and condenser. $FR = 20\%$, $\alpha = 0^\circ$	52
5.6	Frequency spectra of the high frequency temperature measurements and of the time-strip intensity, and time-averaged temperature of the evaporator and condenser. $FR = 20\%$, $\alpha = 45^\circ$	53
5.7	Frequency spectra of high frequency temperature profiles and time-strip intensity, and mean temperature of the evaporator and condenser. $FR = 60\%$, $\alpha = 0^\circ$	54
5.8	Frequency spectra of high frequency temperature profiles and time-strip intensity, and mean temperature of the evaporator and condenser. $FR = 60\%$, $\alpha = 45^\circ$	55
5.9	Single spring-mass-damper system applied to CLPHP. (a) Actual CLPHP, (b) simplified CLPHP assumed to be a straight tube, and (c) Spring-mass-damper system.	57
5.10	Time-strips and local time-averaged heat transfer coefficients (a) and (b) computed for single phase liquid heat transfer $h_l(z)$, two-phase thin film evaporation $h_{film}(z)$, and single-phase vapor $h_v(z)$, and local total heat transfer coefficient $h(z)$ (c) and (d), for operation at $FR = 50\%$, $\alpha = 45^\circ$, $Q_{in} = 38$ W and $FR = 60\%$, $\alpha = 45^\circ$, $Q_{in} = 30$ W.	59
5.11	Average heat transfer coefficient of the single-phase liquid, thin film and single-phase vapor, computed for different heat loads when operating at $FR = 60\%$ and $\alpha = 45^\circ$	61
5.12	Time-strips showing oscillating slug flow with nucleation and growth of bubbles in the liquid slug. (a) $FR = 60\%$, $\alpha = 45^\circ$, $Q_{in} = 44$ W and (b) $FR = 60\%$, $\alpha = 45^\circ$, $Q_{in} = 54$ W	62
6.1	Net gravity producing counter-clockwise circulation (positive momentum) in a single loop CLPHP. White represents the liquid phase and gray vapor	66

6.2	Video images of the two-phase flow distribution in the evaporator U-turn at two different times $t = 0.308$ s (a) and $t = 0.684$ s (b). Time-strip of the oscillating slug flow produced by nucleation and growth of bubbles (c). $FR = 60$ %, $\alpha = 45^\circ$, $Q_{in} = 54$ W.	67
6.3	Effect of heat load on the nucleation and expansion rates for operation at $FR = 50$ %, $\alpha = 45^\circ$. (a) $Q_{in} = 20$ W and (b) 34 W.	68
6.4	Amplitudes of oscillation of a liquid slug in the evaporator U-turn as computed from the time-strip for different operating conditions.	70
6.5	Time-strips with superimposed synchronized evaporator temperature profile and relative frequency spectra for operation at $FR = 50$ %, $\alpha = 45^\circ$, $Q_{in} = 38$ W (a) and $FR = 60$ %, $\alpha = 45^\circ$, $Q_{in} = 54$ W (b)	71
6.6	Amplitudes and frequencies of oscillation of the liquid slug in the evaporator U-turn, as computed from the time-strip for different inclination angles α	72
6.7	(a) Temperature difference ΔT between evaporator and condenser during flow reversal and temperature difference frequency spectra for (b) clockwise and (c) counter-clockwise flow circulation when operating at $FR = 60$ %, $\alpha = 0^\circ$, $Q_{in} = 32$ W	74
6.8	Time-strips for counter-clockwise circulating flow in the condenser with superimposed evaporator temperature T_{evap} (a) and entering the evaporator (b). $FR = 60$ %, $\alpha = 0^\circ$, $Q_{in} = 54$ W	76
6.9	Mean amplitude of the oscillatory flow component in the condenser (red) and mean velocity of rising bubbles in the evaporator inlet \bar{u} (blue), graphically evaluated from the time-strips relative to operation at $FR = 60$ %, $\alpha = 0^\circ$	77
6.10	Frequency spectra of evaporator temperature T_{evap} (a) and of condenser temperature T_{cond} (b) for operation at $FR = 70$ %, $\alpha = 0^\circ$	77
6.11	Average velocity \bar{u} of small (dispersed) bubbles rising the condenser up to the U-turn in circulating flow. (a) Vertical operation ($\alpha = 0^\circ$) and (b) inclined operation ($\alpha = 45^\circ$)	79
6.12	Velocity $u(t)$ of Taylor bubbles rising the condenser up to the U-turn in circulating flow. Time-strips (a)-(c) and relative velocity profile $u(t)$ (d)-(f) for CLPHP operating vertically at 60 % of charge under 40, 50 and 60 W heat input.	80
A.1	Calibration curves for thermocouples (a) and pressure sensor (b)	88
A.2	Temperature measurements under isothermal conditions at 23.5 °C for the condenser (a) and evaporator (b) thermocouples	89

List of Tables

3.1	Test-section specifications	20
3.2	Physical properties of R245fa and R1233zd at $T_{sat} = 20^{\circ} \text{C}$	22
3.3	CLPHP experimental matrix	28
6.1	Dynamics of the oscillating liquid slug: Effect of heat load and filling ratio	69
6.2	Dynamics of the oscillating liquid slug: Effect of inclination angle	72
A.1	Measurement errors of instrumentation	88
A.2	Uncertainty of measured quantities	91

Nomenclature

Roman Symbols

A	Amplitude	
Ca	Capillary number, $\frac{\mu_l u_v}{\sigma}$	[-]
c_p	Isobaric specific Heat	[J/(kg K)]
d	diameter	[m]
f	Frequency	[Hz]
F	force	[N]
FR	Filling Ratio	[-]
g	Gravitational acceleration	[m/s ²]
h	Heat transfer coefficient	[W/(m ² K)]
h	Enthalpy	[J/kg]
I	Current	[A]
I	Time-strip intensity	[-]
k	Thermal conductivity	[W/m K]
k	Spring stiffness	[N/m]
L	Length	[m]
m	mass	[kg]
M	Molar mass	[kg/kmol]
N	Number of turns	[-]
P	Pressure	[Pa]
Q	Heat	[W]
q	Heat flux	[W/m ²]
R	Thermal resistance	[K/W]
Re	Reynolds number, $\frac{\rho u d}{\mu}$	[-]
T	Temperature	[K]
t	Time	[s]

List of Tables

u	Velocity	[m/s]
V	Voltage	[V]
z	Channel coordinate	[mm]

Greek Symbols

α	Inclination angle	[deg]
δ	Uncertainty	
δ	Film Thickness	[m]
Δ	Difference	
μ	Dynamic viscosity	[Pa s]
ρ	Density	[kg/m ³]
σ	Surface tension	[N s/m]

Subscripts

0	Initial
<i>circuit</i>	Electrical circuit
<i>cold</i>	Cooling side
<i>cond</i>	Condenser
<i>crit</i>	Critic
<i>dry</i>	Dry film
<i>el</i>	Electrical
<i>evap</i>	Evaporator
<i>end</i>	End
<i>film</i>	Thin film
<i>g</i>	Gravitational
<i>h</i>	Hydraulic
<i>in</i>	Input
<i>heater</i>	Heater
<i>l</i>	Liquid
<i>loss</i>	Lost to ambient
<i>lv</i>	vaporization
<i>L</i>	Left
<i>min</i>	Minimum
<i>PHP</i>	Pulsating Heat Pipe

<i>R</i>	Right
<i>ratio</i>	Ratio
<i>sat</i>	Saturation
<i>v</i>	Vapor
τ	Frictional

Acronyms

CLPHP	Closed Loop Pulsating Heat Pipe
VED	Vertical Evaporator Down
LF	Low Frequency
LTCM	Laboratory of Heat and Mass Transfer at EPFL
FFT	Fast Fourier Transform
HF	High Frequency
PHP	Pulsating Heat Pipe

1 Introduction

1.1 The need for a paradigm shift

The European energy picture has undergone some major changes in the last years. In 2010 the European Union launched a ten-year growth and job strategy initiative ('Europe 2020') containing, among others, specific targets aimed at reducing greenhouse gas emissions by 20% from 1990 levels (European Commission, 2010). Furthermore, in the next 10 years, 80 civilian nuclear power reactors will be shut down due to operating life or political decisions (World Nuclear Association, 2014). These facts together with the intermittent nature of renewable sources and the depletion of fossil fuels (Shafiee and Topal, 2009) will work to shape the European energy market. The improvement of the energy performance and efficiency of power plants, industrial processes and electronic devices is therefore foreseen.

Recent studies (Dijkstra, 2012) estimate the energy consumption of European data centers will increase to 105 TWh in 2015 from 40 TWh in 2006. It has been acknowledged that energy management in data centers is currently highly inefficient and the energy consumed to run the cooling facility can easily exceed the energy consumed by the computational systems. In a state-of-the-art data center, up to 45 % of the total electrical energy is used for operating the cooling resources (McKinsey, 2008). Integration of new and efficient cooling technologies in data centers has been, in fact, very limited in the past 20 years. The main reason for this being the high hardware cost relative to low energy cost (Beitelmal and Fabris, 2014).

On April 8th, 2014, 3MTM announced the implementation of a fully functional supercomputer developed in collaboration with Intel[®] and SGI[®] that employs a revolutionary *two-phase immersion cooling technology*. According to SGI[®] internal sources, this new technology can reduce the cooling energy costs by 95 % and reduce water consumption used for evaporative cooling in HVAC systems. Moreover, it is 10 times more compact than conventional air cooling and it eliminates the infrastructure and the equipment associated with conventional liquid cooling (Colleen and Stephani, 2014). This proof-of-concept marks time for modern high performance data centers designed to reduce power consumption and thus operating and environmental costs.

1.2 Thermal management of micro-electronics

Historically, the cooling of micro-electronics such as microprocessors, servers and racks in data centers has been the focus of microsystems packaging, while facility-level cooling has been the target of Heating Ventilation and Air Conditioning (HVAC) engineers. With increasing power densities and the need for enhancement of the energy efficiency of cooling systems, a holistic assessment of thermal management across the entire length scale hierarchy is essential (Joshi and Kumar, 2012). Nowadays, it is clear that thermal management of data centers requires coordinated attention to the multiple length scales: From the chip to the data center building going through blade and rack architecture (Zuo et al., 2002).

The majority of servers are currently air-cooled where heat sinks remove the heat from the processor chips and reject it to an outside air stream created through fans or blowers. Newer generation heat sinks for high heat dissipation have a composite construction, which incorporates heat pipes to transport the heat to a fin array. As processor powers increase, the heat sink sizes and cooling air velocities have increased the energy consumption. The high powers and reduced space in servers blades require compact heat removal devices. This has encouraged the exploration and use of liquid cooling for high-performance cooling applications (Joshi and Kumar, 2012).

Recent publications report the development of novel chip cooling technologies, these include microchannel single-phase flow, porous media flow, jet impingement, spray cooling and microchannel two-phase flow (Agostini et al., 2007; Mudawar, 2001). These cooling schemes require a mechanical apparatus (i.e. liquid pump) to push the flow through the cooling circuit with increased operating costs and safety concerns for pump failure and vibration. Passive cooling systems such as *conventional heat pipes*, *two-phase flow thermosyphons* and *pulsating heat pipes*, on the contrary, are thermally driven systems. In other words, the fluid motion is produced by heat provided or removed at a precise location in the device (Japikse, 1973) and no mechanical apparatus is therefore needed to achieve fluid flow and heat transport. Conventional heat pipes can work independent of gravity but they are subject to capillary, boiling and entrainment limits, which restrain the maximum heat input that can be transported (Reay et al., 2014), while thermosyphons are wickless gravity driven systems which can work vertically or in near-vertical orientation.

Pulsating Heat Pipes (PHPs) (Khandekar et al., 2004; Akachi, 1990) present the advantages of simple construction and potentially operation in any orientation. The basic flow mechanism has been observed to be the oscillating movement of the fluid produced by liquid-vapor phase change in a closed tube with a capillary inner size diameter. Self-sustained oscillatory two-phase flow in PHPs is attained as a result of the strong thermo-hydrodynamic coupling which has been observed to affect the operation and the thermal performance of the device (Khandekar et al., 2010; Khandekar and Groll, 2004). However, the complexity of the system is such that many aspects related to its operation and performance appear to be in conflict and so far no comprehensive tools exist for the design of a PHP. Therefore, in order to design

future high performance PHP devices, a deeper fundamental understanding of the transport phenomena occurring in their operation needs to be gained.

1.3 Objectives of this study

Questions emerging from past work on PHPs, pertaining to the mechanisms governing the self-sustained two-phase flow and their thermal behavior, are further investigated and developed here. The current study analyzed a single-turn Closed Loop Pulsating Heat Pipe (CLPHP) machined into a brass plate and charged with R245fa. In this study, a novel experimental approach was developed in order to validate a new measurement technique that allowed the synchronized visual and thermal investigation of the CLPHP.

The objectives of this study were:

- To design, build and validate the experimental facility;
- To implement and improve state-of-the-art flow-visualization techniques in order to extract quantitative information of the two-phase flow phenomena;
- To identify the major flow patterns in terms of two-phase flow characteristics and to evaluate their transitions for vertical and inclined operation;
- To measure the thermal resistance of the device in order to identify the major trends in its thermal performance in relation to the two-phase flow pattern and dynamics, thus identifying the '*sweet-spot*' operating condition;
- To qualitatively analyze the characteristics of the heat transfer in the evaporator;
- To identify the net forces acting during the operation of the single loop CLPHP and to assess the role of gravity;
- To quantitatively characterize the mechanisms producing self-sustained two-phase oscillating and circulating flows;

1.4 Thesis structure

The thesis is comprised of seven chapters: Chapter 2 presents a review of available scientific literature relevant to this study. It includes the important aspects relative to the operation and performance of PHPs which will clarify the rationale and direction of this study. Chapter 3 presents a description of the experimental apparatus and the methods used for the processing of visual and thermal data. The discussion of the results commences in Chapter 4 with a description of the observed flow patterns and continues in Chapter 6 where the thermal performance of the tested single-loop CLPHP are qualitatively and quantitatively assessed in relation to the two-phase flow phenomena. Chapter 5 reports the analysis of the system dynamics during oscillatory and circulating flows. Concluding remarks are reported in Chapter 7.

2 State-of-the-art of Pulsating Heat Pipes

2.1 Introduction

The *Pulsating Heat Pipe* (PHP) was introduced into the literature by Akachi (1990) without clear explanation of its operation. Furthermore, the precise nature of the complex thermal and hydrodynamic interactions from which PHPs derive their motive force is still lacking.

In essence, as reported by Khandekar et al. (2010), the thermo-hydrodynamics of a PHP device is governed by the simultaneous presence of two phases of the working fluid within its internal volume, and mass transfer due to evaporation and condensation. The presence of two phases within the device is ensured by only charging a portion of the device volume with liquid prior to operation. The *self-sustained oscillatory two-phase flow* responsible for efficient heat transfer in a PHP is achieved when a sufficiently high temperature gradient is established between the hot (*evaporator*) and the cold (*condenser*) ends of the device. Simultaneous evaporation and condensation of the working fluid, coupled to non-uniform heating and cooling within the hot and cold sections and uneven distribution of liquid and vapor, produces non-equilibrium pressure conditions which propel the liquid entrapped between vapor plugs and transfer heat from the hot to the cold section (Zhang and Faghri, 2008; Charoensawan et al., 2003).

The total heat transfer provided by a PHP is a combination of latent heat, arising from phase change of the working fluid, and sensible heat exchange. Since these are sensitively linked to the nature of the oscillating two-phase flows present inside operating PHPs, the thermal performance of a PHP is governed by the strong thermo-hydrodynamic couplings existing within a particular device. Therefore, their operation and performance is not only a function of boundary conditions such as geometry, temperature levels, working fluid properties and filling ratio but also the nature of the existing two-phase flow patterns that are in turn linked to the applied heat flux, filling ratio and device inclination (Khandekar and Groll, 2004; Khandekar et al., 2003a). As expected, the large number of degrees of freedom caused by this multi-parametric dependence results in highly non-linear systems that are hard to model or predict.

In this Chapter a comprehensive review of previous PHP investigations found in the literature is presented together with an explanation of the influence of all parameters affecting their operation and thermal performance. A review of past flow visualization studies is also provided as a reference for the present work.

2.2 Relative importance of sensible and latent heat exchange in a PHP

Many previous studies agree that during PHP operation the net heat transfer is a combination of heat exchanged via latent and sensible heat. A number of investigations indicate that the majority of the absorbed/rejected heat is due to sensible heat exchange. For example, mathematical models of oscillating two-phase flow developed by Cheng and Ma (2011), Yuan et al. (2010) and Zhang and Faghri (2002) predict that 90%, 80% and 94.2% of the total heat exchange in their devices was due to sensible heat respectively. Furthermore, Nishio et al. (2002), through optical measurements of the rate of contraction and expansion of Taylor bubbles in their PHP, concluded that less than 15% of the total heat exchange was due to latent heat.

The relative magnitudes of latent and sensible heat transfer depends on the operating conditions of a given device and the nature of the two-phase flow regime present. At low heat fluxes, where liquid slug - vapor plug flow exist, latent heat plays only a marginal role in the total heat transfer. In such flows, whilst the vapor plug is at saturation temperature, the temperature within the liquid slug is not uniform. Thus, due to the thermal inertia of the liquid phase, a finite length of time is required to develop the liquid slug temperature profile as it travels between the hot and the cold zones of the device. This limits the amount of mass transfer due to phase change and thus the proportion of the total heat transfer due to latent heat (Nishio et al., 2002; Khandekar et al., 2003a). However, at higher imposed heat fluxes, where annular flow typically exists in the device, the influence of latent heat increases, thus resulting in better thermal performance of the PHP (Khandekar et al., 2004, 2003b).

2.3 Dominant boiling mechanism

From a review of experimental data available in the literature, it can be concluded that the dominant boiling mechanism in a PHP depends on its operating conditions. In fact, many studies indicate that both *thin film evaporation* and *nucleate boiling* can exist within an operating PHP. In one pertinent study, the effect of heat flux on the dominant boiling mechanism was studied by Lips et al. (2010) during diabatic experiments on a single capillary tube with induced oscillation of the flow at 4Hz and a pressure difference of 0.1 bar. For low heat fluxes the flow was seen to be disturbed by bubble nucleation, while at high heat flux the dominant heat transfer mechanism was thin film evaporation.

2.3. Dominant boiling mechanism

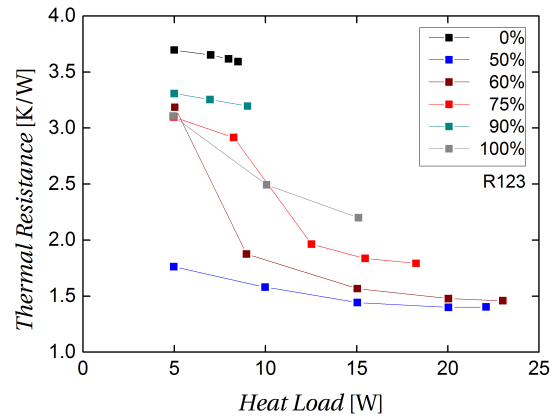
In Tong et al. (2001) the boiling process during vertical gravity assisted operation was described as forced convection boiling. Nucleation sites, activated by local superheating of the evaporator, were visualized in a Pyrex glass tube of 1.8 mm diameter. These nucleated bubbles then rapidly grew in size due to evaporation, thus propelling the liquid slugs through the device. In fact, nucleation of small bubbles in the liquid slug and their subsequent growth has been proven to be important for the start-up and operation of PHP devices. However, in horizontal operation no nucleation could be seen but only rapid coalescence of Taylor bubbles propelling the surrounding liquid.

Similarly, in a 10 turn brass PHP with $1.5 \times 1.5 \text{ mm}^2$ channels, Kim et al. (2003) observed the generation/nucleation of small bubbles in the liquid film which then expanded and coalesced to form Taylor bubbles with increasing heat flux. The resulting flow pattern was described by the author to be similar to the nucleate boiling regime in pool boiling. Furthermore, Khandekar et al. (2003a) utilized flow visualization and thermal measurements to show the transition from nucleate pool boiling to nucleate flow boiling and to convective flow boiling with increasing heat flux input.

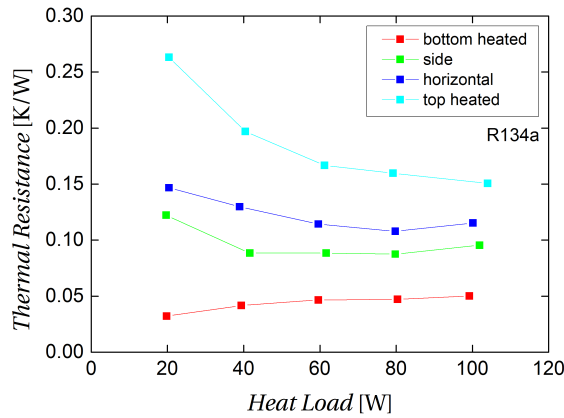
In order to investigate the incidence of nucleation boiling, Qu and Ma (2007) experimentally analyzed the effect of the inner surface roughness. In the presence of rough surfaces (i.e. 20-micron cavities), the start-up of the PHP was observed to be faster since the wall superheating needed by spherical bubbles to grow is smaller than for Taylor bubbles. Nucleation was thus found to be necessary for a prompt start-up of the device and for sustaining flow motion when the evaporator section was filled by liquid. This was in agreement with Cai et al. (2002).

More recently, it has been found that an important contribution to heat transfer due to phase change came from thin film evaporation at the meniscus (Khandekar et al., 2010; Hohmann and Stephan, 2002).

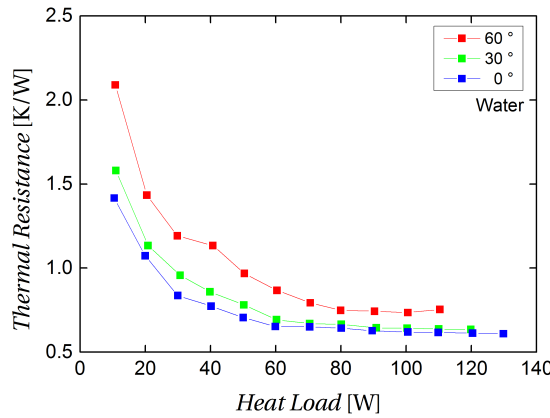
Furthermore, Xu et al. (2005) visualized dispersed bubbles and Taylor bubbles of different length and the combined effect of bubble nucleation, coalescence and condensation was concluded to be responsible for the motion of the two-phase flow and the *local flow direction switch*.



(a)



(b)



(c)

Figure 2.1: Measured thermal resistance for different geometries, materials and operating conditions. (a) R123 in a 2 mm copper tube CLPHP at different filling ratios (Khandekar et al., 2003b), (b) R134a in an Aluminum flat PHP operated at different orientations (Xu et al., 2006), and (c) Water in 2 x 2 mm cross-section copper flat plate PHP operated at 70 % filling ratio and different orientations (Chien et al., 2011).

gravitational buoyancy forces (Zhang and Faghri, 2008):

$$D < D_{crit} = 2\sqrt{\frac{\sigma}{g(\rho_l - \rho_v)}} \quad (2.1)$$

The condition expressed by Eq. 2.1 should guarantee the operation of a PHP at any orientation. However, it has been shown experimentally that the effect of gravity is not insignificant even for tubes of capillary diameter and can affect the mass transfer, the frictional pressure drop and the total liquid inventory (Khandekar et al., 2002a; Xu et al., 2006; Charoensawan et al., 2003; Yang et al., 2008).

The effects of channel diameter were investigated in detail by Wang and Nishio (2005) who observed an improvement in the heat transport rate with increasing channel diameters whilst within the critical limit. Similar trends were observed by Charoensawan et al. (2003), Charoensawan and Terdtoon (2008) and Yang et al. (2008) who measured a 10% enhancement of the thermal performance but lower dry-out heat fluxes in large diameter multi-turn PHPs. Furthermore, Holley and Faghri (2005) numerically assessed the performance of channels whose diameter gradually changed along their length. They concluded that the uneven capillary forces acting on the vapor plugs, coupled with the gradually decreasing frictional forces along the expansion direction, could enhance the overall system performance. In a related study, Chien et al. (2011) tested a system with alternating $2 \times 2 \text{ mm}^2$ and $1 \times 2 \text{ mm}^2$ channels. They found that the unbalanced capillary forces between the different channels triggered flow instabilities, which not only initiated the system operation but also lead to improved performance relative to a device with uniform channel sizes.

Zhang and Faghri (2008) reported on the effects of channel loop geometry on the flow pattern. They found that sharp bends created disturbances which produced stratified or annular flows in the device. Furthermore, at low filling ratios such bends enhanced the heat transport capability of the PHP when operating in gravity assisted mode.

Number of turns

The results presented in the literature tend to conclude that a minimum number of turns is necessary to achieve pulsating flow, and thus system operation, when the device is positioned horizontally (zero gravity) or at top heating modes (negative gravity). This was attributed to the U-turns increasing the degrees of freedom of the system by generating two-phase flow instabilities and pressure perturbations.

Khandekar and Groll (2004) observed that flow oscillations were more pronounced as the number of turns in the PHP channel increased. They also demonstrated that there is an optimum number of turns for a given heat input. Lin et al. (2001) proposed that this critical number of turns N_{crit} was dependent on the dynamic balance between mass, momentum and energy transfer within the existing two-phase flow regime. Charoensawan et al. (2003) computed the critical number of turns N_{crit} necessary for a given set of operating conditions,

and then experimentally validated these by testing CLPHPs possessing higher and lower number of turns. They found that for $N < N_{crit}$ the device did not operate horizontally whilst for $N > N_{crit}$ the CLPHP operated in all orientations. The system performance was also seen to decrease when approaching horizontal operation. Practically, these findings imply that a minimum number of PHP turns should be used in devices designed for horizontal operation.

2.4.2 Orientation with respect to vertical

As previously mentioned, the operation and performance of a PHP depends on its orientation with respect to gravity. This is due to the relative influence of the two driving mechanisms responsible for their operation, namely: (i) The two-phase flow is driven by buoyancy forces caused by the difference in density of the liquid and the vapor phases, and (ii) the flow is driven by inertial forces caused by evaporation and condensation of the working fluid. For any given orientation the driving mechanism is a combination of these two components, with the influence of the first decreasing with increasing inclination from vertical evaporator down.

In order to study the effect of gravity on mass transfer inside PHPs, Tong et al. (2001) carried out flow visualization of a PHP during vertical and horizontal operation. They observed an accumulation of liquid at the evaporator U-bends for vertically operating CLPHPs. This flooding of the U-turn region eventually caused the break up of the transiting vapor plugs thus producing new liquid slugs. Dry-out of the evaporator section and successive stop-over could then be reached at higher heat fluxes. On the contrary, when vapor plug agglomeration took place in the evaporator, they found that flow oscillations stopped, thus leading to local dry-out and failure. However, they noted that PHP devices did not start-up or operate reliably when inclined or horizontal.

Similarly, Khandekar et al. (2002b) did not observe oscillation nor proper operation in a multi-turn flat plate aluminum CLPHP with a 2 mm hydraulic diameter between 75° and 85° from vertical. Xu et al. (2006), in a similar geometry working with butane and R134a, observed oscillation in all possible orientations, albeit different thermal performances. The difference in performance between bottom heating mode and the top heating mode was seen to decrease with increasing heat inputs due to the decreasing influence of gravity (Hemadri and Khandekar, 2009).

2.4.3 Working fluid

Since fluid properties, such as *viscosity*, *surface tension*, *dynamic contact angles*, *specific and latent heat*, and *variation of saturation pressure with temperature*, affect the frictional pressure drops and phase change thermodynamics of the system, they have a strong influence on the thermo-hydrodynamic characteristics of a PHP.

To enhance the convective heat transfer in the device, the working fluid, when evaporating, should rapidly expand, thus aiding the two-phase flow motion (Khandekar et al., 2002b).

Therefore, large pressure fluctuations with smaller heat inputs $\left(\frac{\delta P}{\delta T}\right)_{sat}$ are then preferred (Khandekar et al., 2003b). The rate of bubble growth and shrinkage was seen to be proportional to the **latent heat**, thus low latent heat fluids producing quick bubble generation/collapse are also preferred (Khandekar et al., 2003b). In particular, to avoid too rapid evaporation leading to dry-out, fluid choice could be coupled to filling ratios (Khandekar et al., 2002b).

Given the high ratios of sensible over latent heat exchanged involved on PHP operation, fluids should have a high **specific heat** to enhance the overall heat transfer performances (Zhang and Faghri, 2008).

Two-phase flows over a solid surface also encounter the resistance produced by dynamic contact angle of hysteresis effects (Van P. Carey, 2008). Therefore, working fluids characterized by small **dynamic hysteresis angles** are preferred (Khandekar et al., 2003b). For similar reasons, low values of **dynamics viscosity** are preferred due to the reduced shear stress and pressure drop which help to sustain the two-phase flow motion (Zhang and Faghri, 2008; Khandekar et al., 2003b). Moreover, since bubble nucleation is essential for the start-up of a PHP, it has been suggested that fluids with low **surface tension** are preferred, thus reducing the minimum heat load necessary for start-up (Maydanik et al., 2009).

2.4.4 Filling Ratio

The filling ratio FR is defined as the ratio of the charged volume of liquid over the total internal volume of a PHP, and thus corresponds to the volumetric void fraction of the whole system. The filling ratio, also known as fill ratio or charging ratio, has been observed to significantly affect the operation and thermal performance of a PHP. Khandekar and Groll (2006) stated that the optimum FR for a given device depends on the particular combination of working fluid, PHP geometry and operating conditions present. Different FR operational ranges have been proposed, each presenting different thermal characteristics (Groll and Khandekar, 2003):

- $FR = 0\%$: the heat transfer in these empty devices is purely by heat conduction and characterized by very high thermal resistances;
- $FR \approx 0\%$: very small liquid inventory leading to evaporator dry-out;
- $20\% < FR < 80\%$: typical working range for pulsating mode operation;
- $FR \approx 100\%$: the low void fraction can not generate sufficient pumping action, thus such PHP has to be operated at higher heat fluxes (Wang and Nishio, 2005; Cai et al., 2002);
- $FR = 100\%$: the heat transfer in these fully filled system is due to single-phase natural convection and heat conduction.

2.5 Flow visualization studies

To gain a deeper understanding of the mechanisms governing flow motion in PHPs, their dynamics have been investigated through flow visualization. The resulting qualitative images of the different flow regimes, and the derived quantitative information regarding their two-phase flow dynamics, has led to a clarification of a number of PHP flow mechanisms.

For example, Tong et al. (2001) observed many different types of two-phase flow instabilities in a glass closed-loop PHP. For vertical operation, the random nucleation and rapid subsequent expansion of vapor bubbles was observed to occur in slow moving liquid slugs residing in the evaporator zone. This expansion of the Taylor bubbles was seen to provide the driving force for flow circulation and local oscillations. Furthermore, Taylor bubble breakdown was observed in the evaporator U-turn due to liquid accumulation, whilst Taylor bubble coalescence was seen in the condenser. During horizontal operation, interfacial waves were observed on the liquid film which then led to the break up of the Taylor bubbles.

2.5.1 Flow patterns and trends in performance

Flow visualization experiments coupled with thermal data have been used to classify flow patterns and to assess their influence on the thermal performance of PHPs for different operating conditions. These studies indicate that heat input is the primary parameter defining the qualitative flow pattern, with filling ratio and inclination playing lesser roles (Tong et al., 2001; Khandekar and Groll, 2003; Khandekar et al., 2003a; Khandekar and Groll, 2004; Xu et al., 2005).

The following flow regimes and trends have been identified and also summarized in Figure 2.3: (a) At low heat input, the restricted pumping action produces low amplitude oscillations with slug flow present in the entire PHP volume. The hot/cold slugs oscillate about a mean position in the evaporator/condenser, resulting in an overall poor heat transfer coefficient; (b) At medium heat input, the amplitude of the slug-flow oscillations increase and become comparable to the length of the device. Thus, the hot fluid is now able to reach the cold section and the heat transfer coefficient increases; (c) Further increasing the heat load, the velocity of the oscillating flow increases and the flow can now take a fixed direction around the device loop with possible flow reversals occurring. Annular flow at the evaporator outlet yields a further reduction of the thermal resistance; (d) At higher heat loads, the flow turns continuously in one arbitrary direction around the device, and shows fully developed annular flow in the evaporator rising tube and slug-plug in the condenser down-comer. This operational state corresponds with the lowest thermal resistance and thus the best thermal performance of the PHP. At very high heat loads, the liquid film on the channel wall dries out and the thermal resistance of the device increases.

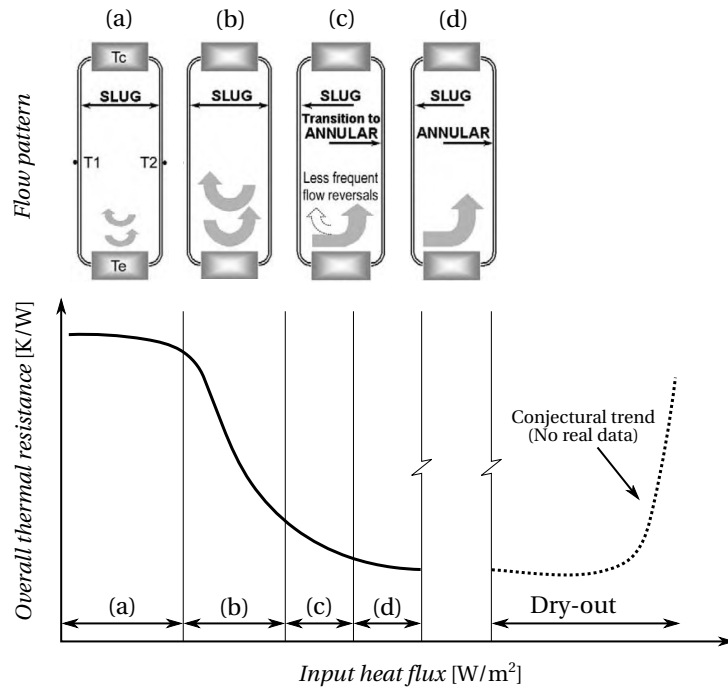


Figure 2.3: Observed flow patterns and relative thermal performance (Khandekar et al., 2009; Khandekar and Groll, 2003)

The heat transfer coefficient obtained for different applied heat inputs to a PHP, comprising a 2 mm copper and glass channel working with ethanol at 65 % fill ratio, was measured by Mameli et al. (2014) and presented in Figure 2.4. This shows how the heat transfer coefficient in the evaporator changes in steps as the heat load is increased due to changes in the two-phase flow pattern in the device. As expected, the highest values of local heat transfer coefficient are obtained at high heat loads where annular flow exists locally.

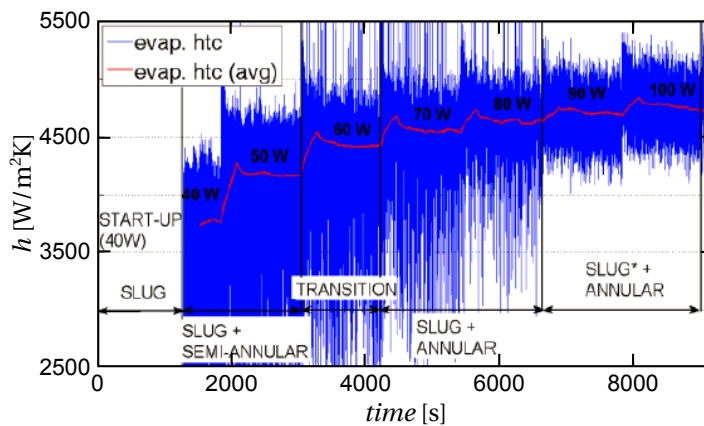


Figure 2.4: Temporal evolution of heat transfer coefficient and flow pattern at different heat inputs (Mameli et al., 2014)

2.6. Two-phase flow dynamics in oscillatory flows

The non-linear complexity of the transport phenomena involved in the operation of a CLPHP, due to the high number of degrees of freedom within the system, leads to the existence of multiple quasi-steady states for the same set of operating conditions, each corresponding to a unique characteristic two-phase flow pattern. Furthermore, for the same set of operating conditions, internal or external flow perturbations can cause flow pattern transitions between these states and consequent changes in thermal performance. This was highlighted by Khandedkar et al. (2009) who observed a number of quasi-steady states in a single loop CLPHP which operated for a 12 hour period at constant operating conditions; these were reported as:

- Sudden start-up corresponding to low operating temperature and thermal power;
- Steady-state 1 (SS1): unidirectional flow showing periods of movement and stop-overs with annular/semi-annular flow in the rising tube and slug flow in the down-comer;
- Steady-state 3 (SS3): continuous unidirectional flow;
- Steady-state 2 (SS2): near complete phase segregation with only little liquid in the evaporator eventually leading to dry-out. However, low amplitude oscillations prevented complete dry-out;
- Steady-state 4 (SS4): dry-out. It could be reversible and after liquid redistribution in the loop another state could be achieved.

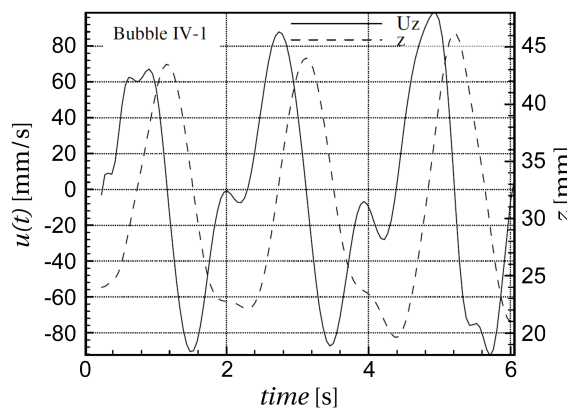


Figure 2.5: Bubble displacement and velocities for methanol in a multi-turn open loop PHP at 10 W heat load (Xu et al., 2005)

2.6 Two-phase flow dynamics in oscillatory flows

2.6.1 Bubble displacement and velocities

Very few quantitative studies assessing the dynamics of oscillatory flows in PHPs are available. Of these, flow visualization of a glass multi-turn open loop PHP carried out by Xu et al. (2005) showed the quasi-sinusoidal behavior of the Taylor bubble displacement and velocities

profiles.

Figure 2.5 shows the observed bubble displacement and velocity for methanol under a 10 W heat load, and indicates the presence of small amplitude oscillations superimposed on the larger oscillation waves. This low amplitude component corresponds to the *local flow direction switch* which adds a stochastic, pulsating component to the system. In a multi-turn open loop PHP, the local flow direction switch process was seen to occur several times in any specific tube and is thought to be caused by the combined action of local boiling, bubble coalescence and condensation.

Furthermore, diabatic tests by Das et al. (2010, 2011) on a unit-cell formed by a single vapor plug and liquid slug, oscillating between two reservoirs kept at different pressure and temperature, showed that the velocity of the slug-vapor interface increases with increasing temperature difference between the two reservoirs.

2.7 Frequency analysis

During the operation of a PHP, the alternating presence of vapor plugs and liquid slugs produces fluctuating evaporator and condenser wall temperatures, whose oscillation amplitudes and frequencies change with heat load and other operating conditions (Xu and Zhang, 2005). Power spectral analysis carried out by Xu and Zhang (2005) showed that the frequency content of the steady state thermal oscillations depends on the liquid-vapor distribution in the PHP volume and on the applied heat flux. In particular, at high heat loads, the PHP displays quasi-periodic thermal behavior, as suggested by the nature of the frequency power spectra of Figure 2.6 obtained for a copper PHP charged at 70 % with R72 under a 26 W heat load.

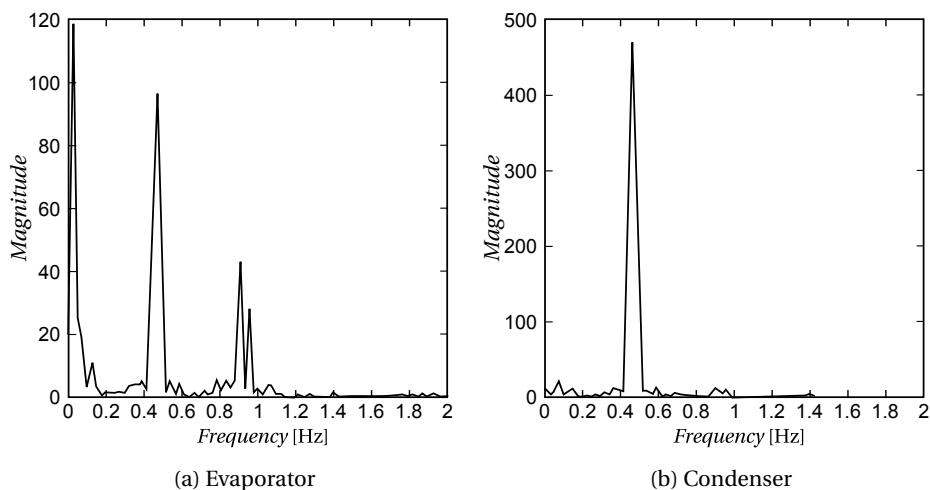


Figure 2.6: Power spectrum of the fluctuating wall temperature in the PHP evaporator (a) and condenser (b), for a heating power of 25.6 W (Xu and Zhang, 2005)

Das et al. (2011) also found that the typical range of dominant frequencies found in a thermally driven self-sustained oscillating PHP system were within 1.7 to 3.36 Hz for methanol and within 1.69 to 4.14 Hz for pentane. Furthermore, these frequencies were seen to increase with the driving temperature difference. This tendency was explained by Cai et al. (2006) to be a consequence of the lower liquid viscosity in the evaporator and of the reduced flow resistance.

Khandekar et al. (2009) analyzed the frequency spectra of the fluctuating system pressure within an operating single loop CLPHP. They found that the nature of the power spectra depends on the flow regime present within the device and that the dominant frequencies were within the range from 0.1 to 3.0 Hz. For example, Figure 2.7 shows the power spectrum obtained for their steady-state 1 (SS1) mode (Section 2.5.1).

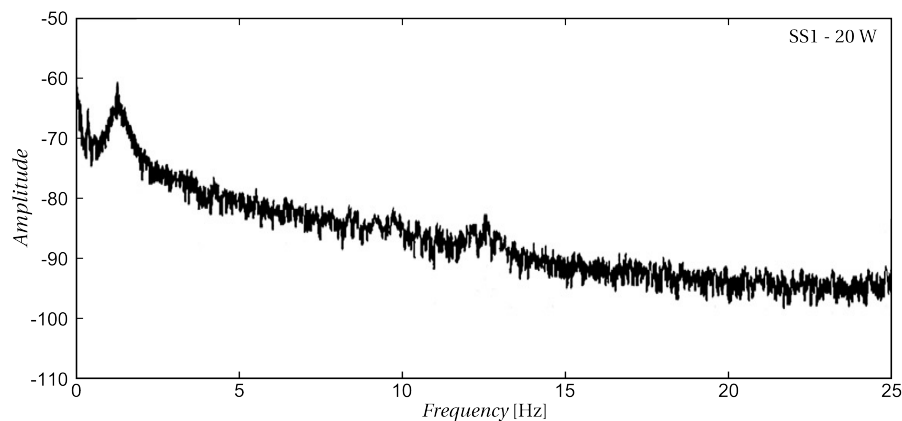


Figure 2.7: Power spectra of pressure variation in a single loop CLPHP for unidirectional flow (Khandekar et al., 2009).

2.8 Conclusions

Since the complexity of a PHP system is such that many aspects related to its operation and performance are unclear, so far no comprehensive tools exist for their design, modelling and optimization (Groll and Khandekar, 2004). In fact, existing theoretical models are limited and based on unrealistic assumptions (Zhang and Faghri, 2008). Therefore, as concluded by Khandekar et al. (2010), more studies on the nature of phase-change induced oscillatory flows in PHPs are needed. This provides the motivation for the present study, which attempts to gain a deeper understanding of such flows in a single loop CLPHP, with a particular focus on revealing the mechanisms governing their thermo-hydraulic behavior.

3 Experimental Set-up and Data Reduction

3.1 Introduction

A new test facility was designed and built for this experimental study on CLPHPs. The architecture of the facility was conceived to allow synchronized thermal and visual investigation of the device. Measurement instrumentation and flow visualization systems were fully computer controlled. A complete description of the facility and its instrumentation is given in this Chapter.

3.2 Test facility

The Closed Loop Pulsating Heat Pipe (CLPHP) facility consists of a hermetically sealed closed loop for the refrigerant, a water loop acting as the cooling source, and an electrical circuit providing heating power (Figure 3.1).

3.2.1 CLPHP test-section

A single-turn channel Closed Loop Pulsating Heat Pipe (CLPHP) was machined into a 10 mm thick brass plate. The channel cross section is 1 mm by 1 mm, the total length of the loop channel is 830 mm with a channel spacing of 13.5 mm. Further details of the test-section geometry can be found in Table 3.1.

Flow visualization was attained via the transparent front side of the test-section which provided full optical access to the flow inside of the CLPHP channels, as depicted in Figure 3.2a. The test-section and the camera were rigidly mounted on a tilting frame which could be set at any orientation α , defined with respect to the *Vertical Evaporator Down (VED)* position, as shown in Figure 3.2b. The back side of the test-section was designed to accommodate ports where instrumentation and auxiliary apparatus, such as the refrigerant charging line, could be placed (Figure 3.2c). Particular care was taken to insert the thermocouple with its tip at the same level with the channel base wall. The temperature around the channel base/wall could



Figure 3.1: CLPHP experimental facility

Table 3.1: Test-section specifications

Test-section	
Number of channels in the loop	1
Channel cross-section	$1 \times 1 \text{ mm}^2$
Channel total length	830 mm
Channel spacing	13.5 mm
Bend radius	2 mm
Channel base thickness	1 mm

thus be measured without perturbation of the flow.

An electrical cartridge heater was inserted into a customized holder and mechanically attached at the back of the test-section. The water cooling circuit was connected to two copper flat tubes, also attached to the back of the test-section, as depicted in Figure 3.2c. In part, this design could provide optical access for surface infra-red temperature measurements.

The internal volume of the CLPHP was 830 mm^3 and thus great care was taken to avoid any leak of the working fluid and non-condensables in the refrigerant. For this reason, the test-section charging line was directly connected to the CLPHP loop through a bellows-sealed valve (SS-6H-MM by *Swagelok*), as in Figure 3.3.

To ensure that there were no leaks of refrigerant, the system was pressurized with nitrogen and controlled for at least 24 hours. If no change in the system pressure occurred, the system

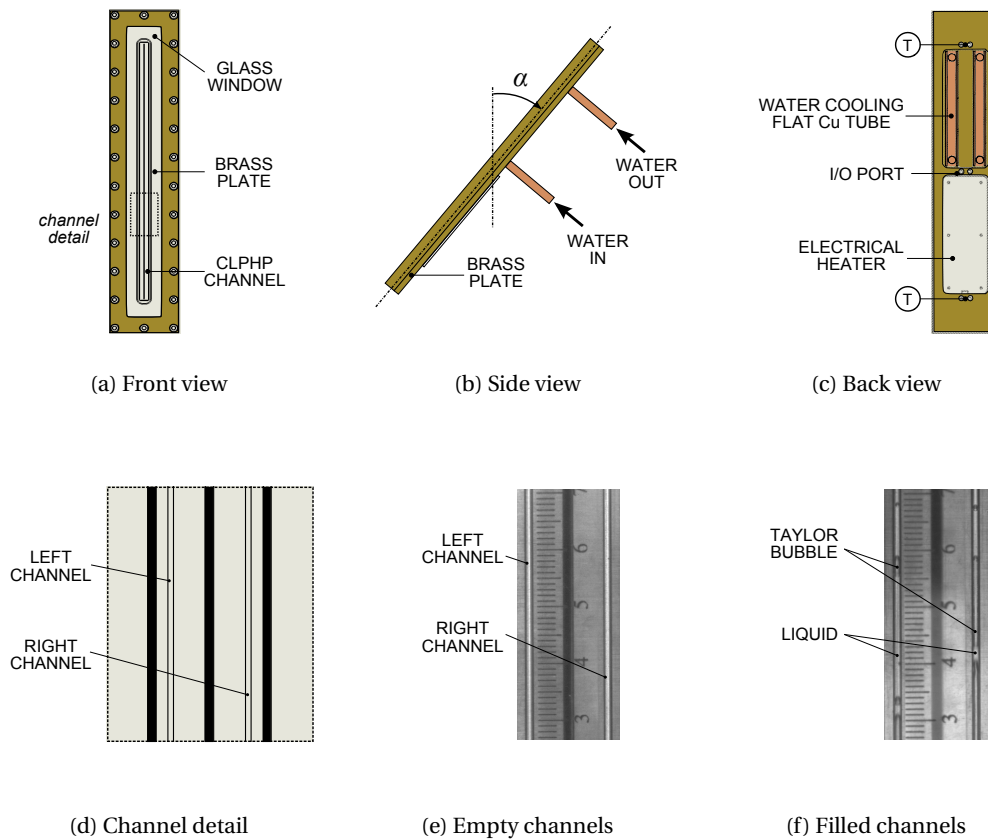


Figure 3.2: Schematics of test-section

was accepted as being gas-tight under high pressure.

For vacuum testing, the system was evacuated with the use of a vacuum pump (MK-060-DS by *ITE*) until the internal pressure was not much higher than 0.27 mBar. The vacuum pump was run for 24 hours whilst the pressure in the circuit was monitored by means of a vacuum gauge by *Hastings*. If no major change in the system pressure occurred, the system was accepted as being gas-tight under vacuum and could be operated.

Particular care was taken when charging the system with refrigerant. The refrigerant reservoir was pre-emptively vacuumed and charged with the working fluid. To remove impurities such as non-condensable gases and other contaminants, the refrigerant was heated and the bottle vented.

3.2.2 Working fluid and system charging procedure

R245fa (1,1,1,3,3,-pentafluoropropane: $C_3H_3F_6$) was used for testing the single-turn CLPHP. It represents an alternative for dichlorofluoroethane (HCFC-141b) and trichlorofluoromethane

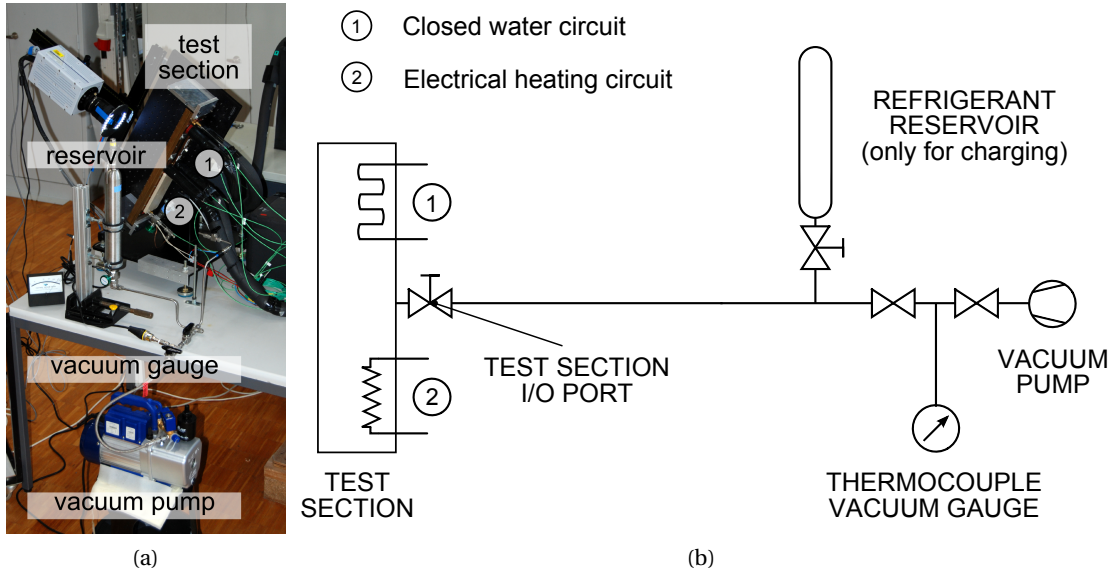


Figure 3.3: (a) Charging line and its connection to the CLPHP test-section. (b) Schematics of the charging line with charging bottle, vacuum gauge and vacuum pump.

(CFC-11) due to a Ozone Depletion Potential (ODP) of 0, a Global Warming Potential (GWP) of 950 and its non-toxicity (U.S. Energy Information Administration, 2003; European Centre for Ecotoxicology, 2004).

In the framework of this research activity, R245fa was chosen for offering low operating pressures within the range of tested temperatures (Table 3.2). Moreover, with respect to other low pressure working fluids, such as R1233zd (Table 3.2), it is characterized by higher $\left(\frac{\delta P}{\delta T}\right)_{sat}$, specific and latent heats together with lower viscosity. All these properties have been proved to positively affect the heat and mass transfer in the device, as previously described in Section 2.4.3.

Table 3.2: Physical properties of R245fa and R1233zd at $T_{sat} = 20^\circ \text{C}$ (NIST, 2007)

Property	Unit	R245fa	R1233zd	Relative to R245fa [%]
$T_{sat} = 20^\circ \text{C}$				
p	[kPa]	123.80	106.28	14.1
$\left(\frac{\delta P}{\delta T}\right)_{sat}$	[kPa/K]	0.0441	0.0368	16.5
ρ_l	[kg/m ³]	1352.2	1298.1	4.0
ρ_v	[kg/m ³]	7.156	5.982	16.4
h_{lv}	[kJ/kg]	193.78	193.36	0.2
c_p	[kJ/kg K]	1.3283	1.1514	13.3
M	[kg/kmol]	134.05	130.5	2.6
μ_l	[$\mu\text{Pa s}$]	432.32	487.3	-12.7
σ	[N/m]	0.0146	0.0133	9.2

In order to allow the filling of the system with very small quantities of refrigerant, a metric ruler was glued onto the glass window and used to measure the volume of liquid charged into the CLPHP volume (Figure 3.2e). The total uncertainty in the measurement of the charged liquid volume, thus filling ratio FR , takes into account the resolution of the measuring system (1 mm) and the geometrical tolerance between the glass window and the brass plate. The maximum error in the filling ratio measurement was estimated to be 5 %.

3.2.3 Water circuit

The cooling power necessary for condensation of the working fluid was supplied by the water circuit of Figure 3.4. The water flowing in the *primary* circuit passed through the flat copper tubes attached to the back of the test-section and thus was heated up. Thereafter it passed through a heat exchanger to cool it down to the required temperature. The latter was controlled by setting the temperature of the cooling fluid in the *secondary* circuit by means of a controlled temperature bath (*LAUDA UKS 3000*). In order to reduce the temperature oscillations measured at the outlet of the thermal bath, a water reservoir was installed in the primary circuit, downstream of the heat exchanger. The mass flow rate of the water in the primary circuit could also be controlled by varying the speed of the water circulation pump.

The two circuits were instrumented with two Coriolis flow meters and thermocouples in the positions indicated in the schematics of Figure 3.4. The enthalpy loss/gain in the different sections of the circuit due to natural convection or frictional contribution could be measured for different operating conditions. In this way, a complete thermal characterization of the water circuit could be achieved, thus allowing future measurements to be corrected.

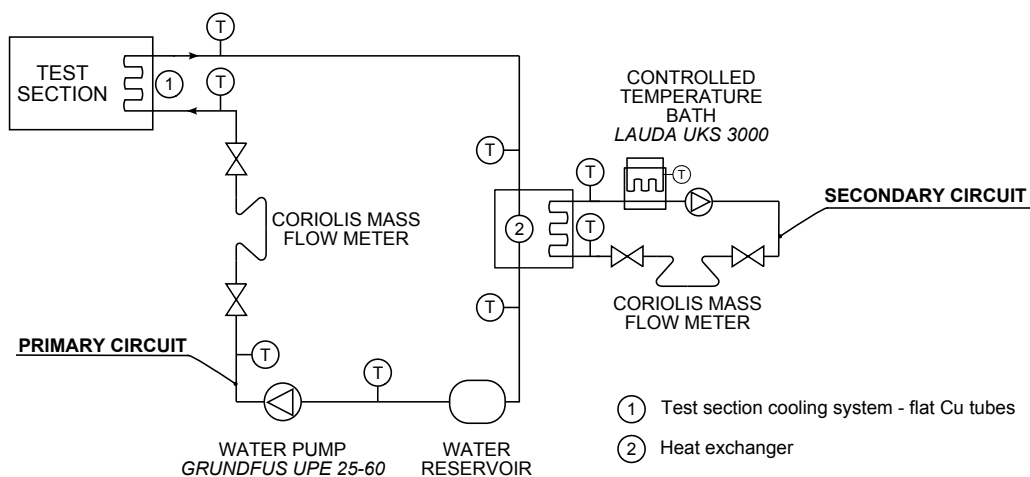


Figure 3.4: Schematic of the water cooling circuits showing the test-section, pump, heat exchanger, temperature controlled bath and instrumentation.

3.2.4 Electrical Circuit

The thermal power necessary for the evaporation of the refrigerant was provided by an electric cartridge heater Omegalux CIR 2079/240 by *Omega* with a maximum power density of 20 W/cm^2 . The resistor was connected to the electrical circuit in Figure 3.5 and was fed by a *Sorensen* DLM 300-10E power supply.

The electrical power supplied to the cartridge heater was computed from the measured voltage applied to the heater and the current flowing through the heater circuit. The current was taken to be the power supply signal, which was experimentally validated for the working range of the cartridge heated by comparing it with *4 wires measurements* of a shunt resistor.

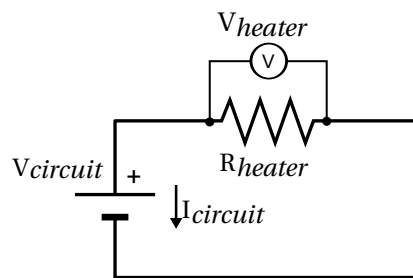


Figure 3.5: Cartridge heater electrical connections

3.3 Instrumentation and Data Acquisition

3.3.1 Data acquisition

The facility was equipped with two data acquisition systems. Electrical measurements were recorded using an *Agilent* HP34970a data acquisition unit connected to the computer through a *RS-232* port. The *Agilent* data acquisition system was equipped with a HP34902a module, providing 16 differential channels with a maximum sampling rate of 600 Hz/channel and an input range of $\pm 300 \text{ V}$.

A *National Instruments* data acquisition system with a PCIe-6323 card was used for the thermal measurements. This card provides 32 differential channels with an analog to digital resolution of 16 bits and a sampling rate of 250 kS/s. The input range of the 48 digital I/O lines was $\pm 10 \text{ V}$.

Low frequency instrumentation, such as the water cooling loop thermocouples and flow meters, were connected to an isothermal terminal block (SCXI-1303) connected to a 32 channels voltage measurement module (SCXI-1102) with a hardware 2 Hz lowpass filtering. The latter communicated with the PCIe-6323 card through a SCXI-1000 chassis. In order to measure a test parameter for each channel, 100 acquisitions were made in 0.1 s and the mean of these 100 values was calculated during the acquisition. To obtain one steady state data point, 60 measurements were recorded for each channel and averaged. The same acquisition card was

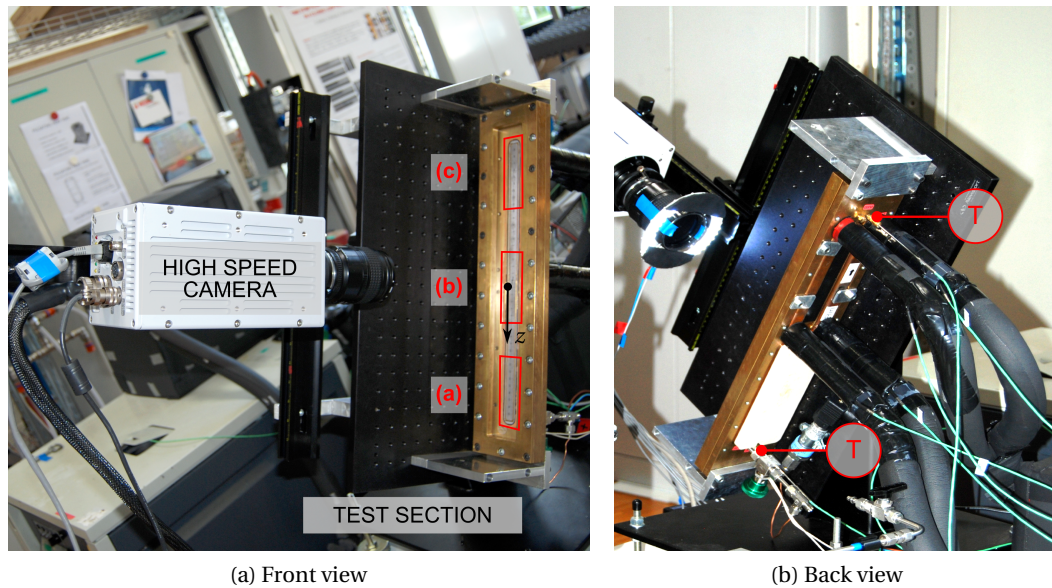


Figure 3.6: (a) Front view of the test-section showing the location of the high speed camera, and (b) back view of the test-section showing the thermocouple positions.

used for the acquisition of the high frequency measurements, such as the signal of test-section thermocouples.

A SCXI-1302 terminal block was used to connect the instrumentation to a SCXI-1180 I/O connector block. The SCXI-1180 allowed different configurations of connection according to the signal source type. A digital output channel was configured and used to start the recording of the high speed camera. The digital trigger was used to synchronize the acquisition of the high frequency temperature data with the videos of the flow in the CLPHP channels.

3.3.2 Instrumentation

Synchronized thermal and visual investigation of the flow-dynamics inside the CLPHP loop was carried out at the (a) evaporator U-turn, (b) evaporator inlet/outlet, and (c) condenser U-turn; as depicted in Figure 3.6. Two thermocouples and a pressure sensor (later removed) were placed at the top, bottom and center of the loop respectively. These provided the high frequency measurements. The instrumentation of the CLPHP facility included:

Thermocouples All the thermocouples were calibrated within the temperature range from 0 to 70°C in a thermal bath using as reference two platinum probes. A second degree polynomial equation was applied to correct the measurement and the uncertainty in each thermocouple measurement was 0.1 K (Figure A.1a).

The water circuits were instrumented with 12 K-type thermocouples of 2 mm diameter, whilst for the test-section 250 μm diameter K-type thermocouples were chosen due to their faster

Chapter 3. Experimental Set-up and Data Reduction

thermal response. As depicted in the schematic diagram of Figure 3.7, the test-section thermocouples were flush-mounted to the channel wall to minimize the effects of transient heat conduction through the channel base plate. The temperature oscillation of the channel wall could then be measured without perturbation of the flow. The precision of the test-section thermocouples was measured to be less than 0.02 K (Figure A.2)

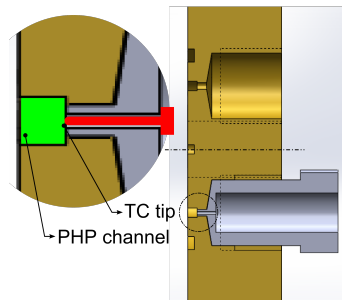


Figure 3.7: Test-section thermocouples mounted flush to the channel wall.

Pressure sensor A Keller absolute pressure transducer was employed for monitoring the operating conditions during pressure testing of the test-section. The operating range was 0-10 bar with a stated accuracy of ± 0.4 % full scale. The latter was reduced by calibrating the instrument with a hydraulic dead weight balance (Figure A.1b).

Flow meter Two Coriolis mass flow meters were installed with a range of 0-200 kg/min for the primary circuit and 0-20 kg/min for the secondary. The uncertainty of the measurements were provided by the manufacturer and are reported in Appendix A. All good engineering practices for the installation of the flow meters were observed, in agreement with the supplier guidelines.

High Speed Camera A high speed Photron Fastcam SA3 digital camera was used to record the two-phase flow dynamics at different locations along the CLPHP loop. The camera was capable of recording up to 120000 fps. It had a 12-bit 1024 x 1024 pixels CMOS sensor with 17 μm pixel size and adjustable shutter speed. A Nikon AF Micro Nikkor lens with a focal length of 60 mm was used to observe the region of interest.

The resolution of the acquired videos was 1024 \times 256 pixels with a resulting scale factor of approximately 1 pixel per 80 μm and a captured area of the size 85.3 mm \times 21.3 mm. The frame rate utilized was 500 Hz and for each test case a sequence of 10906 frames, equivalent to 21.812 s of time, was recorded. The video controller was used to start the recording at exactly the same time as the high frequency temperature measurements.

Light source and optics The test-section was designed to have full optical access to the flow occurring inside the CLPHP channels. The optical window was a 10 mm \pm 0.1 mm thick tempered (Swissdurex) glass plate with a declared transmissivity of 91 % within the

3.4. Experimental set-up validation and experimental protocol

range [390,700] nm. A 12 V, 5 W ring light source was designed and manufactured using commercial 5050 SMD LEDs. A metric ruler was glued onto the glass windows and used for spatial calibration of the camera.

3.4 Experimental set-up validation and experimental protocol

The test set-up and instrumentation were tested prior to the experimental campaign. This preparatory work included the computation of the energy balance and sampling data for the high frequency measurements.

3.4.1 Energy balance

The empty system (0 % filling ratio) was tested to evaluate the energy balance. The electrical power P_{el} and the heat removed by the water cooling system Q_{out} were measured in order to compute the heat losses by natural convection to ambient Q_{loss} . Within the tested range of heat loads, the heat losses were less than 4 %, as depicted in Figure 3.8.

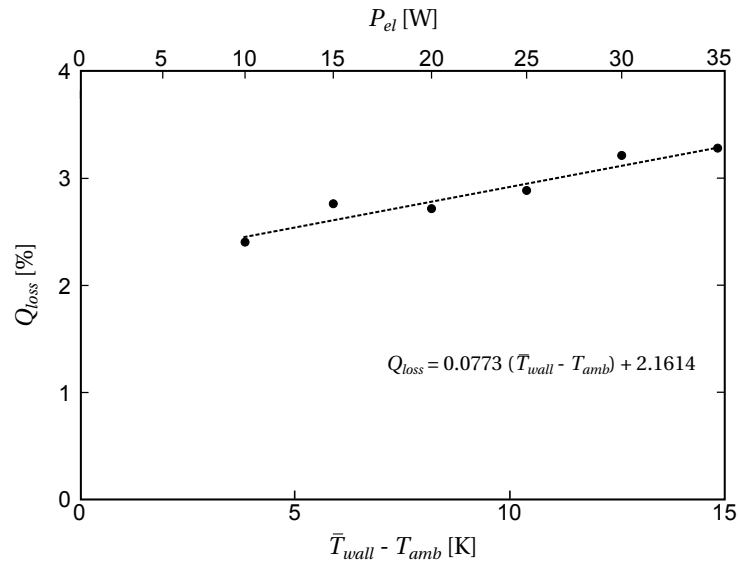


Figure 3.8: Energy balance results for tests at $FR = 0\%$.

3.4.2 High frequency data sampling

High frequency temperature measurement were carried out while operating the empty system, to check for the possible interference of electrical apparatus with the instrumentation.

High frequency measurements during operation at different filling ratios were carried out to define the best sampling parameters. The needed resolutions on both time domain (sampling frequency) and frequency domain (number of samples) were reached when acquiring 2048

samples at 20 Hz for the temperature measurements in the test-section and 10906 frames at 500 Hz for the high speed video imaging. A good trade off between the number of samples and the image resolution was in this way attained.

3.4.3 Experimental protocol

The objective of the experimental phase of this study was to characterize the relationship between thermal behavior and two-phase flow dynamics under different operating conditions. Therefore, flow visualization was carried out in order to extract quantitative and qualitative information about the two-phase flow pattern and its oscillations. These data were then coupled with high frequency temperature measurements from the test-section in order to assess any correlations.

Considering the numerous control parameters involved, and the consequent non-linear nature of the system, a standard protocol was set-up to regulate the experimental procedure. The following steps were taken:

1. The system was evacuated for at least 12 hours after any test run.
2. The CLPHP was charged at the desired filling ratio FR and left inoperative for a few hours.
3. The CLPHP was operated by setting the temperature of the cooling circuit (section 3.2.3) and the heating power (section 3.2.4). The latter was increased in steps of 2 W, within the range $[0, 60]$ W.
4. For each test condition, after steady-state was reached, first the low frequency (LF) set of measurements, including water and electrical circuit quantities, was recorded. The high frequency (HF) set of measurements of the test-section thermocouples was then recorded synchronously to the high-speed videos.
5. At the end of each test run, after the flow motion had stopped, the charge quantity (FR) was controlled to check for possible refrigerant leaks, measuring the level of liquid refrigerant.

Table 3.3: CLPHP experimental matrix

Refrigerant	FR [%]	P_{el} [W]	α [deg]
R245fa	20:10:90	2:2:60	0-45
	40, 60, 80	10:10:40	0:15:90

3.4.4 Experimental data sets

For each data point, corresponding to a particular location in the experimental test matrix of Table 3.3, the electrical power P_{el} and the water circuit measurements were carried out in order to compute the net heat input into the test-section Q_{in} . The high frequency temperature measurements in the test-section T_{evap} and T_{cond} were then recorded synchronously to the videos of the two-phase flow. Three different sets of high frequency temperatures-videos were finally acquired, one for each of the three zones previously identified (Figure 3.6a). More than 400 operating conditions were tested.

3.5 Data reduction

In this study, the flow direction (z -axis) was chosen as positive in the counter-clockwise direction, with the origin of the coordinate system being set at the midpoint of the CLPHP left channel centerline, as depicted in Figure 3.6a. Notably, the thermocouples were positioned at $z=200$ mm for the evaporator T_{evap} and at $z=630$ mm for the condenser T_{cond} .

3.5.1 Video sequence processing

From the image sequence to the time-strip

The time-strip image processing technique implemented by Borhani et al. (2010) was utilized to obtain a 2D space-time representation of the flow inside the CLPHP channels. A schematic of the condenser and evaporator U-turns is shown in Figure 3.9a and 3.9c. In order to create the time-strips, the frame space dimension was first reduced by rotating the right and bottom channel centerlines so that they were aligned with the left channel, as depicted in Figures 3.9b and 3.9d. The time-strip was then built by extracting the two-phase flow distribution along the channel centerline for each frame and plotting it as a function of time, as depicted in Figure 3.10c and 3.10d (Borhani et al., 2010; Sage et al., 2010).

In a video sequence, the intensity of a given pixel resulted from the different attenuation rates of light in the different phases, together with the effects of reflection and refraction at the phase interfaces. Dark regions corresponded to the nose and tail regions of the vapor bubbles, gray areas indicated the presence of liquid films on the channel walls, and light gray areas indicated the presence of liquid slugs, as shown in Figures 3.10a-3.10d. The positive counter-clockwise flow direction is depicted from top to bottom in the time-strips.

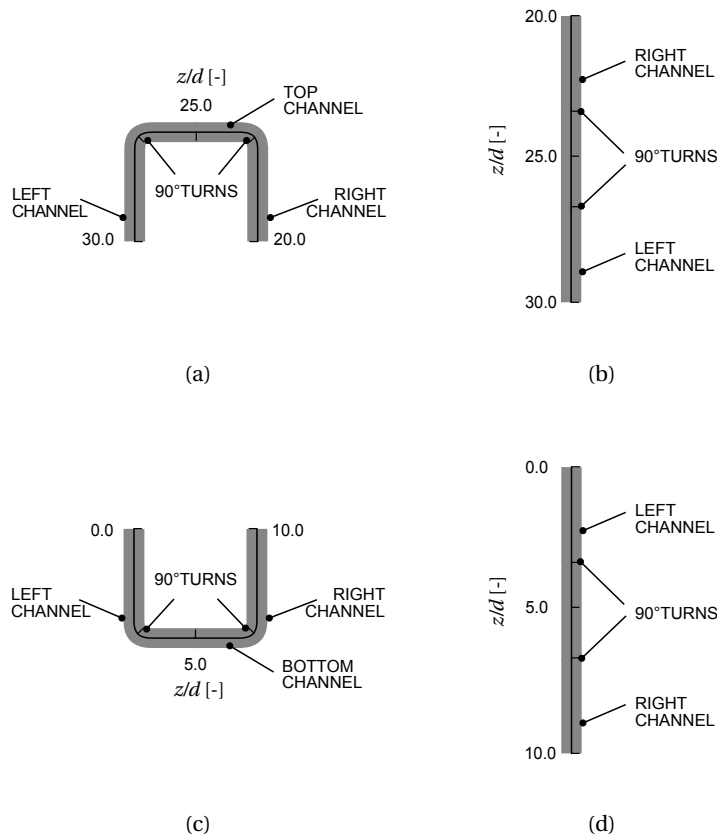


Figure 3.9: 2D Schematics of the condenser (a) and evaporator (c) U-turns, and 1D schematics after unfolding (b) and (d).

Time-strip post-processing

The time-strip representation of the flow dynamics showed good potential for extracting quantitative information of the flow such as interface trajectories, velocities and evaporation/condensation rates. Ad hoc image processing algorithms were implemented in order to reduce such data.

Dominant frequency components The time-strip intensity at a given position z was converted into the frequency domain by means of the Fast Fourier Transform (FFT) algorithm with a frequency resolution of 46 mHz. Frequency spectra were thus built.

Tracking of the liquid-vapor interface during oscillations In a time-strip (see Figure 3.11a), the local intensity identifies the liquid and vapor phases. Intensity gradients in the time-strips, due to the nature of the incident illumination and subsequent reflection, producing horizontal artifacts, needed to be addressed during the post-processing. The input image was first processed by applying a vertical low pass filter and then a Gaussian blur. The filtered

image was then thresholded and further processed to remove any noise still present in the white (*closing* morphological operator) and black (*opening* morphological operator) areas. Finally, a Sobel edge detection algorithm from the Matlab[®] image processing library was applied and the interface profiles were defined and tracked. The image processing algorithm was benchmarked against different operating conditions and the best set of parameters were then chosen.

In order to characterize the displacement of a liquid slug as a function of time, the displacement $z(t)$ of the center of mass of the chosen liquid slug was computed. The center of mass was defined as the mid point between the top and bottom interfaces (the trailing edge of the top vapor plug and the leading edge of the bottom vapor plug) at each time instant. To obtain a clean displacement profile, the high frequency component has to be removed if present. Figure 3.11a shows the filtered displacement curve of a liquid slug oscillating about the evaporator U-turn superimposed on the time-strip from which it was generated. For the particular case of Figure 3.11a the cut-off frequency of the low pass filter was chosen to be 2.5 Hz. The latter was selected with the help of the frequency spectra computed for the time-strip intensity profile. Raw and filtered trajectories are presented in Figure 3.11b.

The velocity $u(t)$ of the center of mass of the same liquid slug (Figure 3.11c) was computed as:

$$u(t) = \frac{\Delta z}{\Delta t} = \frac{z(t + \frac{5}{500}) - z(t - \frac{5}{500})}{(t + \frac{5}{500}) - (t - \frac{5}{500})} = 50 \cdot (z(t + 0.01) - z(t - 0.01)) \quad (3.1)$$

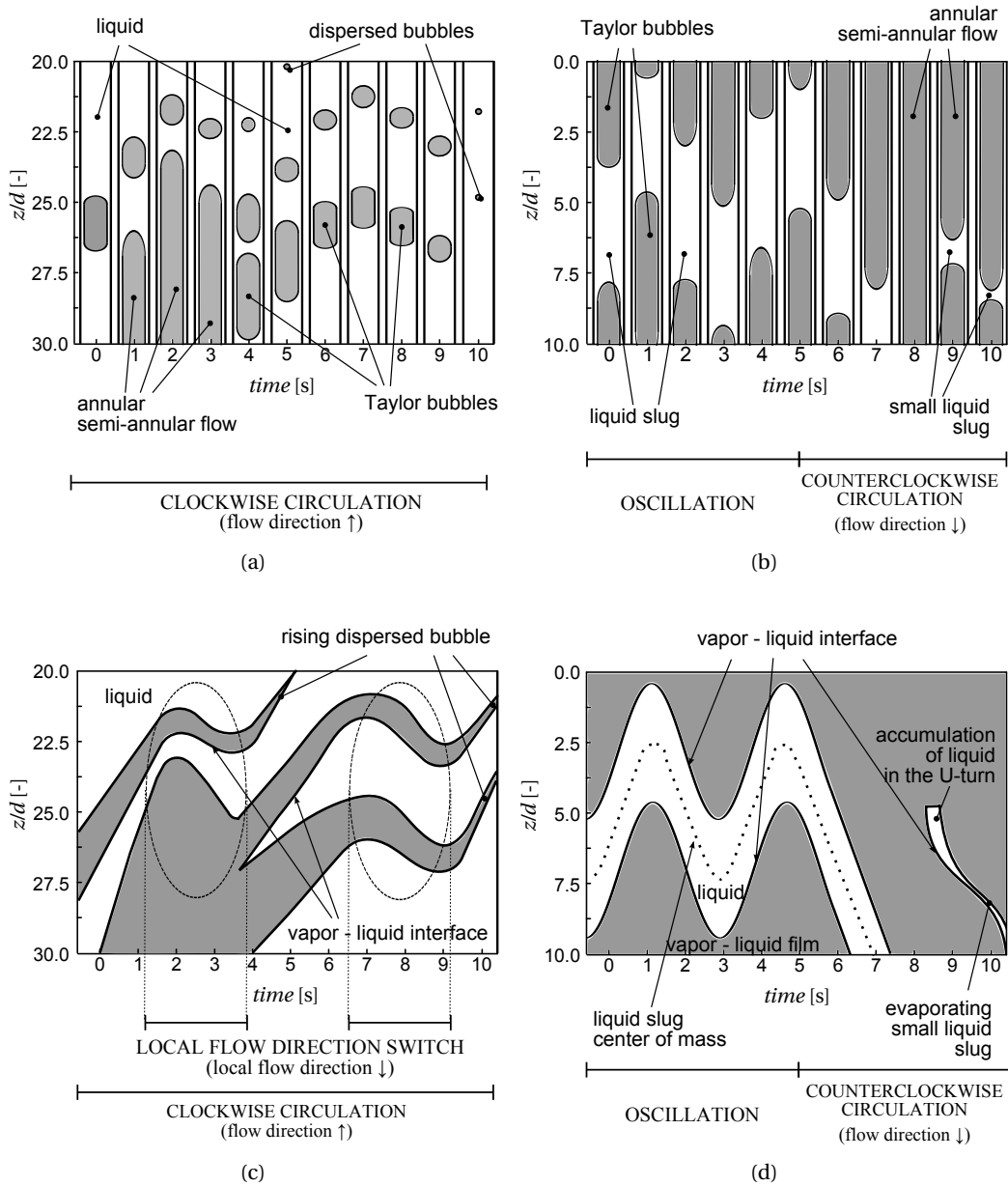


Figure 3.10: Frame sequence schematic (a) and corresponding time-strip (c) of clockwise circulation. Condensing annular flow (0-3 s) and Taylor bubbles (3-10 s) rise up the left channel of the PHP and briefly change direction as a consequence of the local flow direction switch. Frame sequence schematic (b) and corresponding time-strip (d) showing oscillating slug flow (0-5 s) and counter-clockwise circulation with creation and evaporation of small liquid slugs in the evaporator U-turn (5-10 s).

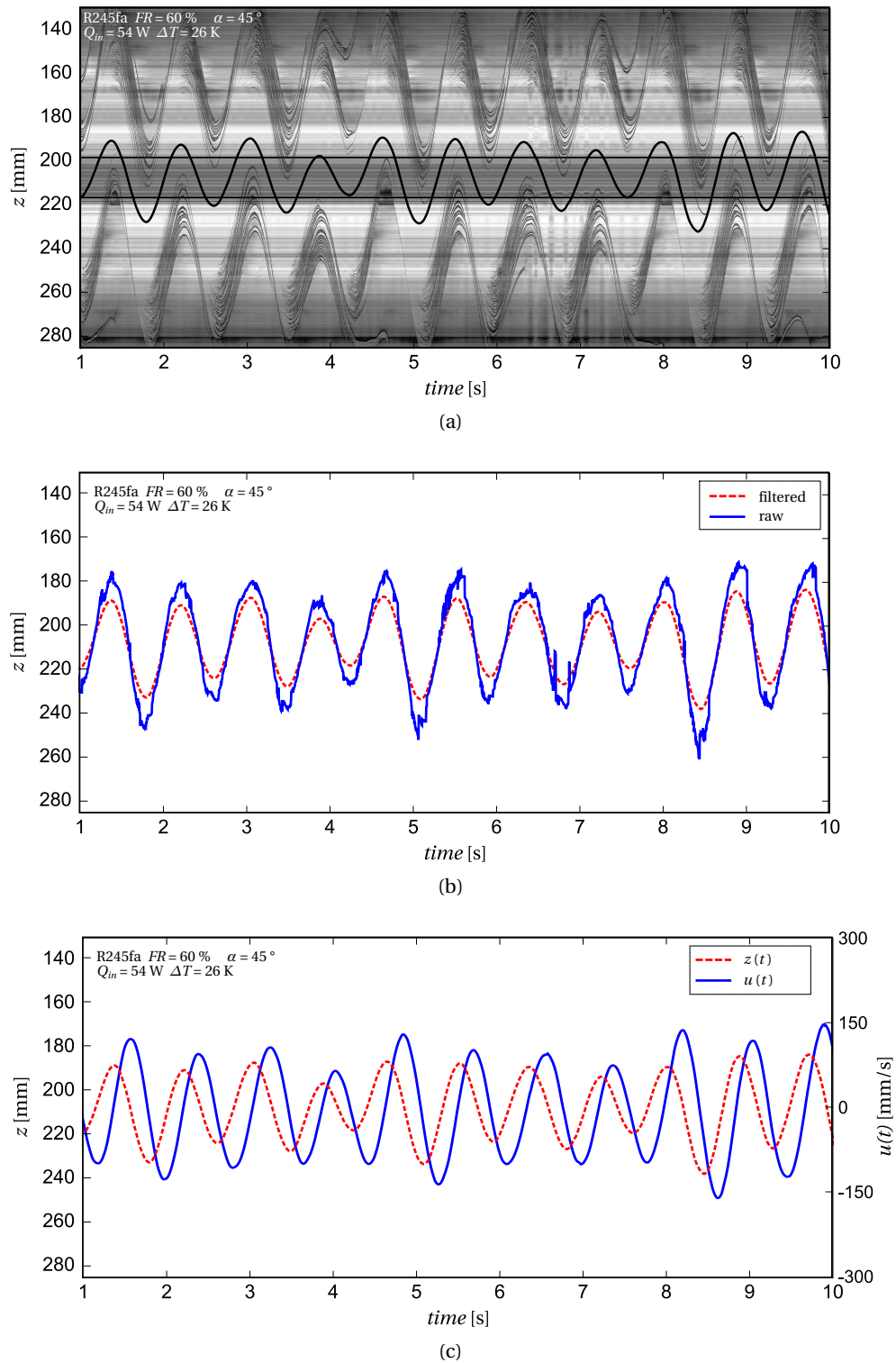


Figure 3.11: (a) Time-strip and superimposed displacement profile $z(t)$, (b) Raw (solid line) and filtered (dashed line) displacement profiles $z(t)$, (c) displacement $z(t)$ (dashed line) and velocity $u(t)$ (solid line) profiles for a liquid slug oscillating about the evaporator U-turn. $Q_{in} = 54\text{ W}$, $FR = 60\%$, $\alpha = 45^\circ$.

Tracking of the liquid-vapor interface when moving quasi-unidirectionally The trajectories $z(t)$ of the liquid-vapor interfaces moving unidirectionally or quasi-unidirectionally (as for circulating flow) were manually tracked from the time-strips using the commercial software for graph digitizing Origin[®], as shown in Figure 3.12a. The local velocities $u(t)$ were then computed as the time derivative of the displacement profile (as in Figure 3.12b) and could be averaged to compute the average velocities $\bar{u}(t)$.

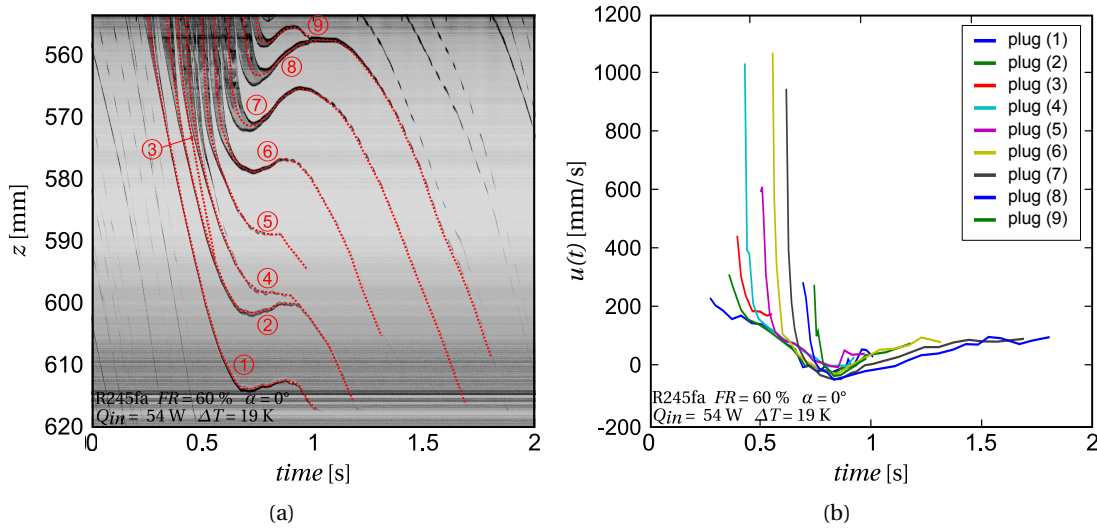


Figure 3.12: (a) time-strip and superimposed displacement profiles $z(t)$, and (b) velocity profiles $u(t)$ for vapor plugs traveling along the condenser U-turn, for an operating condition of $Q_{in} = 54$ W, $FR = 60$ %, $\alpha = 0^\circ$.

3.5.2 Thermal Data Processing

Dominant frequency components

The signals of the test-section thermocouples, measuring the local temperature in the evaporator T_{evap} and condenser T_{cond} , were converted into the frequency domain by means of the Fast Fourier Transform (FFT) algorithm. The acquisition frequency of these data was 20 Hz and each data set counted for 2048 samples, resulting in a maximum resolvable frequency of 10 Hz and a resolution of 10 mHz.

Relative thermal performance

The overall thermal resistance R_{TOT} of the CLPHP under different operating conditions was computed according to Equation 3.2. It was defined as the ratio of the temperature difference

between the evaporator and the condenser $\Delta T = T_{evap} - T_{cond}$ over the *net heat input* Q_{in} .

$$R_{TOT} = \frac{T_{evap} - T_{cond}}{Q_{in}} = \frac{\Delta T}{Q_{in}} \quad (3.2)$$

In order to take into account the thermal losses to ambient, thus the quantity of heat transferred from the hot to the cold zone, the net heat input Q_{in} was computed as the mean value of the power supplied by the electrical heater P_{el} and the heat removed by the cooling circuit Q_{out} (Eq. 3.3).

$$Q_{in} = \frac{P_{el} + Q_{out}}{2} \quad (3.3)$$

The effect of the two-phase pulsating flow on the overall thermal resistance was estimated using Equation 3.4 from Khandekar et al. (2002b). The overall thermal resistance R_{TOT} was considered equivalent to the parallel configuration of (a) the thermal resistance of pure conduction $R_{FR=00}$ and (b) the resistance produced by two-phase flow convective heat transfer R_{PHP} . Thus:

$$R_{PHP} = \left(\frac{1}{R_{TOT}} - \frac{1}{R_{FR=00}} \right)^{-1} \quad (3.4)$$

The ratio of the overall thermal resistance of the empty CLPHP $R_{FR=00}$ over the overall thermal resistance R_{TOT} was computed according to Equation 3.5:

$$R_{ratio} = \frac{R_{FR=00}}{R_{TOT}} \quad (3.5)$$

The thermal resistance of the empty ($FR = 0\%$) CLPHP $R_{FR=00}$ was experimentally evaluated according to Equation 3.2.

3.6 Conclusions

The methods used for experimentation and in the data reduction have been discussed here. This chapter, together with the literature study, serves as the reference for all information used during the discussion in the following chapters.

4 Flow Pattern Results

4.1 Introduction

The operation and the thermal performance of CLPHPs depends not only on the boundary conditions (geometry, temperature levels, filling ratios) but also on the two-phase flow patterns present in the loop. Thus identifying major trends in the flow-pattern transition may in turn reveal novel details about the physics producing the self-sustained two-phase flow oscillations in CLPHPs.

In this experimental study, the flow patterns were inspected through the analysis of the time-strips in order to evaluate possible correlations with the thermal behavior of the system. This Chapter reports the observation on the flow patterns in the evaporator and condenser sections of the CLPHP, as well as the flow dynamics and thermal behavior.

4.2 Flow patterns

Visual observations of the flow in the CLPHP channels were carried out through high-speed video recording and time-strip image processing, as described in Section 3.5.1.

Heat input was observed to be the primary parameter defining the qualitative flow patterns occurring in the evaporator and condenser zones. These were classified into the following general categories (Khandekar et al., 2003a; Tong et al., 2001; Mameli et al., 2011; Xu et al., 2005): (a) *low amplitude oscillation*, (b) *oscillation*, (c) *unstable oscillation with circulation and direction reversals*, and (d) *unidirectional flow circulation*. The superposition of an oscillatory component on the circulating component was sometimes observed and represented as a particular case of circulating flow with '*local flow direction switch*' (Section 6.4.3).

4.2.1 Evaporator dynamics

The time-strips of Figures 4.1a, 4.1b, 4.1c and 4.1e show the four main flow patterns observed in the *evaporator* U-turn within the z range [130, 290] mm, with the midpoint of the U-turn at $z = 207$ mm, for the system operating vertically (VED) at $FR = 60\%$. Figure 4.1d represents the particular case of circulating flow with local flow direction switch. The following dynamics were observed:

Low amplitude oscillation (a) Before starting the operation of the CLPHP, the liquid was segregated at its bottom thus filling the whole evaporator and part of the condenser. To achieve start-up of the device, nucleation and expansion of bubble plugs in the evaporator zone had to take place. At 6 W heat load, this mechanism was periodically triggered at the bottom of the evaporator right channel ($z = 220$ mm), as shown in Figure 4.1a. These small bubbles then progressively expand rising up the right channel under the action of buoyancy forces before coalescing with the proceeding Taylor bubbles. At $z \cong 250$ mm the interface of the long bubble is pushed back towards the bottom of the channel (upwards in the time-strip), for example at $t = 1$ s. This was representative of the small amplitude oscillation flow pattern in the evaporator.

Oscillation (b) Figure 4.1b shows oscillating flow in the evaporator U-turn at a heat load of 10 W. When liquid accumulates in the evaporator U-turn, a long liquid slug forms at the bottom of the evaporator and starts to move along the channel. There is a 180 degree phase shift between nucleation taking place in the two channels, with the subsequent expansion producing the oscillatory flow depicted in the time-strip. Starting from $t = 3.5$ s, nucleation was observed to be more intense, with the subsequent expansion of these vapor bubbles producing oscillating slug flow.

Unstable oscillation with circulation and flow direction reversals (c) Increasing the heat load causes the flow to oscillate at higher amplitudes and to take a fixed direction around the loop even though flow reversal may still occur. Figure 4.1c reports the time-strip relative to operation at 14 W. During the first 3 seconds, the flow pattern was oscillating slug flow which then turned into counter-clockwise circulating flow before reversing its flow direction at $t = 5$ s. The transition from oscillating to circulating flow is thought to be caused by the higher local evaporation rates which produce higher momentum of the two-phase flow along the positive (counter-clockwise) direction. The net momentum now becomes positive and the flow thus temporarily takes the counter-clockwise direction. The flow pattern corresponding to this condition shows that flow oscillation, circulation and reversal can occur with no periodicity.

Unidirectional flow circulation (d) & (e) At high heat loads the flow can take an arbitrary constant direction though the loop with annular flow developing in the evaporator section, as shown in Figures 4.1d and 4.1e for 54 and 64 W applied heat loads. These show a thinning

liquid film on the channel wall in the top part of the time-strip where periodical rewetting was also observed. The steep dark lines represent short liquid slugs coming from the condenser section which then periodically returned through the left channel corners to the evaporator. The liquid can also accumulate in the U-turn and cause bubble breakage.

Evaporator

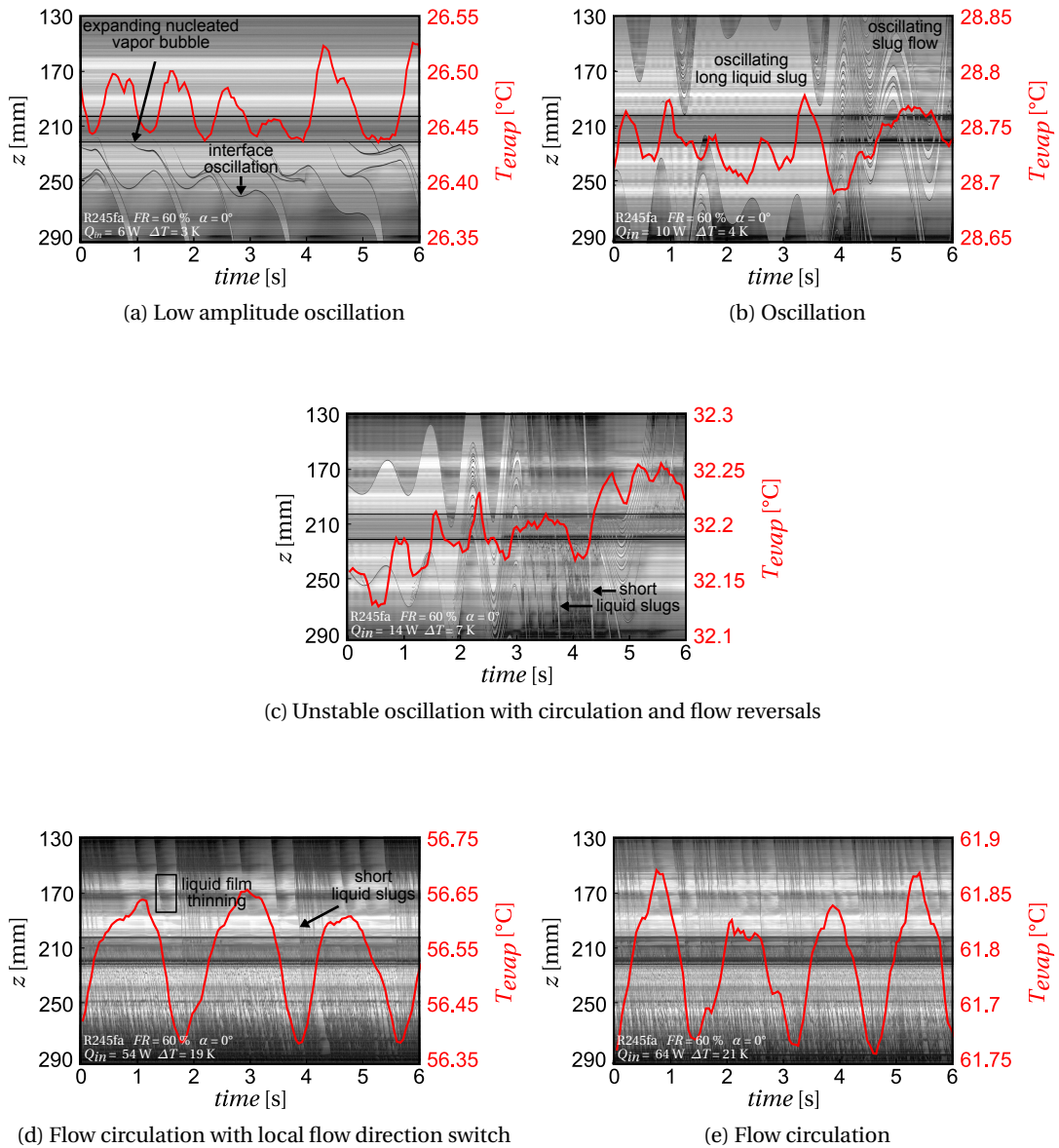


Figure 4.1: Flow Patterns observed in the evaporator section as a function of the net heat input Q_{in} , for $FR = 60\%$ and $\alpha = 0^\circ$.

4.2.2 Condenser dynamics

The time-strips in Figures 4.2a, 4.2b, 4.2c, 4.2d, 4.2e show the two-phase flow in the *condenser* U-turn with $z \in [570, 690]$ mm, and the midpoint of the U-turn at $z = 623$ mm, for the same operating conditions presented for the evaporator in Section 4.1. The following dynamics were observed:

Low amplitude oscillation (a) As described in section 4.1, at very low heat loads the nucleation and expansion of Taylor bubbles was seen to trigger the oscillatory operation of the CLPHP. It propagates throughout the whole system volume and results in the oscillation of liquid/vapor interfaces created anywhere in the CLPHP. In this particular case at a 6 W heat load, as shown in Figure 4.2a, the interface formed at $z = 640$ mm oscillated about a mean position with a quasi-sinusoidal profile.

Oscillation (b) The oscillating trajectory of a condensing vapor plug can be observed in the time-strip of Figure 4.2b at a location of around $z = 630$ mm. In this case, the condenser U-turn was flooded with liquid and only a few small vapor plugs remained due to condensation. These can be used to track the flow motion and thus confirmed the oscillating behavior of the system at a heat load of 10 W.

Unstable oscillation with circulation and flow direction reversals (c) Figure 4.2c reports the time-strip relative to operation at 14 W. Between $t = 0$ and $t = 1$ s, circulation was clockwise with the dark patch at the bottom of the time-strip representing condensing annular flow rising up the left channel. The flow reverted to oscillating slug flow at the U-turn where only small vapor plugs remain due to condensation. At $t = 3.8$ s circulation was counter-clockwise with the top of the time-strip representing condensing annular flow rising up the right channel.

Unidirectional flow circulation (d) & (e) With further increases of heat load, flow circulation became fixed in one arbitrary direction with condensing annular flow in the U-turn. Figure 4.2d and 4.2e show unidirectional counter-clockwise circulation (top to bottom in the time-strip) at 54 and 64 W respectively. At low heat loads (Figure 4.2d, for operation at 54 W), the flow regime in the right channel alternated between rising condensing Taylor bubbles and condensing annular flow, as shown at the top of the time-strip at $t = 1.2, 3.2, 4.5$ s. This caused the flow direction to periodically switch thus producing the oscillatory trajectories of the small bubbles. This phenomenon, called '*local flow direction switch*,' was seen to decrease in amplitude and frequency at higher heat loads. For example, as depicted in Figure 4.2e for 64 W heat load, the flow direction switch is less frequent and the condensing small bubbles travel up the right channel with almost uniform velocity, as shown by the inclined dark lines in the time-strip.

Condenser

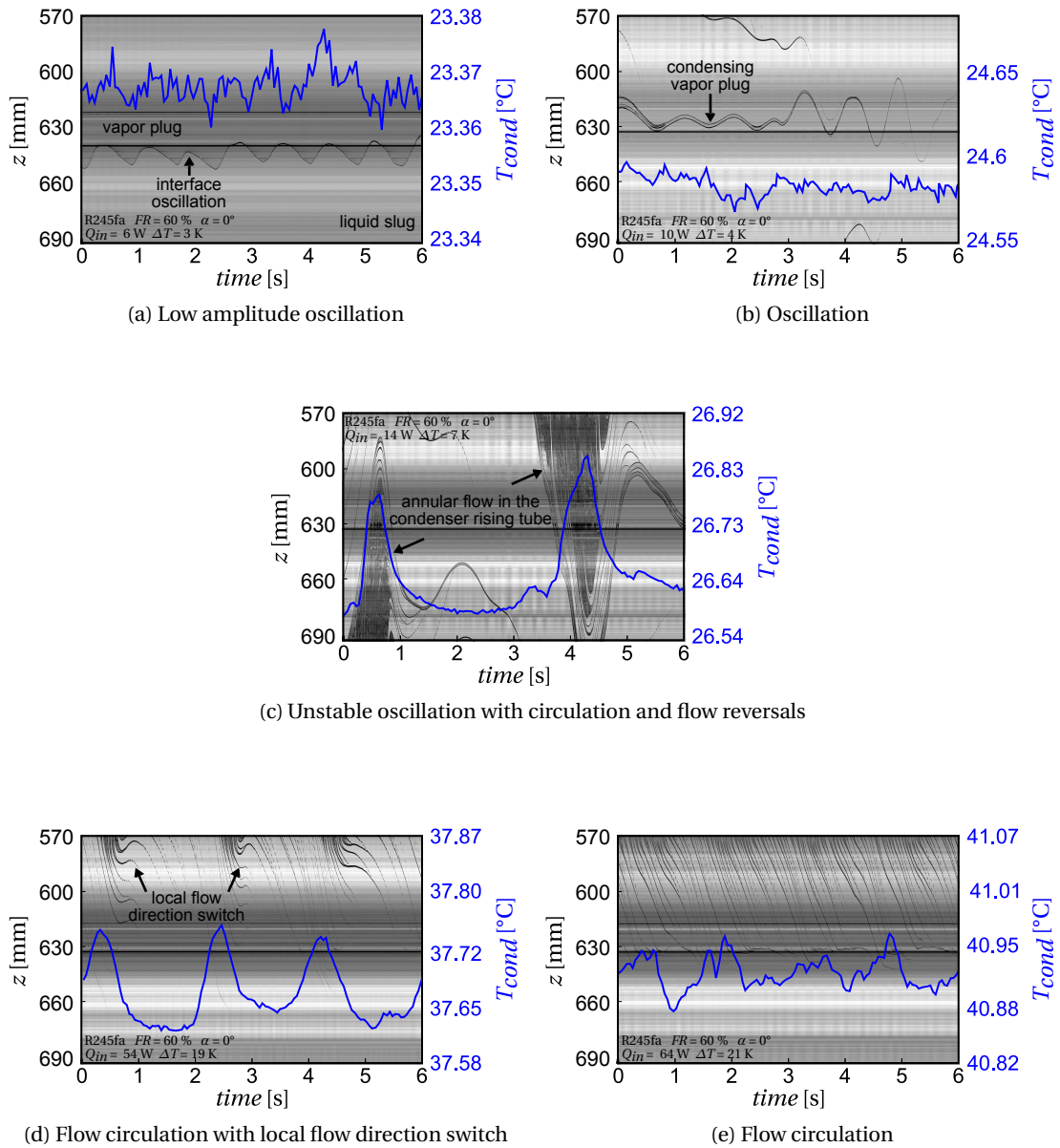


Figure 4.2: Flow Patterns observed in the condenser section as a function of the net heat input Q_{in} , for $FR = 60\%$ and $\alpha = 0^\circ$.

4.3 Flow pattern transition

4.3.1 Effect of heat load and filling ratio

Visual observations of flow patterns across the whole range of tested operating conditions are summarized in the flow pattern maps shown in Figure 4.3a for operation at $\alpha = 0^\circ$ and Figure 4.3b for operation at $\alpha = 45^\circ$. These indicate the influence of filling ratio, heat input, and CLPHP orientation on the two-phase flow pattern in the device. As described in Chapter 2, the operation of CLPHPs, and PHPs in general, is characterized by a non-linear stochastic component and thus universally applicable transition boundaries cannot be defined.

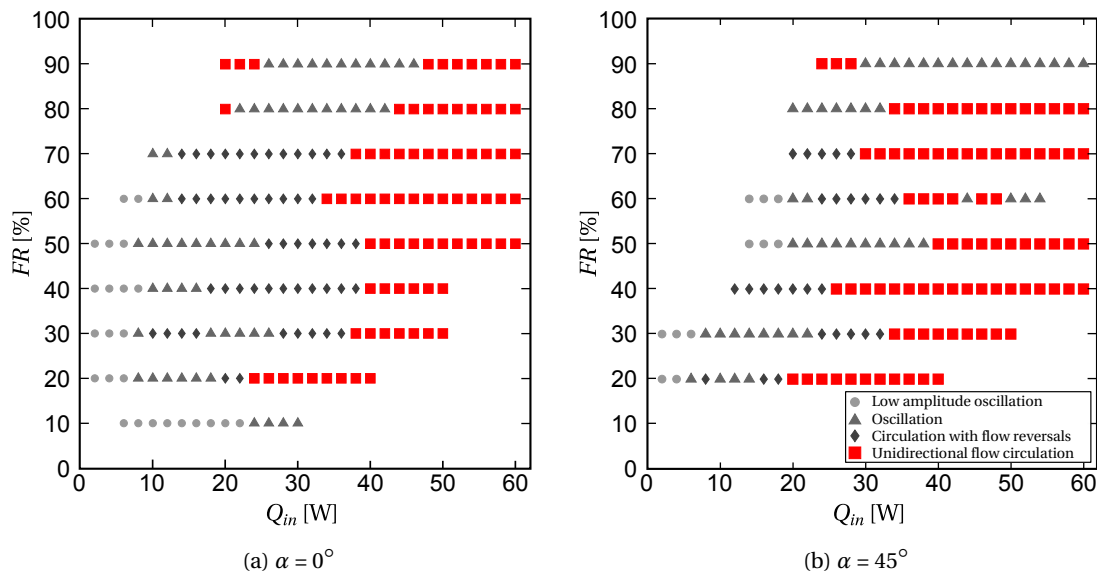


Figure 4.3: Flow pattern map for CLPHP operating at (a) Vertical Evaporator Down (VED) position $\alpha = 0^\circ$ and (b) at $\alpha = 45^\circ$.

The unidirectional circulation flow pattern (marked in red in the flow pattern maps of Figure 4.3) is recognized to be the most thermodynamically performant and thus the preferred operation mode, also in multi-turn PHPs (Mameli et al., 2014; Karthikeyan et al., 2014). It is therefore essential to identify the range of operating conditions producing this flow pattern for efficient practical applications. The present results indicate that:

1. In agreement with previous results in the literature, unidirectional circulating flow was attained at high heat loads. Two exceptions, where unidirectional circulation stopped and the system reverted to oscillating flow with increasing heat loads, were observed while operating at $\alpha = 45^\circ$ and filling ratios of 60 % and 90%.
2. For vertical operation, in the low ($FR < 50\%$) and high ($FR > 50\%$) filling ratio domains, the critical heat load for transition to flow circulation increased with filling ratio. A trend

for this transition could not be established for operation at $\alpha = 45^\circ$.

3. At the highest filling ratios, direct transition from oscillating regime to flow circulation was observed.
4. Unidirectional *counter-clockwise* circulation was preferred, with only one exception at $FR = 80\%$ and $\alpha = 45^\circ$.

4.3.2 Effect of system orientation

Visual analysis was carried out to assess to the effects of inclination on the system dynamics. For a given filling ratio and heat input the system was operated and the inclination α changed within the range 0 to 90° . For all of the tested conditions the system showed an oscillatory flow pattern, produced by nucleation and the ensuing expansion of the resulting Taylor bubbles, similar of the dynamics depicted in the time-strips of Figure 6.3.

4.4 Flow pattern dynamics

4.4.1 Synchronized visual and thermal measurements

High frequency temperature measurements were carried out during the operation of the CLPHP. The experimental procedure and measurement is discussed in Chapter 3.

In order to help the analysis, the temperatures measured in the evaporator T_{evap} and in the condenser T_{cond} have been superimposed onto the synchronized time-strips, as shown in Figures 4.1 and 4.2. It can be seen that the two-phase flow dynamics had a repetitive pattern which is strictly coupled with the temperature variations. In particular, the steady state thermal oscillations occurring during the operation of this CLPHP depend on the flow pattern and heat flux, as also found in Tong et al. (2001), Khandekar and Groll (2003), Khandekar and Groll (2004), and Xu et al. (2005).

The frequency spectra of the *temperature signal* in the evaporator and condenser are reported in Figures 4.4a and 4.4b for vertical operation at a 60 % filling ratio respectively. The frequency spectra of the *time-strip intensity profile* at the corresponding positions ($z_{evap} = 200$ mm, $z_{cond} = 630$ mm) are reported in Figures 4.4c and 4.4d for the same operating conditions. Qualitatively, a good agreement between the fundamental frequencies of the temperature signals and those relative to the two-phase flow dynamics as computed from the time-strips can be observed, thus proving their strong coupling. A detailed analysis of such data is addressed in Chapter 5, where the relationship between system thermo-hydrodynamics and system performance is discussed.

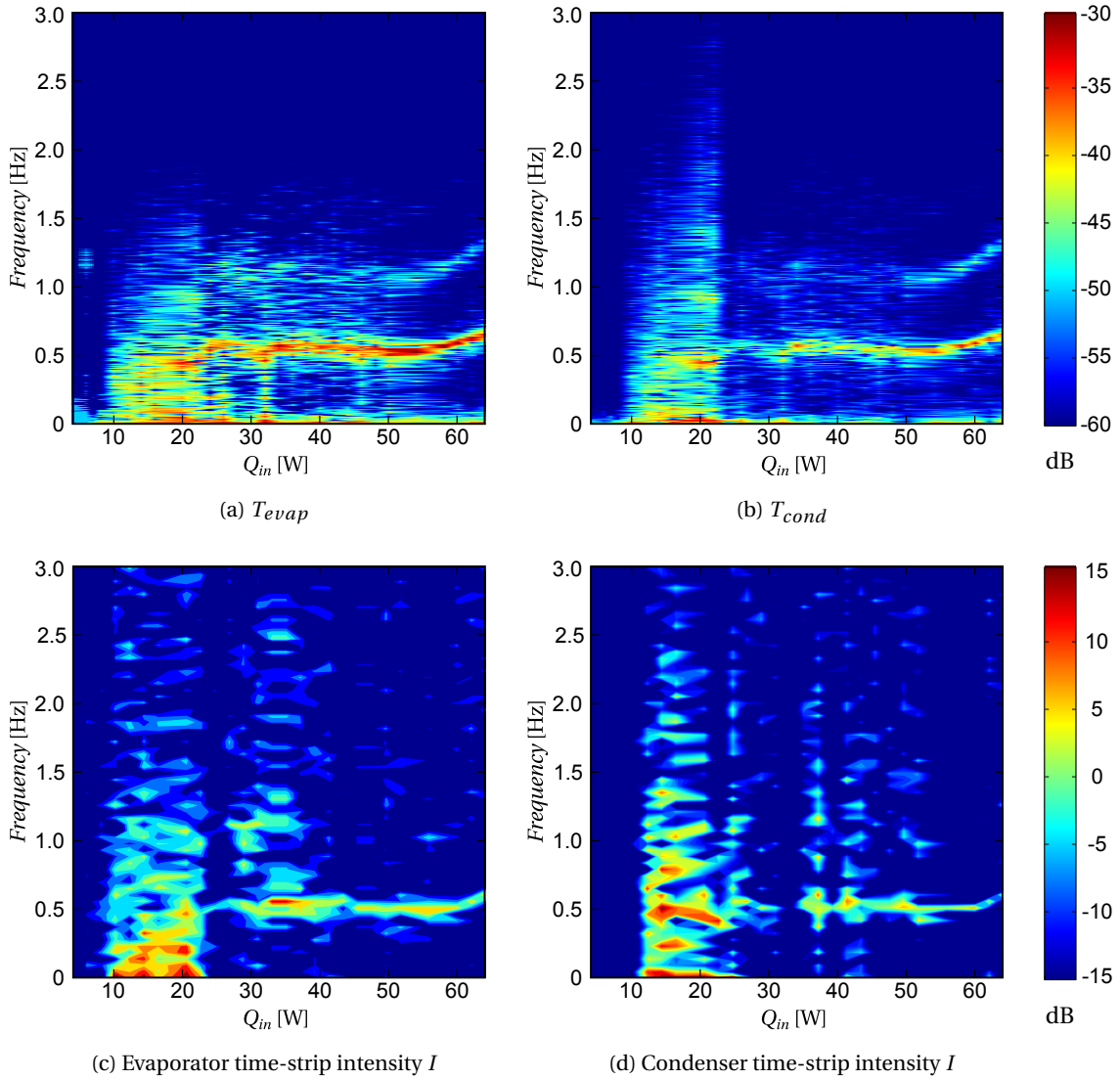


Figure 4.4: Frequency spectra of the high frequency temperature measurements and of the time-strip intensity in the evaporator T_{evap} (a) and (c), and condenser T_{cond} (b) and (d) for $FR = 60\%$ and $\alpha = 0^\circ$.

4.5 Conclusions

The results presented in this Chapter confirm the existence of a thermo-hydrodynamic coupling within the CLPHP device.

The thermal performance of the system will be qualitatively assessed in order to identify general trends relating it to flow pattern and flow dynamics and presented in Chapter 5. System dynamics, such as the mechanisms governing oscillatory flow, flow reversals and flow direction switch, are presented in Chapter 6.

5 CLPHP Thermo-hydrodynamics

5.1 Introduction

The present synchronized thermal and visual investigation proved to be a very powerful tool for the assessment of the thermal performance of the single-turn CLPHP. The measured thermal resistance of the system could in fact be correlated with the flow visualization results and with the high frequency temperature measurements. The coupled analysis of the thermal and flow behavior by means of spectral analysis is also addressed in this Chapter. Finally, an attempt to qualitatively estimate the heat transfer coefficient in the evaporator U-turn concludes the thermal analysis of the the single loop CLPHP.

5.2 Operational maps

The metric chosen for the qualitative evaluation of the system thermal performance as a function of inclination, filling ratio and heat input was its *resistance ratio* R_{ratio} , as defined by Eq. 3.5. From this definition, since high values of R_{ratio} correspond to low system thermal resistances, higher values of R_{ratio} indicate better thermal performance of the device.

Figure 5.1 shows the *operational maps* relative to vertical and inclined operation of the single loop CLPHP, where the flow pattern data obtained from visual investigation are coupled with the measured thermal resistances. The following trends, confirming the results of previous experimental analysis (Khandekar and Groll, 2003; Khandekar et al., 2004; Mameli et al., 2011), are here identified:

- Generally, for a given filling ratio the thermal resistance decreases with increasing heat input and the consequent transition to unidirectional circulating flow. This flow transition in particular yields a significant improvement of thermal performance due to annular/semi-annular flow developing in the evaporator;
- For a given heat input, there is a progressive deterioration of thermal performance with increasing filling ratio, and thus increasing liquid inventory. This corresponds to an increase in the proportion of heat transferred by sensible heat relative to latent heat,

due to reduction of the formation of annular flow and eventually elongated bubbles as filling ratio increases.

- At filling ratios lower than 50 % the thermal resistance increases at high heat loads. In fact, the combination of low liquid inventory and its segregation in the condenser at the top of the device can eventually lead to local dry-out in the evaporator;
- The thermal resistance measured for vertical operation (Figure 5.1c) is generally lower than for an inclined system (Figure 5.1d) for the same heat input and filling ratio, thus suggesting gravitational forces influence on the flow dynamics and system thermal performance.

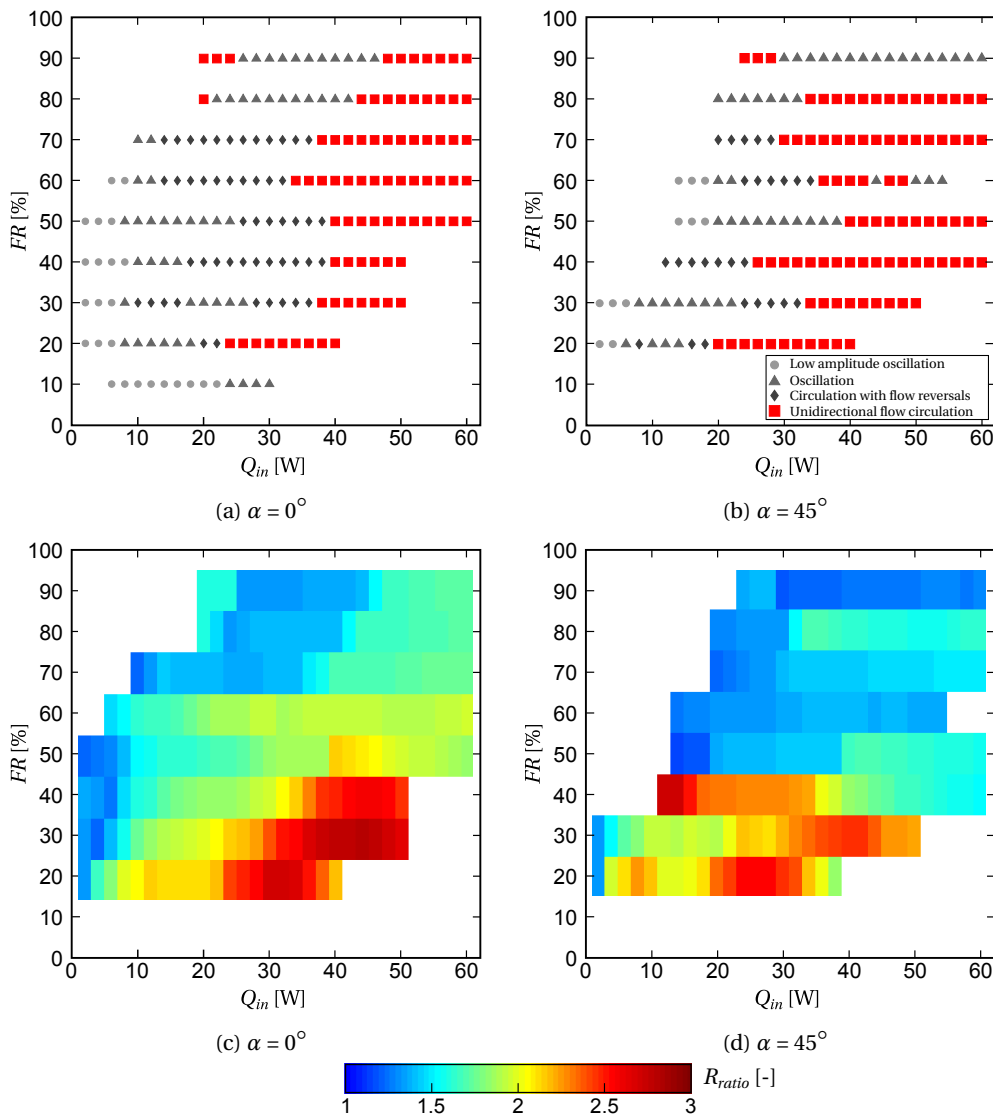


Figure 5.1: Flow pattern maps for the CLPHP operating at (a) Vertical Evaporator Down (VED) and (b) $\alpha = 45^\circ$ positions. Thermal performance maps showing R_{ratio} trends for (c) Vertical Evaporator Down (VED) and (d) $\alpha = 45^\circ$ orientations.

5.3 Thermal performance and two-phase flow dynamics

The spectral content of the fluctuating temperature data reveals information about the characteristics of the two-phase flow which can then be compared to the thermal resistance of the PHP effect R_{PHP} (Eq. 3.4).

Figures 5.2a and 5.2b show the frequency spectra of the fluctuating temperature difference ΔT between the evaporator and condenser for operation at $FR = 20\%$ and heat input Q_{in} varying within the range from 2 to 40 W, for vertical and inclined operation. The resistance R_{PHP} and the observed flow patterns, relative to the same operating conditions, are reported in Figures 5.2c and 5.2d.

Similar trends for vertical and inclined operation at a filling ratio of 20 % are observed in the thermal and flow dynamics frequency behavior. At low heat loads, oscillation amplitudes and frequencies are seen to increase, producing a progressive reduction of the thermal resistance. Increasing the heat input to 18 W for vertical operation and to 14 W for inclined system, nucleation followed by rapid expansion of bubbles produces oscillatory flow. A liquid slug oscillates about the evaporator U-turn and dry patches are formed in the evaporator, leading to a deterioration of the thermal performance. The latter lasts until unstable circulating flow brings a more uniform liquid-vapor distribution within the system, at 20 and 16 W respectively. The evaporator wall is now rewetted and the resistance progressively decreases with increasing heat loads and the consequent transition to unidirectional circulating flow. The frequency spectra of both temperature and flow data suggest the increase of the dominant frequency components and thus the higher convective heat transfer rates up to 34 and 32 W. At this point, low liquid inventory combined with high heat inputs, produces the evaporator dry-out which is known to reduce the pumping power and the system thermal performance. The low oscillation amplitudes in the frequency spectra of Figures 5.2a and 5.2b confirm this trend.

At high filling ratios ($FR > 50\%$) the thermal resistance is seen to decrease with increasing heat loads over the whole range of tested heat inputs, as confirmed by the data reported in Figures 5.3c and 5.3d for operation at a 60 % of filling ratio. In these conditions, the liquid inventory is such that much higher heat loads are necessary for dry patches to occur in the evaporator, but higher single phase liquid heat transfer rates are present as indicated by the lower thermal performances. As reported in the flow pattern maps of Figure 5.1a and 5.1b, vertical and inclined operation produce different flow pattern transitions and thus different thermal behavior. The gradual improvement of thermal performances with increasing heat load in the annular flow regime is shown in Figure 5.3c for $Q_{in} > 14$ W and vertical operation at $FR = 60\%$, whilst the effect of the transition to slug flow at high heat fluxes is visible in Figure 5.3d for inclined operation at the same filling ratio.

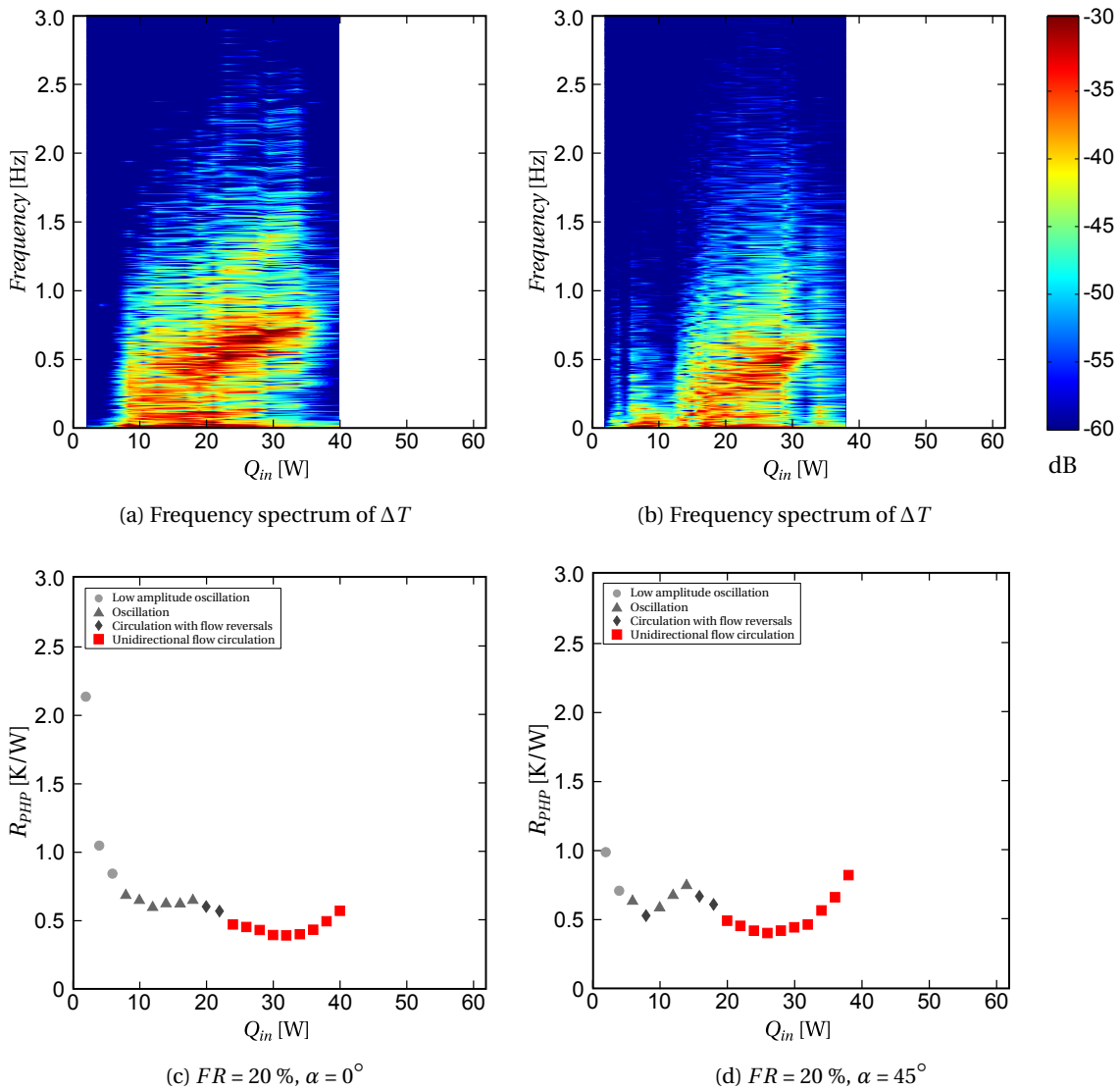


Figure 5.2: Frequency spectra of the temperature difference ΔT and resistance of the PHP effect R_{PHP} versus heat load Q_{in} when operating at $FR = 20\%$ for vertical (a) and (c), and inclined operation at $\alpha = 45^\circ$ (b) and (d).

The resistance R_{PHP} for vertical operation at $FR = 60\%$ (Figure 5.3c) shows two major changes in its slope. The first occurs at a heat load of 24 W for unstable circulating flow where flow reversals are less frequent and unidirectional flow lasts longer, as suggested by the cleaner frequency spectra. Annular flow can be here considered the main flow pattern, as for the unidirectional circulating flow establishing at a heat load of 34 W. A second slight change in the resistance slope is observed at heat loads higher than 54 W. The oscillation frequency starts to increase, and the oscillatory component associated with the 'local flow direction switch' reduces, producing an improvement of the system thermal performance, as described in Section 6.4.3.

5.3. Thermal performance and two-phase flow dynamics

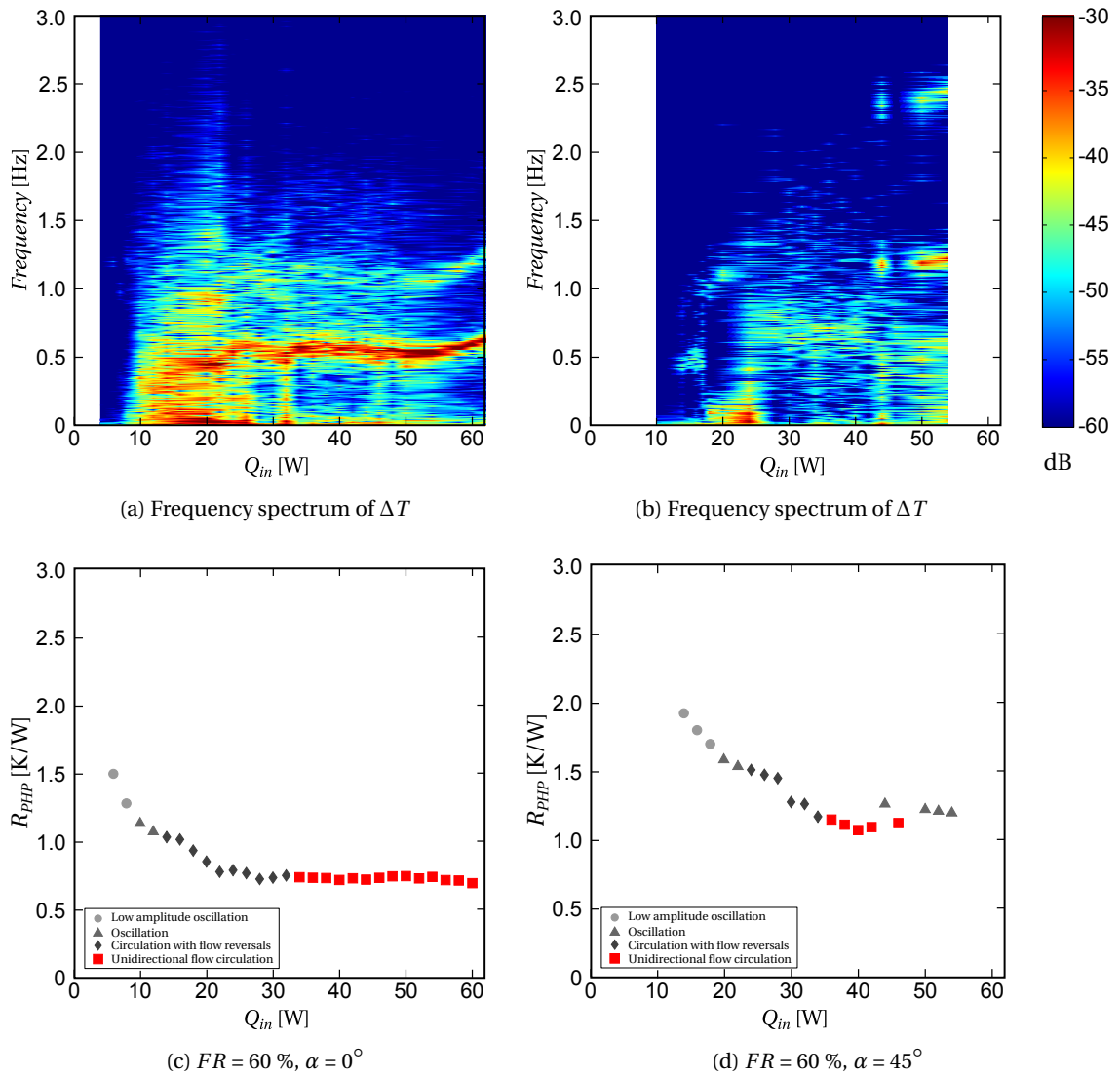


Figure 5.3: Frequency spectra of the temperature difference ΔT and resistance of the PHP effect R_{PHP} versus heat load Q_{in} when operating at $FR = 60\%$ for vertical (a) and (c), and inclined operation at $\alpha = 45^\circ$ (b) and (d).

During inclined operation at $\alpha = 45^\circ$ for $FR = 60\%$, the oscillating flow regime was restored at the highest heat inputs tested. The effect of this flow pattern transition on the dynamics can be seen in the resistance trend of Figure 5.3d and in the frequency spectrum of Figure 5.3b. Oscillatory flow, produced by the expansion of nucleated bubbles (Section 6.3), is characterized by a long liquid slug oscillating about the evaporator U-turn. Therefore, the single-phase liquid heat transfer component occurring in the evaporator in this case is higher than for the annular flow case, thus producing a slight deterioration of the thermal performance.

The effect of the inclination angle α on the system performance for constant heat inputs of 30 and 40 W at a filling ratio of 60 % was further investigated and the results are shown in Figure 5.4a. As it can be seen, there is a significant increase in the thermal resistance of the device with increasing inclination angle. Furthermore, in agreement with Xu et al. (2006), the performance difference between vertical and horizontal operation diminishes with increasing heating power and filling ratio, thus confirming the hypothesis that thermally induced forces are responsible for producing the two-phase oscillating flow (Hemadri and Khandekar, 2009). The dominant oscillation frequencies are also seen to decrease with inclination, further highlighting the potential effect of gravity on the operation of the system, as described in Chapter 6.

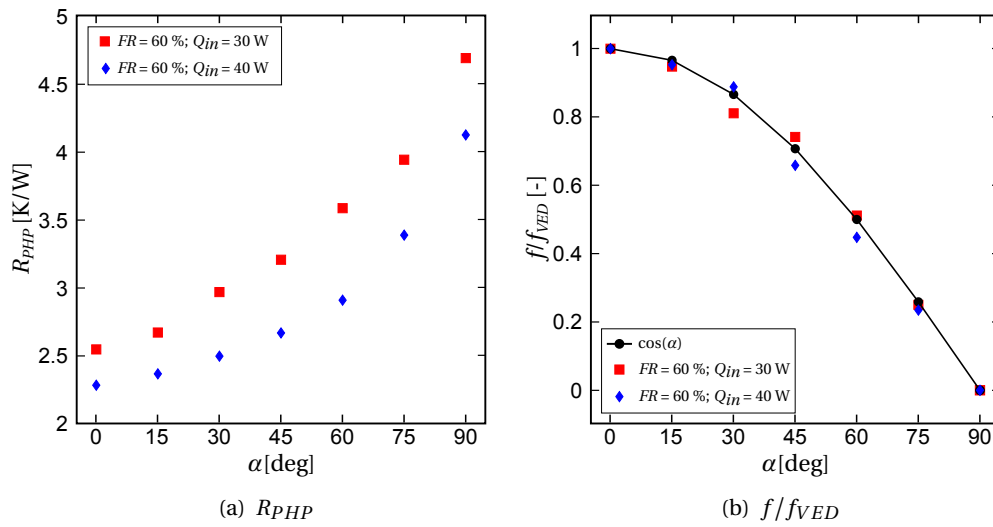


Figure 5.4: Resistance of the PHP effect R_{PHP} (a) and dominant frequency component (b) for different inclination angles α and operation at $FR = 60$ % at 30 and 40 W heat inputs.

5.4 Thermo-hydrodynamics in a single-turn CLPHP

The synchronized thermal and visual investigation technique, implemented in the framework of this research work, allows the analysis of the thermal and hydraulic behaviors of the single loop CLPHP by means of the spectral analysis of the acquired data, as described in Section 4.4.1. Namely, the thermal behavior reported in the frequency spectra of the evaporator and condenser temperatures can be compared with the frequency spectra computed from the intensity of the time-strip at the corresponding positions. This analysis is further enhanced by also considering the time-averaged temperatures of the evaporator \bar{T}_{evap} and condenser \bar{T}_{cond} .

Figure 5.5 describes the operation of the single loop CLPHP at a 20 % of filling ratio when operated vertically. At such low filling ratios, the stiffness of the system is very low and any flow perturbation can propagate throughout the device and thus globally affect the two-phase flow dynamics. This can be seen from the existence of similar spectra components in the evaporator and condenser fluctuating temperature, as shown in Figures 5.5a and 5.5b.

5.4. Thermo-hydrodynamics in a single-turn CLPHP

Figure 5.5 indicates that as the heat input is increased the evaporator and condenser temperatures increase until at $Q_{in} = 8$ W they begin to display large amplitude oscillations. This corresponds to a change in the flow regime from low amplitude oscillations to oscillations, as evident from the time-strip intensity spectra. The broad band featureless spectra obtained up to $Q_{in} = 22$ W indicates that the temperature and the two-phase flow oscillations are non-periodic in nature. At higher heat inputs, the spectra become well defined, with only a dominant frequency at around 0.7 Hz and its harmonics, thus indicating the presence of stable periodic behavior. This transition can be seen to correspond with a flow regime transition to unidirectional circulation. With further increases in heat load, the temperature of the evaporator and condenser continue to increase at a constant slope until $Q_{in} = 36$ W. Above this heat load, there is an increase in the slope of the evaporator temperature trend. This corresponds to the disappearance of spectra activity within the evaporator and condenser sections, which is due to the progressive dry-out of the evaporator, as shown in Figure 5.2.

Figure 5.6 indicates a quantitatively similar behavior when the CLPHP is inclined at $\alpha = 45^\circ$.

Figure 5.7 shows the frequency spectra of the evaporator and the condenser wall temperatures and of the time-strip intensities for vertical operation at a 60 % of filling ratio. It can be seen that the evaporator and condenser share the same frequency components albeit with significantly different amplitudes. Dominant frequencies range from 1.2 Hz for the small amplitude oscillation regime to $\cong 0.6$ Hz for the circulating flow regime.

Within the heat load range of 6 to 8 W, the system shows low amplitude oscillations produced by the cyclic creation and expansion of Taylor bubbles in the evaporator. The temperature signal in the evaporator is seen to oscillate at a frequency of 1.2 Hz, whilst in the condenser the oscillating liquid/vapor interface remains in proximity of the thermocouple and the amplitude of the temperature oscillation is negligible, as shown in Figure 4.2a.

When the two-phase flow oscillates with larger amplitude ($[10,12]$ W heat load), the oscillation frequency can change significantly with time and no dominant components are then computed. A wide spectral band in the frequency spectra is also visible for the unstable circulation with flow reversals regime, found for Q_{in} within 14 and 32 W. Each time unidirectional flow occurs, or the flow direction changes, the condenser temperature peaks during annular flow in both directions or drops when subcooled liquid is pushed back into the U-turn (Figure 4.2c), whilst the evaporator temperature drops when colder flow is pushed into the U-turn.

As suggested by the spectral behavior of both thermal and flow data, at low heat loads flow reversals could happen with no periodicity, whilst, starting from 24 W, flow reversals are less frequent. Unidirectional flow circulation lasts longer, resulting in cleaner frequency spectra. The mean evaporator and condenser temperatures increase at a lower rate with heat input, as shown by the reduced slopes in Figures 5.7e and 5.7f.

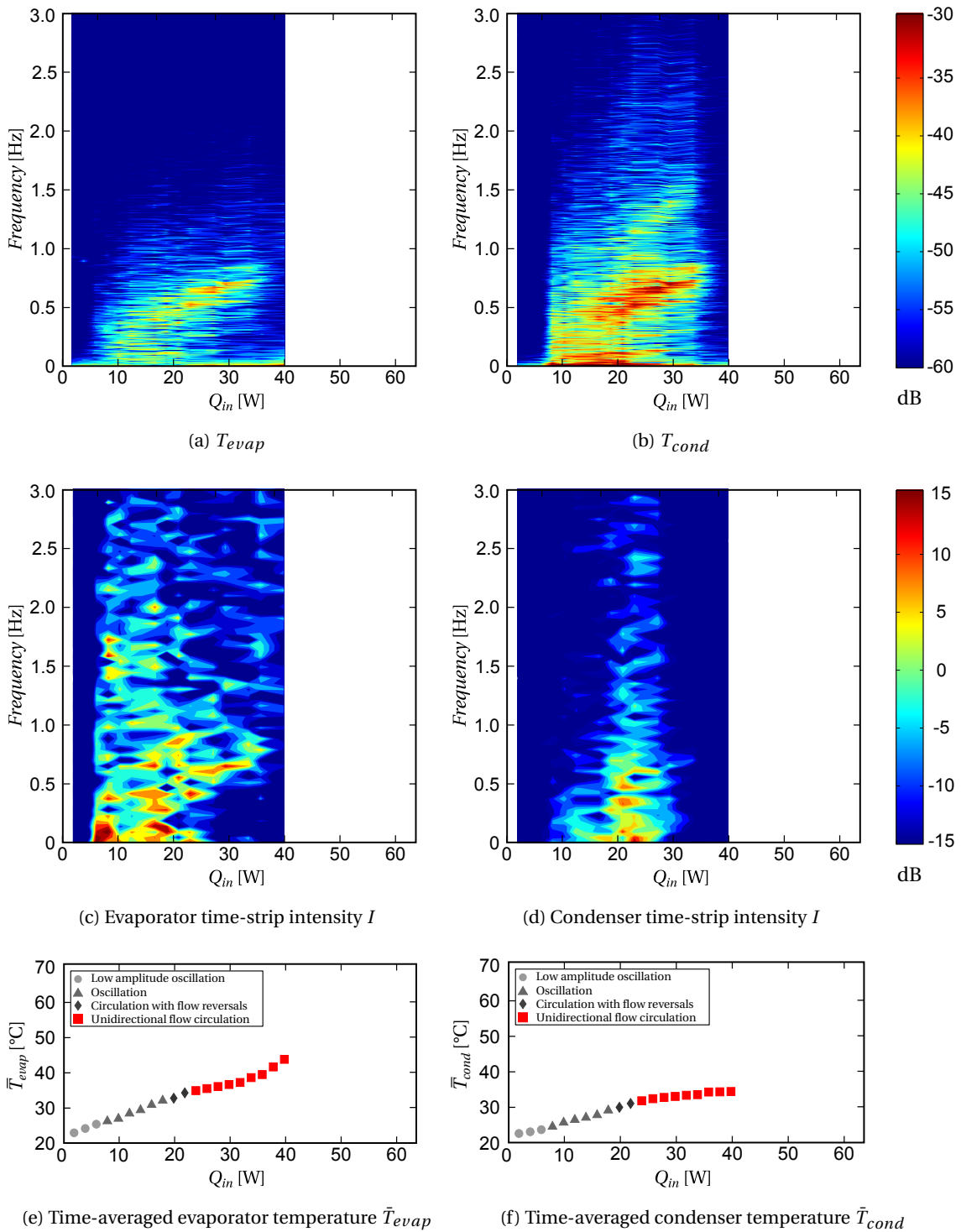


Figure 5.5: Frequency spectra of the high frequency temperature measurements and of the time-strip intensity I of the evaporator (a) and (c), and of the condenser (b) and (d). Time-averaged temperatures of the evaporator \bar{T}_{evap} (d) and condenser \bar{T}_{cond} (e). $FR = 20\%$, $\alpha = 0^\circ$

5.4. Thermo-hydrodynamics in a single-turn CLPHP

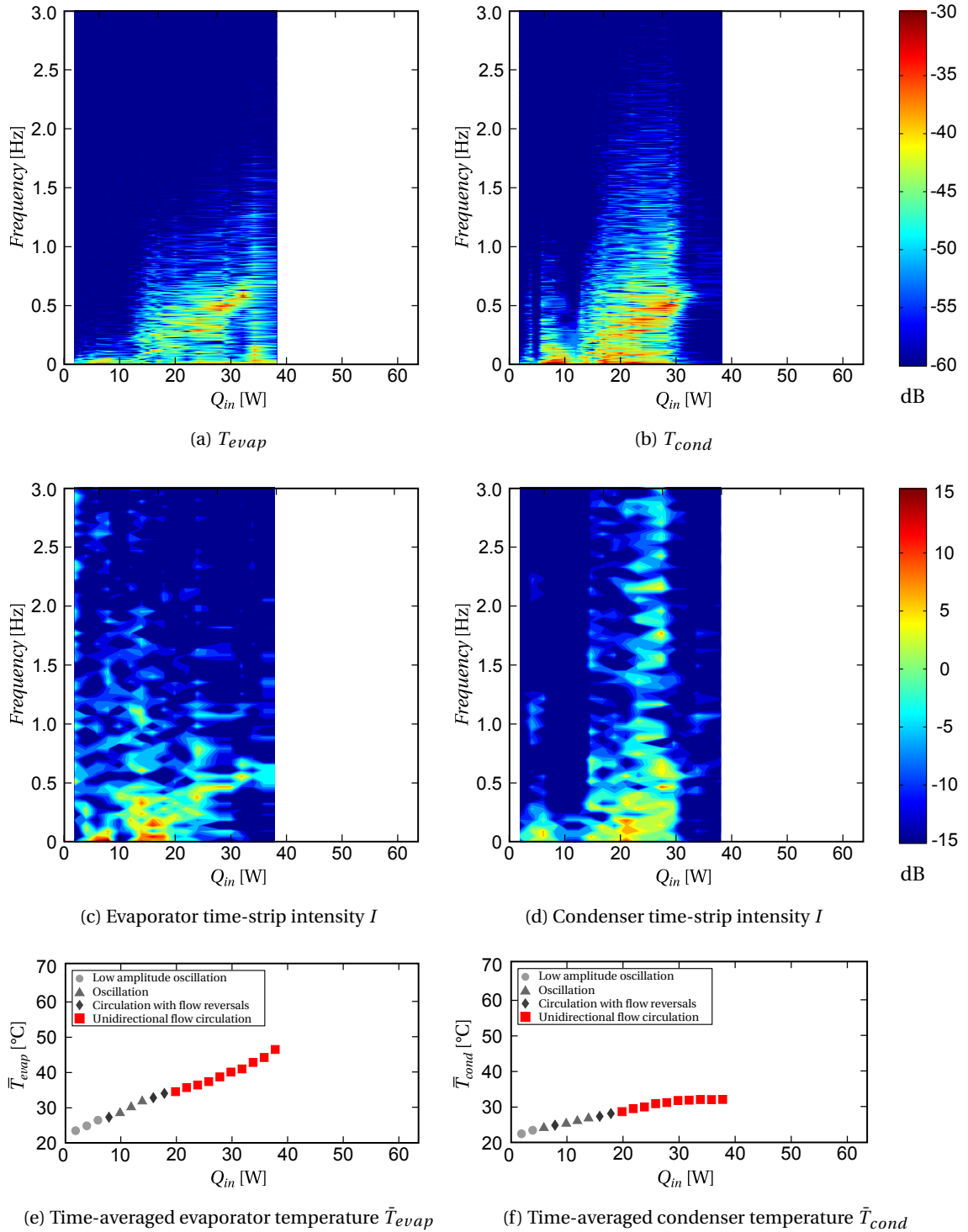


Figure 5.6: Frequency spectra of the high frequency temperature measurements and of the time-strip intensity I of the evaporator (a) and (c), and of the condenser (b) and (d). Time-averaged temperatures of the evaporator \bar{T}_{evap} (d) and condenser \bar{T}_{cond} (e). $FR = 20\%$, $\alpha = 45^\circ$

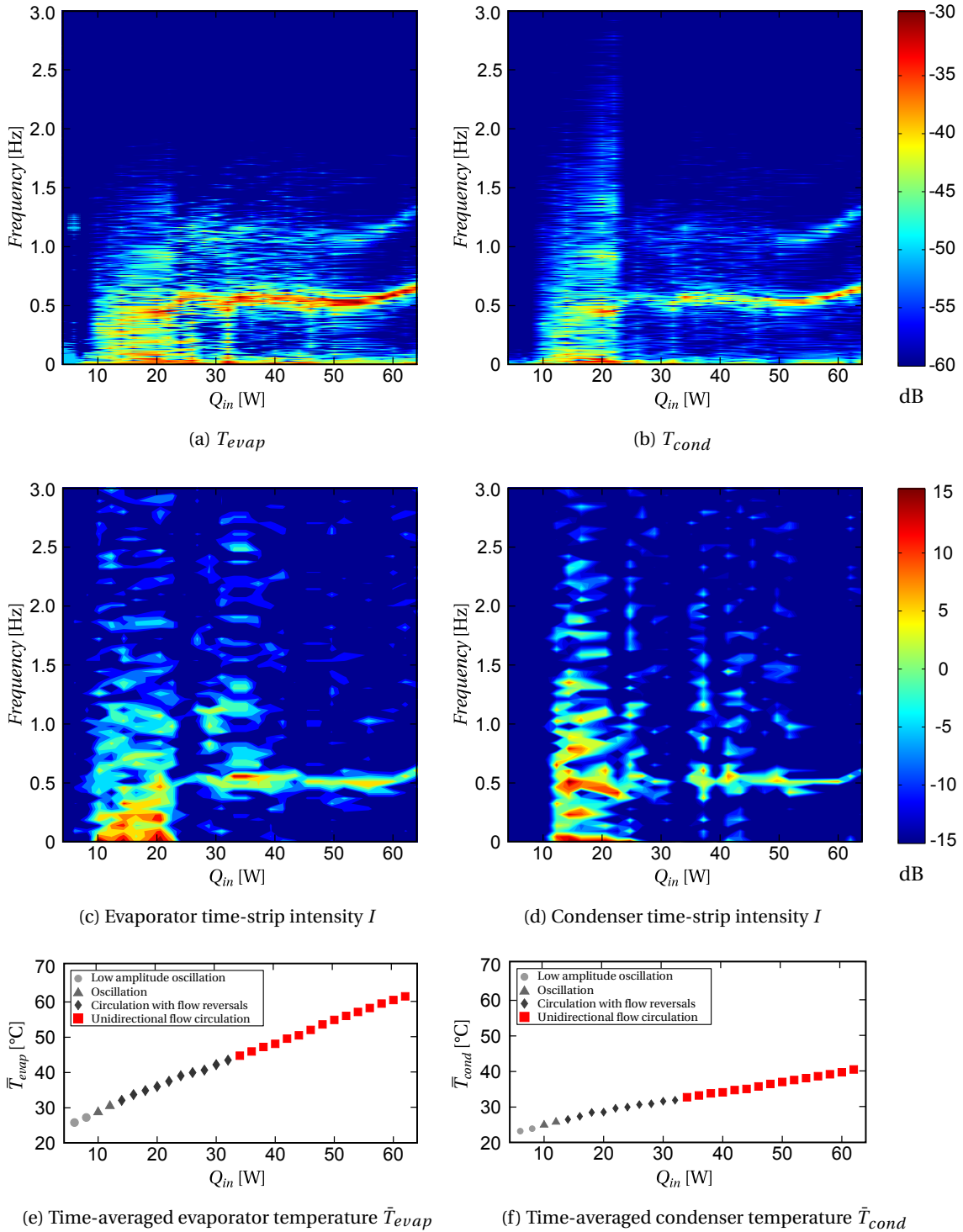


Figure 5.7: Frequency spectra of the high frequency temperature measurements and of the time-strip intensity I of the evaporator (a) and (c), and of the condenser (b) and (d). Time-averaged temperatures of the evaporator \bar{T}_{evap} (d) and condenser \bar{T}_{cond} (e). $FR = 60\%$, $\alpha = 0^\circ$

5.4. Thermo-hydrodynamics in a single-turn CLPHP

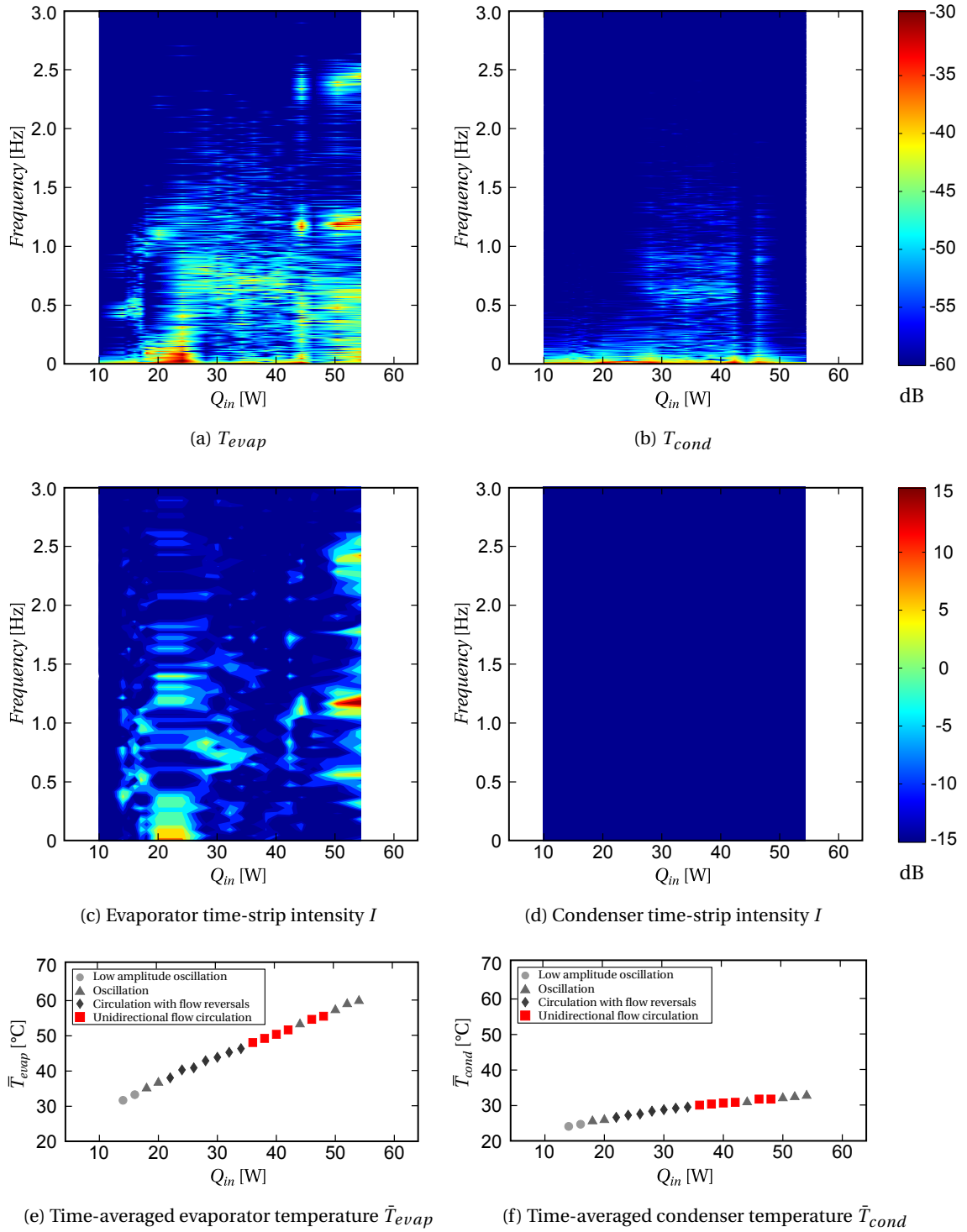


Figure 5.8: Frequency spectra of the high frequency temperature measurements and of the time-strip intensity I of the evaporator (a) and (c), and of the condenser (b) and (d). Time-averaged temperatures of the evaporator \bar{T}_{evap} (d) and condenser \bar{T}_{cond} (e). $FR = 60\%$, $\alpha = 45^\circ$

Unidirectional flow circulation was initiated at 34 W and shows a periodical behavior. The temperature profiles of Figures 4.1d and 4.1e show the cyclic rise in the evaporator temperature. The latter rises due to film thinning and their temperature drops when liquid returns and wets the evaporator channel walls. Similarly, the condenser temperature periodically peaks when annular flow appears in the condenser, as shown in Figure 4.2d. A low amplitude component of 1.2 Hz is superimposed on the fundamental oscillation component (0.6 Hz). The first is thought to be a consequence of the so called 'local flow direction switch' (Xu et al., 2005), whose duration is similar to one half period of the circulating regime of the same loop (Section 6.4.3).

In the whole unidirectional circulating-flow regime the frequency bandwidth is seen to change with heat load and to decrease significantly, starting from a heat load of 50 W. At low heat loads the system could be easily perturbed by local two-phase flow instabilities such as altered nucleation and expansion rates, bubble coalescence or breakage. At higher system energies, temperature and saturation pressure increase, making vapor plugs stiffer to compression and expansion. A narrow frequency bandwidth was observed and, from an applied heat load of 54 W, the dominant frequency increases significantly with heat load. Consistently, the system thermal performance improves, as suggested by the lower gradient in the mean evaporator temperature \bar{T}_{evap} of Figure 5.7e.

The spectral behavior of thermal and time-strip data relative to vertical operation at 60 % of filling ratio reflects the progressive transition to circulating flow while increasing the heat load.

As indicated by the frequency spectra of Figure 5.8, at 14 and 16 W of heat input, nucleation and expansion of bubbles in the evaporator propels the two-phase flow in an oscillating fashion at a frequency of 0.5 Hz. Increasing the heat input to 20 W, the system starts to oscillate at approximately 1.2 Hz, which is the oscillation frequency also at higher heat rates. Spectral bands around 1.2 Hz are in fact visible for operation at 44, 50, 52 and 54 W in the evaporator temperature data of Figure 5.8a and in the time-strips intensity data of Figure 5.8c. For the same conditions no dominant frequency can be computed in the temperature or time-strip data for the condenser where liquid is accumulated and no high temperature variation or interface motion in the time-strips can be captured.

Unstable and unidirectional flow circulation, taking place within the heat input range from 22 to 42 W, redistributes the liquid in the system volume. Frequency components around 0.6 Hz are in fact present in the temperature and time-strip intensity spectra for both evaporator and condenser.

5.4.1 Frequency analysis

A single *spring-mass-damper system*, as in Figure 5.9c, can be used to model the self-sustained two-phase flow motion in any PHP (Dobson, 2004; Sakulchangsattajatai et al., 2008) and to assess its frequency behavior. In the single *spring-mass-damper system*:

- The spring of stiffness k is representative of the compressible volume in the PHP. It is affected by the filling ratio FR and by the system pressure, which is in turn also affected by the heat input Q_{in} .
- The mass m represents the charged liquid inventory and depends on the filling ratio FR .
- The damping action c represents the total flow resistance developing during the self-sustained two-phase flow motion.

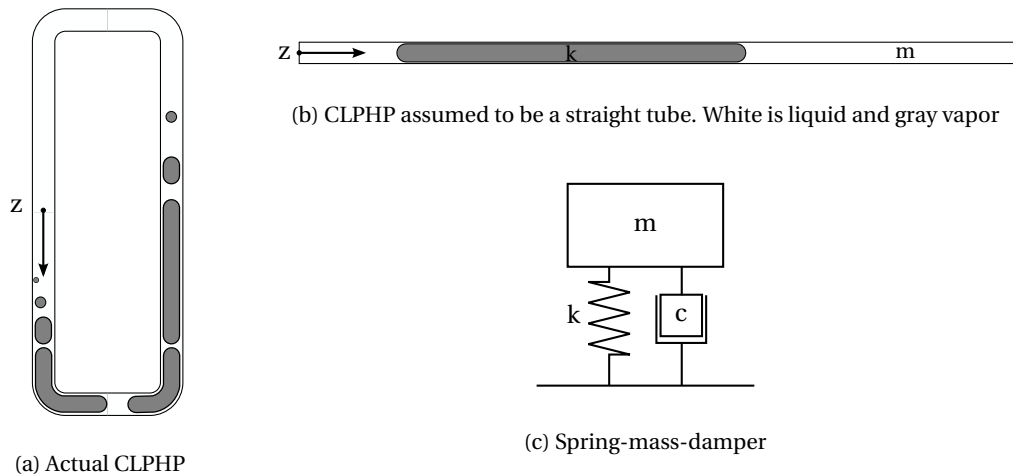


Figure 5.9: Single spring-mass-damper system applied to CLPHP. (a) Actual CLPHP, (b) simplified CLPHP assumed to be a straight tube, and (c) Spring-mass-damper system.

The natural oscillation frequency of such system is known to be equal to $\sqrt{\frac{k}{m}}$ and thus it increases with increasing system stiffness k and with decreasing mass m (Giovagnoni, 2001). For a given filling ratio, therefore mass of the system, higher heat inputs increase the system pressure and the stiffness of the vapor plugs. Higher frequencies are then observed with increasing heat loads, as indicated by the frequency spectra of Figures 5.5a and 5.6a for vertical and inclined operation at a 20 % filling ratio.

The frequency spectra of Figure 5.5a for operation at $FR = 20\%$ and $Q_{in} = 30\text{ W}$ show wide spectra bands around 0.7 Hz, while a narrow spectral band is observed around 0.6 Hz at a 60% filling ratio for the same heat load (Figure 5.7a). The wide spectral bands at the low system mass suggest low stiffness. The higher frequencies are in this case produced by the lower mass

the system has to displace.

Comparing the spectral bands of Figures 5.7a and 6.10a, for operation at 60 and 70 % filling ratios respectively, higher frequencies were observed at the highest filling ratios. In this case the reduced size of the compressible volume, and the higher operating temperature for the same heat load neutralize the effect of the increase of mass.

Utilizing the same approach, the effect of the working fluid can be analyzed. For a given set of operating conditions, the physical properties of the fluid can affect the total mass charged into the system, which mainly depends on the liquid density, and the system stiffness which is dependent on the pressure and density of the vapor phase at the given temperature.

5.5 Qualitative analysis of the heat transfer in the evaporator U-turn

The information contained in the operational maps are relevant when the best operating conditions of such system have to be decided. Given the maximum heat input to be processed by a single-loop PHP of the same geometry and material, and the operating temperatures, the range of applicable filling ratios could be qualitatively assessed in relation to the flow pattern offering the best thermal performance. The final choice of the operating conditions, however, also depends on safety considerations during operation. Low filling ratios, for instance, offer better thermal performance but could lead to evaporator dry-out and system failure.

For larger systems, such as multi-turn PHPs, a holistic approach should be utilized. The technique described in this Chapter could be used in future parametric experimental studies in order to identify the major trends in flow pattern transition and the relative two-phase flow-dynamics. Local flow velocities and frequencies could be coupled with measurements of the local heat transfer coefficients in the evaporator to implement, verify and validate mechanistic models of the heat and mass transfer in PHPs.

An approximate attempt to predict the local time-averaged heat transfer coefficient in the evaporator U-turn is made here by applying a state-of-the-art *mechanistic* model for evaporation of elongated bubbles in microchannels (Thome et al., 2004). The obtained local and averaged results are used to qualitatively assess the heat transfer characteristics. The rate of sensible and latent heat exchanged can be in fact estimated for the different flow patterns. The input data for the *3-zone model*, such as the two-phase flow velocities, liquid slug and vapor lengths, together with the residence time for liquid and vapor phases are obtained from the analysis of the time-strips, as described in Section 3.5.1 and in Appendix B.

Figure 5.10a and 5.10b show the computed local time-averaged heat transfer coefficients due to single-phase liquid heat transfer $h_l(z)$, two-phase thin-film evaporation $h_{film}(z)$ and single-phase vapor heat exchange $h_v(z)$. The Figures also show the relative time-strips for slug-flow oscillation and for circulating semi-annular flow in the evaporator U-turn. Figure 5.10c and 5.10d show the total local heat transfer coefficient $h(z)$ as computed from Eq. B.1.

5.5. Qualitative analysis of the heat transfer in the evaporator U-turn

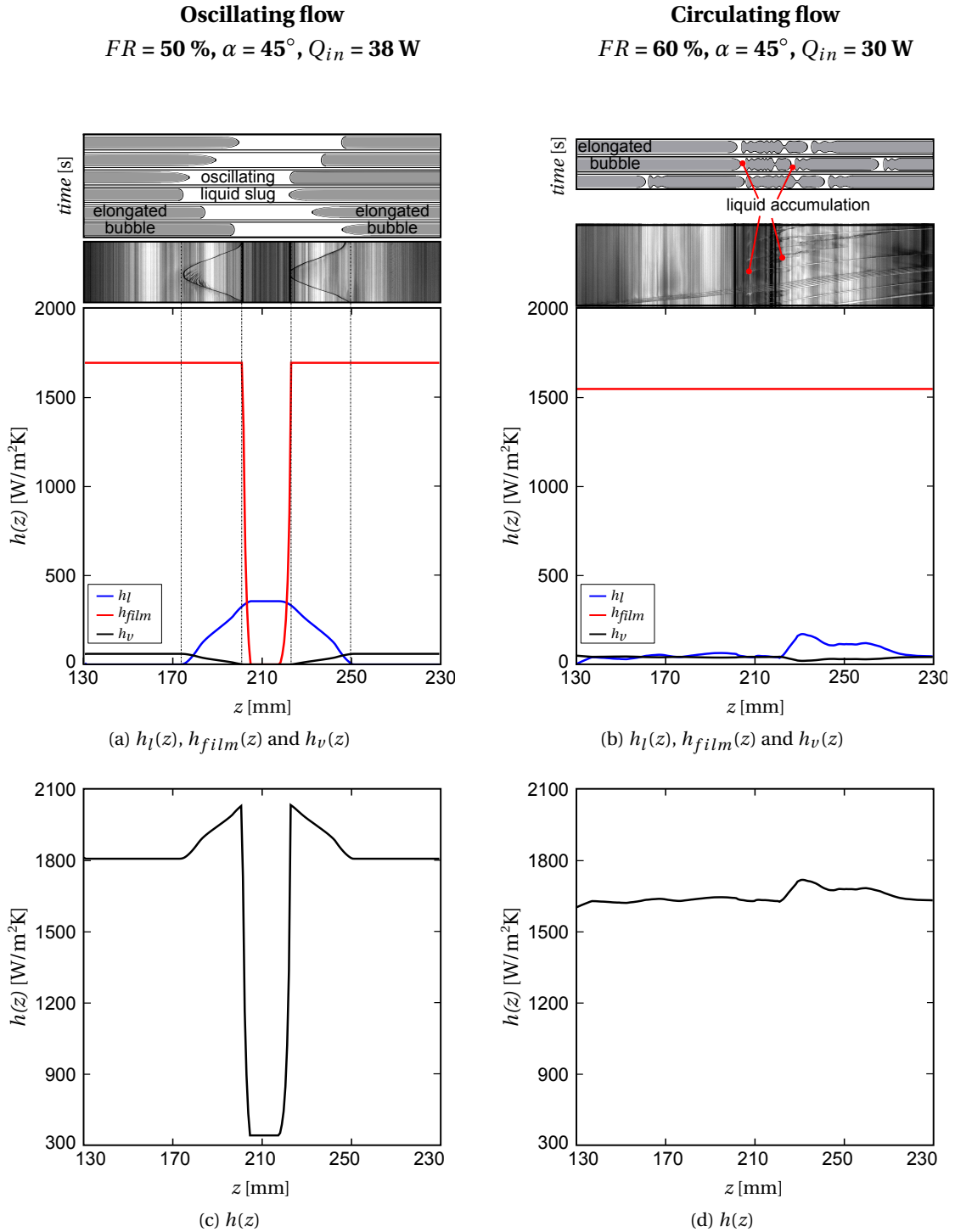


Figure 5.10: Time-strips and local time-averaged heat transfer coefficients (a) and (b) computed for single phase liquid heat transfer $h_l(z)$, two-phase thin film evaporation $h_{film}(z)$, and single-phase vapor $h_v(z)$, and local total heat transfer coefficient $h(z)$ (c) and (d), for operation at $FR = 50\%$, $\alpha = 45^\circ$, $Q_{in} = 38\text{ W}$ and $FR = 60\%$, $\alpha = 45^\circ$, $Q_{in} = 30\text{ W}$.

The effect of film thickening after the passage of the liquid slug in oscillating flows can be observed in Figure 5.10a. Far from the rewetting zone (z within 176 and 252 mm), the thin film completely evaporates and dries out, thus the single-phase vapor heat transfer coefficients are almost constant. Within the rewetting zone, where the liquid slug periodically swipes the channel walls, the dry-out component reduces, and the time-averaged film thickness is higher. Moreover, the periodical switch of the flow momentum producing the oscillatory flow prevents the liquid slug from escaping from the bottom of the U-turn. Within the z range from 207 to 222 mm, the heat transfer coefficient experiences a minimum and only liquid is exchanging heat with the channel walls.

For the circulating flows, the time-strip of Figure 5.10b suggests the presence of thin-films with periodical rewetting and liquid accumulation at the bottom of the U-turn. As suggested by the single-phase liquid and vapor heat transfer coefficients, the liquid which is observed to return from the channel corners and to accumulate in the evaporator U-turn helps delay dry-out and thus locally enhance the heat transfer.

The results presented here are strongly related to the prediction of the dry-out condition. The latter is computed given the initial and minimum film thickness of the elongated bubble. The correlation suggested by Thome et al. (2004), which was experimentally validated and corrected against a wide-range of channel geometries and diameters, gives very low values of the initial film thickness. Qualitative observation of the film-dynamics in the CLPHP suggested much larger values. For this reason, the initial value of the film thickness is computed according to the correlation proposed by Aussillous and Quere (2000) for 1 mm diameter square-section channels.

The strong dependence of the obtained results on this parameter is such that only qualitative trends can be derived based on them. For the development of new mechanistic PHP models, further experimental investigation on the film laying mechanism is required, whilst experimental heat transfer coefficients are necessary for the final adaptation of the present model to the PHP case and for its final validation.

Figure 5.11 shows the space-time averaged heat transfer coefficient relative to the single-phase liquid, thin-film evaporation and single-phase vapor heat exchange, computed at different heat loads Q_{in} for inclined operation at a 60 % of filling ratio. The effect of flow pattern is evident, qualitatively confirming the trends observed in Figure 5.3d:

- Low single-phase liquid and thin-film heat transfer coefficients are characteristics of the low amplitude oscillation flow regimes. The computed thermal resistances are in fact the highest obtained.
- Time-averaged heat transfer coefficients for the unstable circulation flow regime could not be obtained. The flow pattern and its flow-dynamics characteristics change considerably with time and thus the periodical features required as inputs to the model could not be computed.

5.5. Qualitative analysis of the heat transfer in the evaporator U-turn

- The dominant heat transfer mechanism for unidirectional circulating flow is observed to be the thin-film evaporation mechanism. The average heat transfer coefficients of sensible liquid and vapor phase are in fact very low.
- The rate of liquid heat transfer, as computed from the *3-zone model*, is seen to considerably increase for the oscillating slug-flow regime, in agreement with the higher values of the thermal resistances measured for this case.

Further observations on these results must take into consideration the validity of the assumptions on which the *3-zone model* (Thome et al., 2004) is based, with respect to PHP thermo and flow-dynamics:

- The hypothesis that all the energy entering the system volume is used for evaporation is not always valid during PHP operation. In this case, in fact, the temperature within the oscillating liquid slug could be different from the saturation temperature, thus the relative heat rate estimated with this method is the minimum achievable;
- Ripples and liquid film bridging are observed in the evaporator, locally changing the film thickness. This phenomenon is visible in the time-strips but can only be partially captured by their post-processing. Depending on the image-processing filtering, this component could either be considered as liquid or vapor. According to the chosen parameters in this study, the liquid contribution to heat transfer is overestimated.

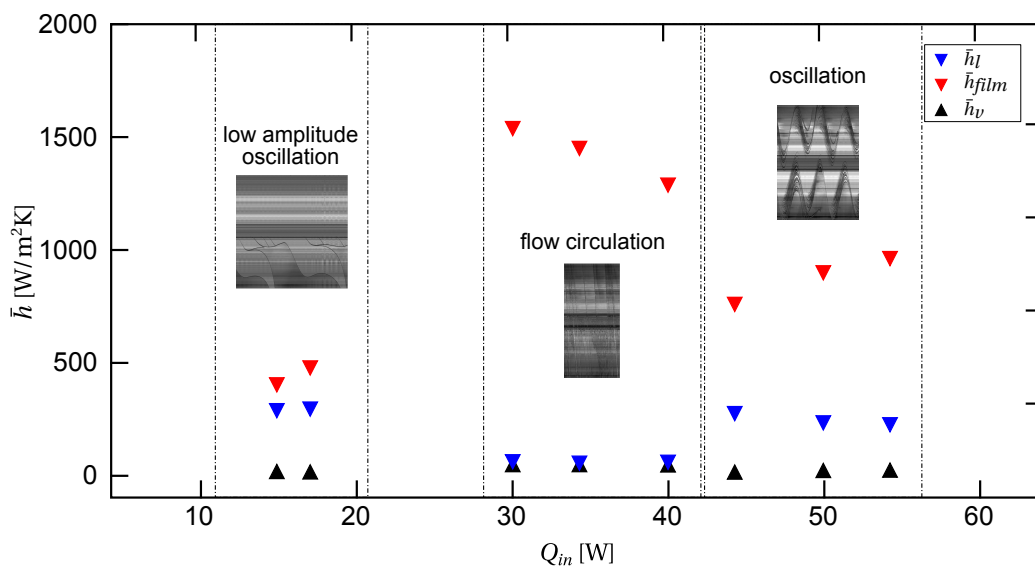


Figure 5.11: Average heat transfer coefficient of the single-phase liquid, thin film and single-phase vapor, computed for different heat loads when operating at $FR = 60\%$ and $\alpha = 45^\circ$

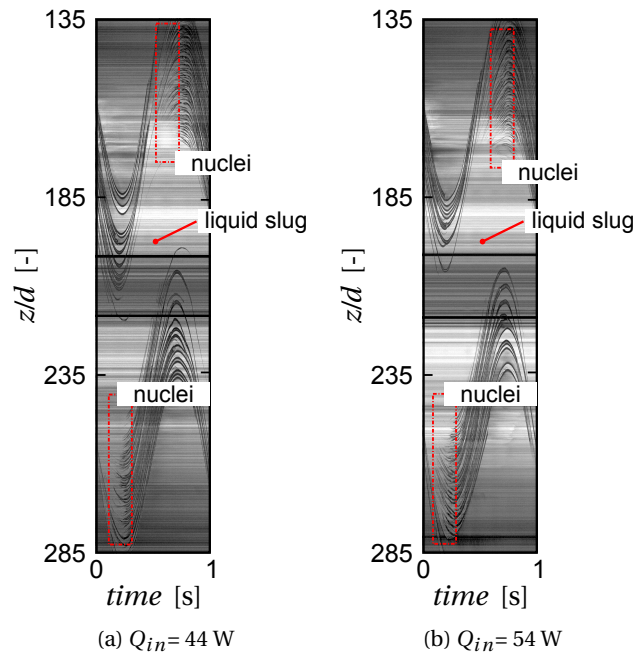


Figure 5.12: Time-strips showing oscillating slug flow with nucleation and growth of bubbles in the liquid slug. (a) $FR = 60\%$, $\alpha = 45^\circ$, $Q_{in} = 44\text{ W}$ and (b) $FR = 60\%$, $\alpha = 45^\circ$, $Q_{in} = 54\text{ W}$

As described later in Chapter 6, nucleation and rapid growth of bubbles from a liquid slug residing in the evaporator is observed to produce oscillating slug flow (Figure 6.2). Utilizing the same approach used in the *3-zone model*, the spatial location z where nucleation is observed to occur and its duration can be estimated from the analysis of the time-strips. Nucleation within the oscillating liquid slug, as depicted in Figure 5.12, can then be considered as a local enhancement of the heat transfer. For the two cases shown here, nucleation is visible at the leading edges of the liquid slugs, at $z > 160\text{ mm}$ in the left and $z < 255\text{ mm}$ in the right channel. Furthermore, the duration of the phenomenon is limited with respect to the whole oscillation period.

Measured values of the local heat transfer coefficient would help estimate the actual effect of nucleation on the overall heat transfer in this CLPHP evaporator. The nucleation process is known to be system dependent: A particular surface structure or a local defect could act as the nucleation site. Therefore, the obtained results could not be extended to other systems.

5.6 Conclusions

Self-sustained two-phase flow in PHPs is governed by phase-change phenomena, thus the overall system thermal performance is the result of the system thermo-hydrodynamics. The results of the synchronized visual and thermal investigation carried out on a single-turn PHP confirmed previously observed trends in the thermal performance with operating conditions and flow pattern. Novel quantitative information relating the thermal performance to the two-phase flow characteristics is provided by the high frequency measurements coupled with the flow visualization results. To complete the thermal analysis, the time-averaged heat transfer coefficients relative to single-phase liquid and vapor and thin-film evaporation heat transfer mechanisms have been qualitatively evaluated for different operating conditions, confirming previous results of the role of the flow pattern on the system thermal performance.

6 CLPHP Flow dynamics

6.1 Introduction

Self-sustained oscillatory two-phase flow in PHPs is attained as the result of the strong thermo-hydrodynamic coupling present within the device and has been observed to influence the operation and thermal performance of PHPs (Khandekar et al., 2010; Khandekar and Groll, 2004). This Chapter reports on the analysis of the net axial forces responsible for producing self-sustained two-phase flow motion, such as oscillatory and circulating flows, flow reversals and 'local flow direction switch'. Novel information regarding the mechanisms regulating flow pattern transition and the role of gravity for single loop CLPHPs operation are also provided.

6.2 Net forces acting on the two-phase flow in a single-turn CLPHP

The time-strip analysis implemented here provides novel qualitative and quantitative details about the flow dynamics of oscillatory and circulating flows. To better understand the phenomena underlying the flow motion in a single loop CLPHP, a static analysis of the forces acting on the system was carried out: Assuming the flow velocity uniform and constant, the only axial forces acting on the fluid are *net gravity* $F_{\vec{g}}$ and *frictional shear forces* F_{τ} .

In the close volume the system pressure tends to be equalized and the total void fraction must be constant. If evaporation produces bubble expansion and the consequent local increase in pressure, simultaneously the cooling process must produce a local contraction of the vapor volume and of the pressure. The *net pressure force* in the CLPHP volume is then zero.

Net gravity can be seen as the sum of the gravitational forces in the left $F_{\vec{g},L}$ and right $F_{\vec{g},R}$ tubes, as shown in Figure 6.1. To obtain positive counter-clockwise momentum of the two-phase flow, such as for counter-clockwise circulation, the equilibrium of the forces acting on the CLPHP flow can be written as:

$$F_{\vec{g},L} = F_{\vec{g},R} + F_{\tau} \quad (6.1)$$

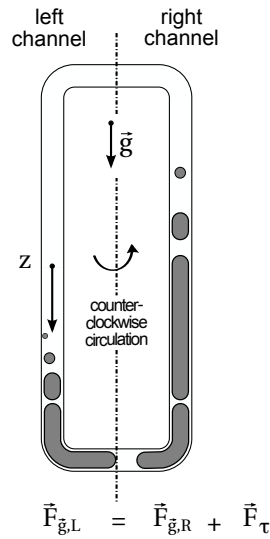


Figure 6.1: Net gravity producing counter-clockwise circulation (positive momentum) in a single loop CLPHP. White represents the liquid phase and gray vapor.

Positive counter-clockwise net momentum is thus reached when the average density in the left (*descending*) channel is higher than the one in the right (*rising*) channel, as depicted in Figure 6.1. To change the flow direction, thus reversing the net momentum in the loop, an imbalance of mass in the channels is needed until a new gravitational equilibrium and thus unidirectional flow circulation are restored. In such a system, the imbalance of mass can only be produced by a change in density (void fraction) in the channels, as a consequence to the change of liquid-vapor distribution in the system volume. To produce the imbalance condition stated by Eq. 6.2, where F'_{τ} represents the total friction force of the new state, nucleation and subsequent vapor generation must increase the void fraction of the left (descending) side to move mass to the right channel:

$$F_{\vec{g},R} > F_{\vec{g},L} + F'_{\tau} \tag{6.2}$$

During the reversal, until a new equilibrium condition is again established, the kinetic energy (velocity of expanding bubble) in the left tube must prevail over the potential energy and frictional losses in the whole loop; only in this case is a permanent flow reversal affecting the whole loop attained.

Oscillatory flow is characterized by the periodic fulfilling of the imbalance condition, thus causing a periodic reversal of the flow direction. The 'local flow direction switch', on the contrary, represents a particular case of flow reversals where the imbalance condition is only temporarily satisfied and flow circulation is finally restored.

6.3 Dynamics of the oscillatory two-phase flows

Thermally induced forces produce the impulse needed to start-up and later sustain the flow motion in the single-turn CLPHP. Nucleation and rapid expansion of the vapor bubbles was observed to produce the oscillatory flow in the CLPHP, in agreement with Tong et al. (2001), Cai et al. (2002), Xu et al. (2005) and Qu and Ma (2007).

6.3.1 Slug flow oscillation

When the liquid accumulates in the evaporator U-turn, a liquid/vapor interface is created and it starts moving along the channel. The accumulated liquid quickly reaches thermal equilibrium with the channel wall and the primary difference in superheat along the liquid slug is due to the pressure gradient (hydrostatic head). The local pressure is the lowest near the leading edge of the liquid slug, which corresponds to the location where nucleation is observed.

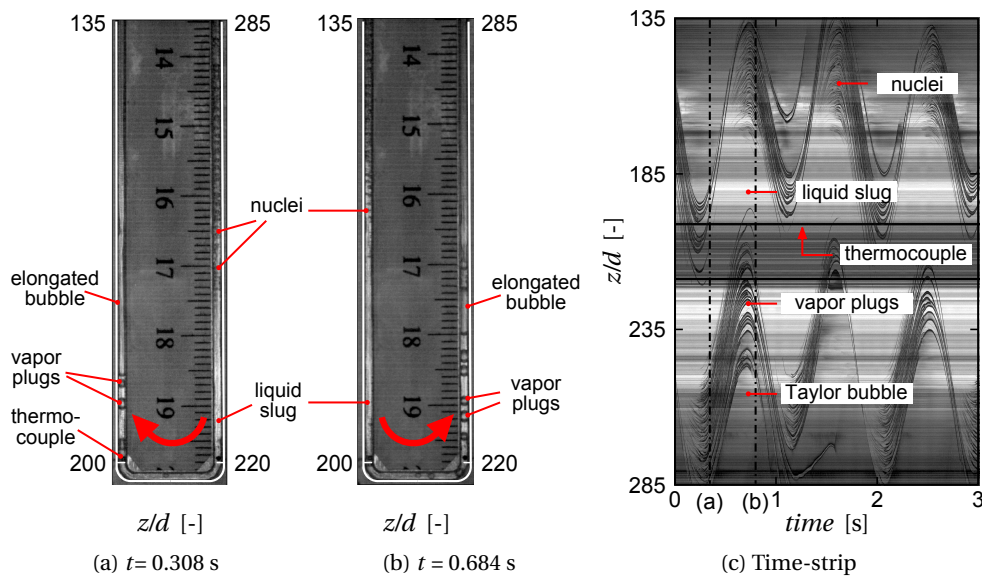


Figure 6.2: Video images of the two-phase flow distribution in the evaporator U-turn at two different times $t = 0.308$ s (a) and $t = 0.684$ s (b). Time-strip of the oscillating slug flow produced by nucleation and growth of bubbles (c). $FR = 60\%$, $\alpha = 45^\circ$, $Q_{in} = 54$ W.

The result of the combined effect of nucleation, rapid expansion and coalescence of bubbles can be observed in Figure 6.2, showing a liquid slug residing in the evaporator U-turn oscillating between the left and right channels.

Figure 6.2a shows the frame taken at $t = 0.308$ s when the evaporator left channel is mostly filled with vapor. The density difference between the two channels is such that negative momentum is reached and the liquid slug is moving back into the left channel. Vapor generation can also be observed in the top part of the moving liquid slug. The expansion of these nucleated

bubbles later produces the condition shown in Figure 6.2b, where the liquid slug is moving from the left to the right channel with positive momentum, thus reversing the flow direction. Thus the 180 degree phase difference between the nucleation taking place in the two channels and the ensuing expansion produces the oscillatory flow depicted in the time-strip of Figure 6.2c.

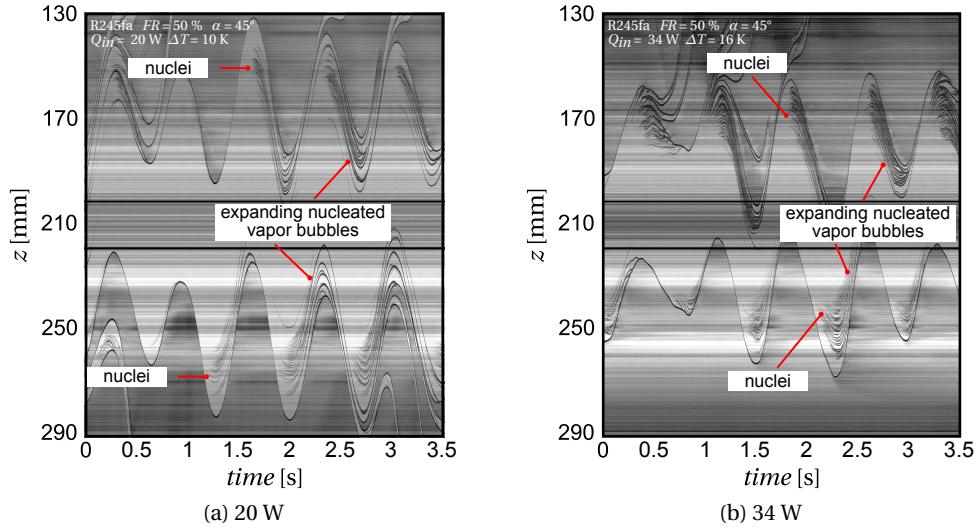


Figure 6.3: Effect of heat load on the nucleation and expansion rates for operation at $FR= 50\%$, $\alpha = 45^\circ$. (a) $Q_{in} = 20\text{ W}$ and (b) 34 W .

6.3.2 Slug flow oscillation measurements

Effect of the heat load and filling ratio

The displacement and the velocity of the liquid slug oscillating about the evaporator U-turn was graphically evaluated as described in Section 3.5.1. To assess the characteristics of the two-phase flow motion, the amplitudes and frequencies of the displacement and velocity profiles were computed as shown in Figure 6.4 and reported in Table 6.1.

In all the presented cases, the amplitude of the oscillation is seen to decrease with heat load. The transition from slug to semi-annular/annular flow is observed to be caused by the increase in nucleation intensity and evaporation rates. The bubbles which nucleate in the liquid slug residing in the evaporator expand faster and can coalesce to produce annular/semi-annular flow in the evaporator, as previously observed by Spinato et al. (2014).

At 50 % of charge with $\alpha = 45^\circ$, a significant decrease in the oscillation amplitude was observed for applied heat loads greater than 30 W, until direct transition from oscillatory to counter-clockwise circulation was observed at a heat load of 40 W (Figure 6.4). The effect of heat load on nucleation, expansion rates and bubble coalescence is shown in Figure 6.3. At 34 W heat load (Figure 6.3b), nucleated bubbles rapidly expand and coalesce with elongated bubbles whilst vapor plugs are progressively expanding while oscillating about the evaporator U-turn at lower heat loads (Figure 6.3a). The difference in oscillation amplitude can also be directly

6.3. Dynamics of the oscillatory two-phase flows

compared.

When operating at a filling ratio of 60 %, a transition from counter-clockwise circulation to oscillatory flow occurs at heat loads above 42 W. In this case, a liquid slug that accumulates in the evaporator U-turn starts to oscillate, propelled by vapor generation in the liquid. At higher heat rates, superheating conditions necessary for nucleation are reached more rapidly, thus reversing the flow direction of the liquid slug at higher frequencies. As suggested by the trend in the amplitude of the displacement signals $z(t)$ reported in Table 6.1, this flow reversal occurs before the liquid slug reaches the location $z(t)$ and thus the velocity attained at lower heat loads.

For vertical operation at a 80 % filling ratio, the same conclusions can be drawn. In this case the direct transition from oscillating slug flow to unidirectional annular flow is attained at 44 W. The liquid inventory, and thus system inertia, is very high in this case, explaining the higher oscillation amplitudes and the lower frequencies with respect to lower filling ratio cases (Table 6.1).

Table 6.1: Dynamics of the oscillating liquid slug: Effect of heat load and filling ratio

<i>FR = 50 % $\alpha = 45^\circ$</i>					
Q_{in}	T_{evap}		$z(t)$		$u(t)$
[W]	Frequency	Amplitude	Frequency	Amplitude	Amplitude
	[Hz]	[K]	[Hz]	[mm]	[mm/s]
20	1.306	0.008	1.330	15.350	115.328
22	1.386	0.007	1.284	11.454	81.297
24	1.405	0.009	1.330	14.401	108.499
26	1.411	0.009	1.398	13.676	104.752
28	1.477	0.010	1.467	12.876	100.602
30	1.411	0.011	1.421	15.691	119.947
32	1.391	0.018	1.375	10.039	73.534
34	1.452	0.017	1.401	7.811	56.860
36	1.390	0.019	1.365	7.452	51.765
38	1.346	0.024	1.330	6.084	46.429
<i>FR = 60 % $\alpha = 45^\circ$</i>					
44	1.170	0.038	1.167	19.62	157.441
50	1.190	0.040	1.192	19.132	126.789
54	1.215	0.045	1.200	19.031	118.781
<i>FR = 80 % $\alpha = 0^\circ$</i>					
24	0.494	0.018	0.458	36.817	94.803
26	0.489	0.019	0.514	34.280	95.405
30	0.489	0.022	0.514	33.278	94.105
34	0.479	0.024	0.514	31.109	86.000
38	0.484	0.030	0.473	30.117	82.620

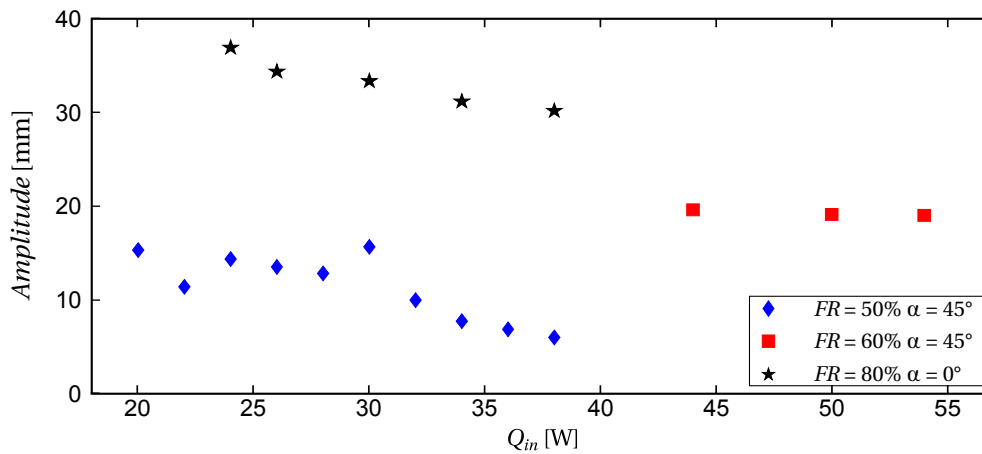


Figure 6.4: Amplitudes of oscillation of a liquid slug in the evaporator U-turn as computed from the time-strip for different operating conditions.

In the oscillatory flow regime, it is frequent to observe in the evaporator time-strips, especially at high heat loads, non-periodic patterns with many frequency components. As shown in Figure 6.5, nucleation and expansion rates can vary with time producing non-constant oscillation amplitudes and frequencies. As a result of this, the corresponding frequency spectra display numerous components highlighting the non-periodic nature of the dynamics. This is evident from Figure 6.5 that reports the frequency spectra of the evaporator temperature T_{evap} and displacement profile $z(t)$ relative to operation at $FR = 50\%$, $\alpha = 45^\circ$, $Q_{in} = 38$ W (Figure 6.5a) and at $FR = 60\%$, $\alpha = 45^\circ$, $Q_{in} = 54$ W (Figure 6.5b). In the first case, a low frequency component of 0.33 Hz is present in both the thermal behavior and flow dynamics. The repetition of this 3 s period pattern is also visible in the relative time-strip.

The periodic oscillation of the liquid slug can be observed in the time-strip of Figure 6.5b. Peak values in the displacement curve $z(t)$ are attained at $t = 1.5$ s and 4.5 s and correspond to the maximum expansion rates of the second and sixth coalescing bubbles residing in the right channel (bottom of the time-strip). The peak in the velocity profile (Figure 3.11c) always occurs after reaching the local minimum velocity value. The flow momentarily slows down, achieving higher evaporation rates, and thus later producing a stronger propelling force and higher flow velocity in the following expansion.

6.3. Dynamics of the oscillatory two-phase flows

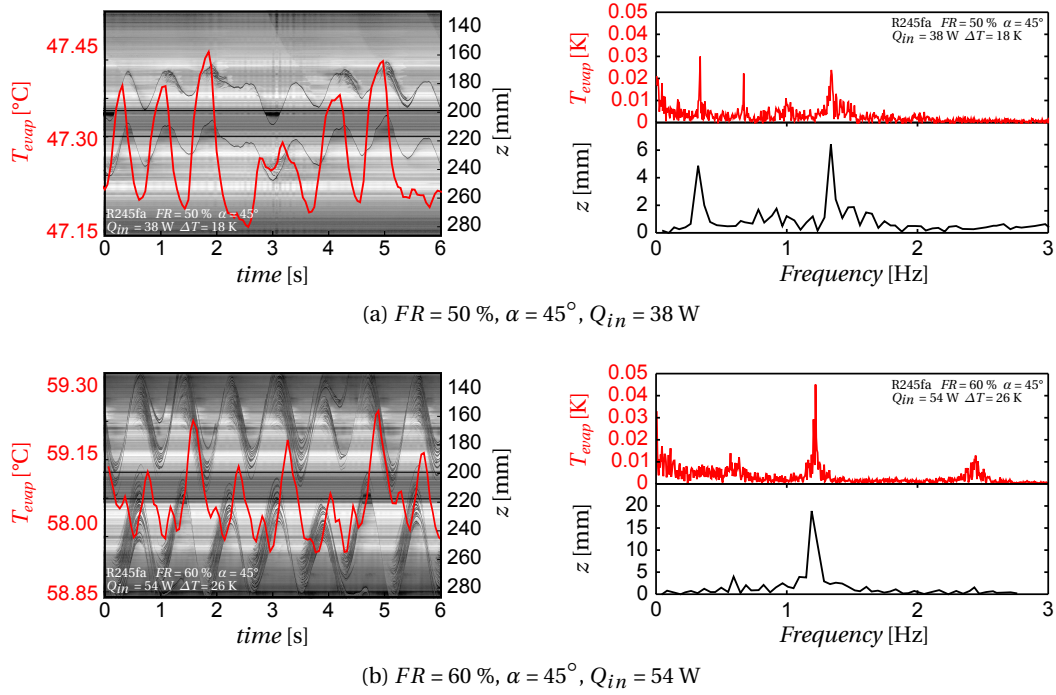


Figure 6.5: Time-strips with superimposed synchronized evaporator temperature profile and relative frequency spectra for operation at $FR = 50\%$, $\alpha = 45^\circ$, $Q_{in} = 38\text{ W}$ (a) and $FR = 60\%$, $\alpha = 45^\circ$, $Q_{in} = 54\text{ W}$ (b)

Effect of system orientation

The amplitudes and frequencies of the liquid-slug oscillation were computed for system operating at a 60 % of charge at different inclinations α . The results for 30 and 40 W heat input are reported in Figure 6.6. A significant reduction of the mean oscillation amplitude is observed for angles higher than 60° . When the system is positioned horizontally, nucleation followed by bubble expansion is not observed and the interface motion completely stops.

Proof of the effect of gravity on the operation of the single-turn CLPHP is obtained from analysis of the dominant frequencies of thermal (Figure 5.4b) and displacement data (Figure 6.6b) for different operating inclinations. As reported in Table 6.2 and highlighted in Figure 6.6b, the dominant frequencies decrease with the cosine of the inclination angle α and thus with the actual value of the gravity acceleration $g_z(\alpha)$ which is given as:

$$g_z(\alpha) = |\vec{g}| \cdot \cos(\alpha) = g_{VED} \cdot \cos(\alpha) \Rightarrow \frac{g_z(\alpha)}{g_{VED}} = \cos(\alpha) \quad (6.3)$$

A similar cosine-like attenuation of the oscillation amplitude with increasing inclination can also be seen.

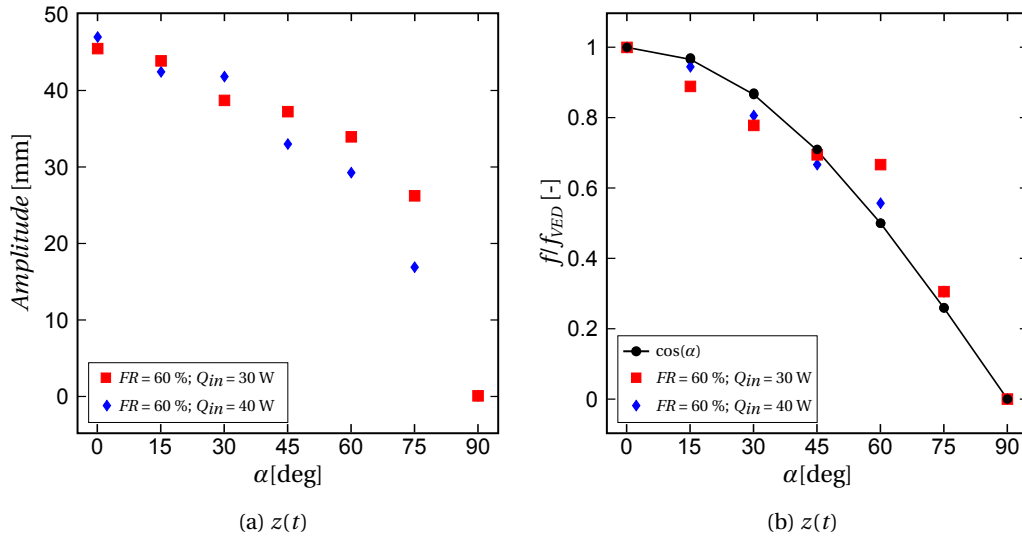


Figure 6.6: (a) Amplitudes of oscillation of the liquid slug in the evaporator U-turn for different inclination angles α . (b) Dominant oscillations frequencies normalized with respect to vertical orientation (VED) value f/f_{VED} for different angles α . $FR = 60\%$, $Q_{in} = 30$ and 40 W .

Table 6.2: Dynamics of the oscillating liquid slug: Effect of inclination angle

$FR = 60\% Q_{in} = 30\text{ W}$					
α [deg]	$\cos(\alpha)$ [-]	T_{evap}		$z(t)$	
		Frequency [Hz]	Amplitude [K]	Frequency [Hz]	Amplitude [mm]
0	1.000	1.734	0.017	1.650	46.77
15	0.966	1.643	0.015	1.559	42.23
30	0.866	1.406	0.016	1.330	41.61
45	0.707	1.286	0.012	1.100	32.82
60	0.500	0.887	0.011	0.919	29.09
75	0.259	0.434	0.011	0.504	16.77
90	0.000	0.000	0.000	0.000	0.000
$FR = 60\% Q_{in} = 40\text{ W}$					
0	1.000	1.719	0.021	1.650	45.26
15	0.966	1.638	0.023	1.467	43.66
30	0.866	1.527	0.029	1.284	38.51
45	0.707	1.132	0.028	1.146	37.04
60	0.500	0.770	0.024	1.100	33.76
75	0.259	0.403	0.024	0.504	26.07
90	0.000	0.000	0.000	0.000	0.000

6.4 Dynamics of circulating flow and flow reversals

Circulating flow in a PHP is characterized by flow reversals and local flow direction switching. In order to describe the physics of PHPs, and thus produce accurate mechanistic models, it is important to identify the mechanisms characterizing the two-phase flow behavior that potentially produce flow pattern transitions. Unidirectional flow is attained when the vapor-liquid distribution in the PHP loop is such that the equilibrium condition of Eq. 6.1 is satisfied. However, nucleation and the ensuing expansion of bubbles in precise locations in the loop, can produce the impulse necessary for flow reversals and the local flow direction switch.

6.4.1 Flow reversals

From the analysis of the high frequency temperature data and the flow pattern transition trends, it is evident that the occurrence of flow reversals is affected by the heat load and filling ratio.

Experimental results suggest that, when increasing the heat load past a certain value, annular/semi-annular flow is attained. The two-phase flow then starts to circulate around the loop but flow reversals can still occur and oscillating flow regime can be temporarily restored. During this particular flow regime, attained at medium-high heat loads, the pressure in the system is such that two-phase flow instabilities (nucleation, bubble breakage, coalescence,..) produce the local change in the void fraction necessary to reverse the flow direction.

The system becomes stiffer with increasing heat load and thus operating temperature and pressure, as previously described in Section 5.4.1. Therefore, higher impulses are now necessary to divert the system from the equilibrium condition of Eq. 6.1 and to permanently change the circulation direction. The latter can still be locally changed by local nucleation and the expansion of bubbles in the evaporator inlet. This phenomenon, known as 'local flow direction switch', was observed by Xu et al. (2005) and it is said to add an oscillatory component to the unidirectional flow (Section 6.4.3).

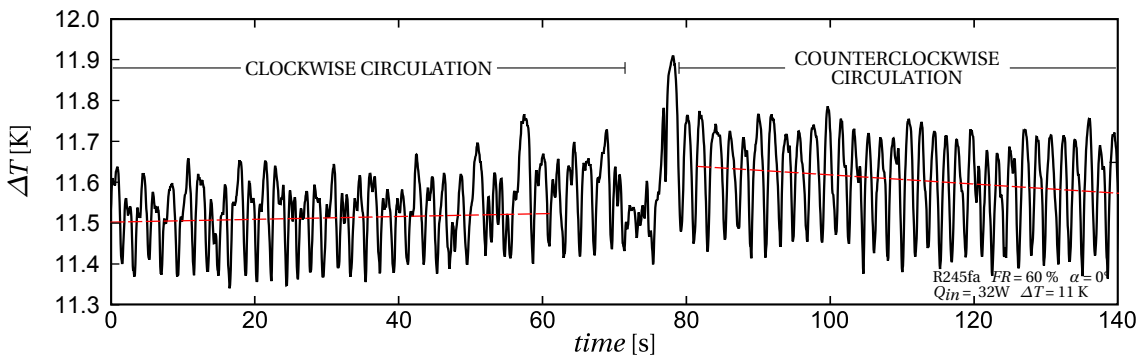
The filling ratio and thus the compressible volume, has an effect on the system pressure and stiffness (Section 5.4.1). Higher heat inputs are seen to be necessary for unidirectional circulation when operating with a higher compressible volume as for low filling ratios ($FR < 50\%$). Moreover, no flow reversals are observed (Section 4.3) and the system transitions from oscillating to circulating regime at high filling ratios of 80 and 90 %, with increasing heat loads.

6.4.2 Thermal measurements of the flow reversals

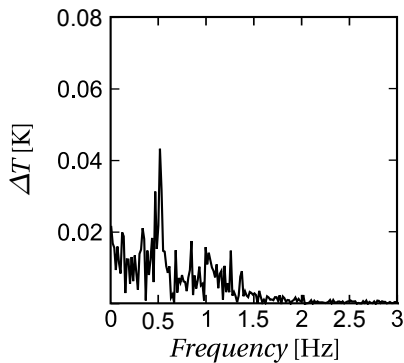
During vertical operation of the system at 32 W and 60 % filling ratio, the flow direction reversed from *clockwise* to *counter-clockwise*. The high frequency temperature measurements suggest different thermal behavior in the two directions, as indicated by the temperature difference ΔT ($T_{evap} - T_{cond}$) plotted in Figure 6.7a versus time. The frequency spectra of the temperature data computed for the clockwise (Figure 6.7b) and counter-clockwise (Figure 6.7c) flow circulation indicate lower oscillation amplitude and frequency for the clockwise case. In other words, a higher frictional component along this direction is thought to be

responsible for the higher total frictional losses, thus lower kinetic energy and average flow velocity. Moreover, as indicated by the trend lines in Figure 6.7a, the mean temperature difference starts to decrease after the counter-clockwise circulation is established. A lower pressure difference is required for the self-sustained flow motion and the hypothesis of lower frictional component along this flow direction is thus confirmed.

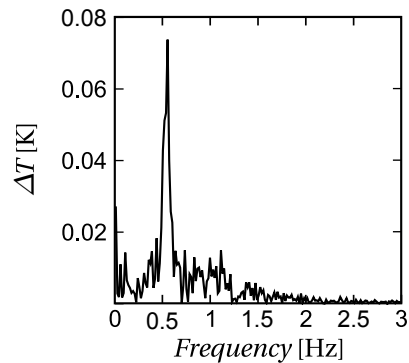
During this experimental study, the preferred flow direction is counter-clockwise. This peculiarity is thought to be consequence of the anisotropy of the channel surface structure due to the machining process. The local shear stress between the channel and the two-phase flow changes with flow direction and the system would then 'naturally' tend to circulate along the lower energy direction.



(a) Total temperature oscillation ΔT



(b) Clockwise circulation



(c) Counterclockwise circulation

Figure 6.7: (a) Temperature difference ΔT between evaporator and condenser during flow reversal and temperature difference frequency spectra for (b) clockwise and (c) counter-clockwise flow circulation when operating at $FR = 60\%$, $\alpha = 0^\circ$, $Q_{in} = 32\text{ W}$

6.4.3 Local flow direction switch

The phenomenon known as 'local flow direction switch' (Xu et al., 2005) is thought to be caused by bubble nucleation that triggers quick vapor generation at the evaporator inlet. This then produces a temporary change of the momentum in the loop, as stated by Eq. 6.2.

Figure 6.8 reports the time-strips for counter-clockwise circulating flow in the condenser U-turn (top to bottom in the time-strip of Figure 6.8a) and in the evaporator inlet (Figure 6.8b) for operation at 54 W and 60 % filling ratio. In the evaporator inlet, the flow regularly ($t = 1$ s, 3 s, 5 s) but momentarily moves opposite to the main flow (upwards in the time-strip) under the force of nucleated bubbles which are expanding downstream. Simultaneously, in the condenser, after each appearance of annular flow, the flow quickly slows down and briefly changes direction. As a result, the two-phase flow experiences oscillating trajectories, as depicted in Figure 6.8a. This local change in the flow's main direction adds a low amplitude oscillating component to the circulating flow, whose resulting trajectory is then quasi-sinusoidal.

In the single-turn CLPHP, this direction switch propagates along the whole loop and periodically interrupts the liquid return to the evaporator. The time-strip of Figure 4.1d now depicts the liquid film locally thinning and drying out due to evaporation, thus causing an increase in the wall temperature. This periodic drying of the evaporator wall diminishes the evaporative heat transfer and thus the propulsive force in the loop, which is then restored when the evaporator is again rewetted.

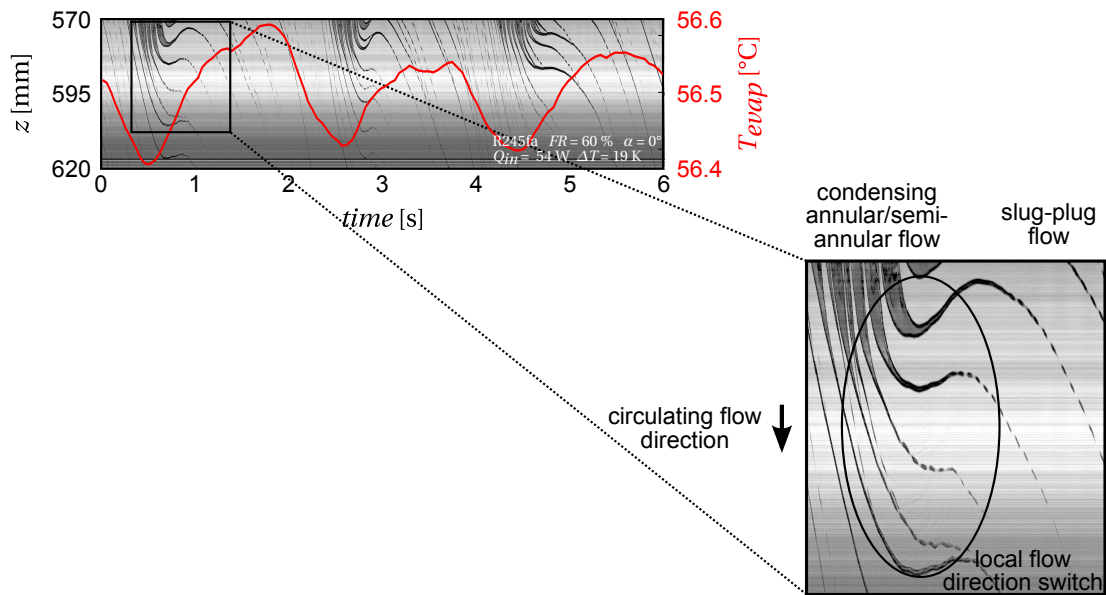
The synchronized evaporator temperature profiles T_{evap} on the time-strips of Figure 6.8 show that the peak momentum in the loop, when annular flow exists at the top of the condenser left channel, is reached after evaporator rewetting (minimum evaporator temperature). Periodic variation in evaporation rates, and thus liquid/vapor distribution in the loop, are then thought to be responsible for the momentarily slowed down circulation and thus for the local flow direction switch.

The duration of local flow direction switch is similar to one half period of the oscillatory regime of the same loop, as indicated by the temperature and time-strip data in Figure 4.1d and 4.2d.

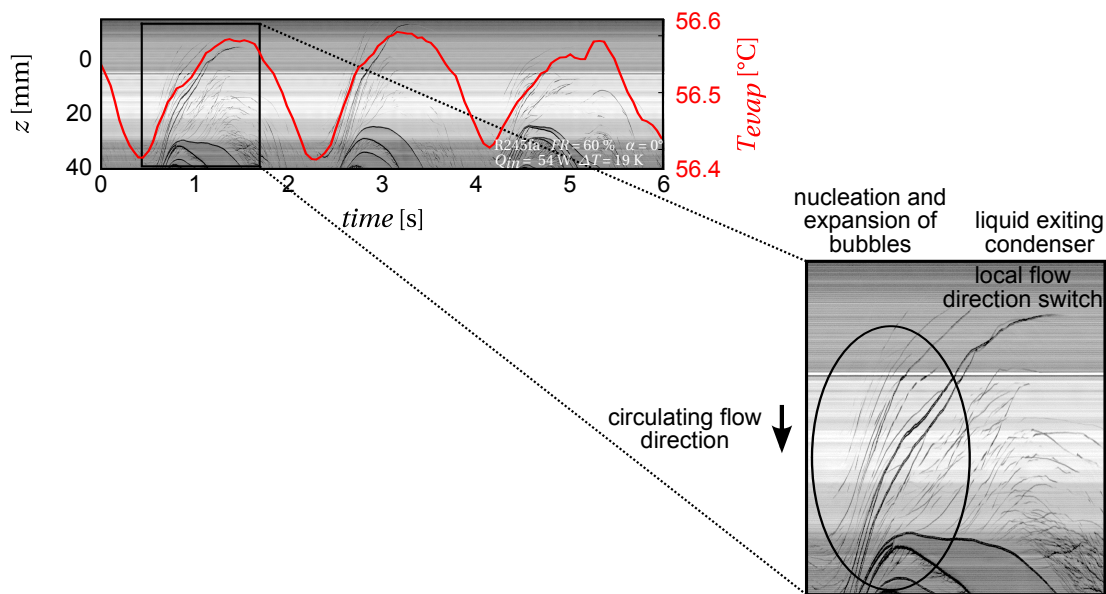
Effect of heat load and filling ratio on local flow direction switch

Thermal and visual investigations of the circulating flows indicate that the effect of the local flow direction switch diminishes with increasing heat input (Section 4.4.1). The mean amplitude of the oscillatory flow component in the condenser, and the mean velocity \bar{u} of rising bubbles in the evaporator inlet can be considered as metrics to evaluate the effect of the local flow direction switch. These two quantities were graphically extracted from the time-strips as explained in Section 3.5.1.

The results relative to vertical operation at a 60 % of charge are reported in Figure 6.9. Consistently with the frequency spectrum of Figure 4.4a, a trend in both amplitude and mean velocity cannot not be established at heat inputs lower than 50 W. Under these conditions the nature of the flow in CLPHP is such that it still varies considerably with time. Above an applied heat load of 50 W, both oscillation amplitude and mean velocity \bar{u} drop with increasing heat load. Confirming previous observations, at such heat loads, the system is stiffer and compression and expansion rates of vapor plugs are significantly reduced.



(a)



(b)

Figure 6.8: Time-strips for counter-clockwise circulating flow in the condenser with superimposed evaporator temperature T_{evap} (a) and entering the evaporator (b). $FR = 60\%$, $\alpha = 0^\circ$, $Q_{in} = 54\text{ W}$

6.4. Dynamics of circulating flow and flow reversals

Consistent with the observation reported in Section 6.4.1, at high filling ratios the occurrence of flow reversals and the effect of the local flow direction switch is expected to be lower than for lower filling ratios at the same heat input. The frequency spectra of the evaporator and condenser temperatures for operation at $FR = 70\%$ are reported in Figure 6.10a and 6.10b. No high frequency component relative to local direction switch can be observed for heat loads higher than 48 W, while the same is still present in the spectra of Figure 5.7a and 5.7b for operation at $FR = 60\%$.

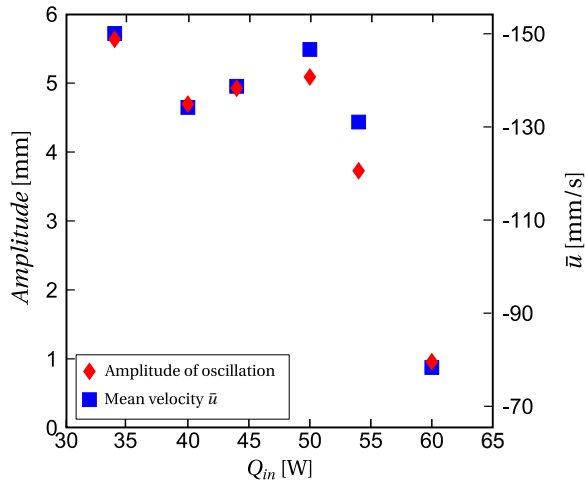


Figure 6.9: Mean amplitude of the oscillatory flow component in the condenser (red) and mean velocity of rising bubbles in the evaporator inlet \bar{u} (blue), graphically evaluated from the time-strips relative to operation at $FR = 60\%$, $\alpha = 0^\circ$

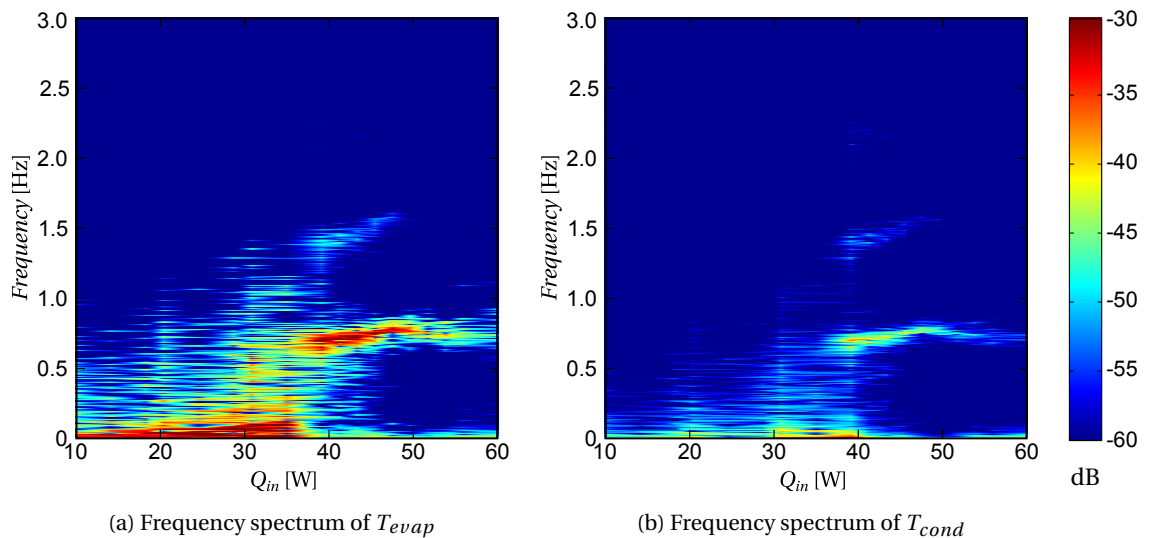


Figure 6.10: Frequency spectra of evaporator temperature T_{evap} (a) and of condenser temperature T_{cond} (b) for operation at $FR = 70\%$, $\alpha = 0^\circ$

6.4.4 Bubble velocities in the condenser

According to Xu et al. (2005), the major parameters affecting the velocity of a bubble are bubble size, buoyancy force and system pressure gradient. From analysis of the time-strips obtained for circulating flow, it is observed that dispersed bubbles have larger velocities than Taylor bubbles in upward flows. The repeating pattern of small bubbles coalescing with Taylor bubbles while sweeping up the condenser channel can also be seen in Figure 6.8a. Dispersed bubbles are in fact pushed upwards by buoyancy forces whilst rising Taylor bubbles are slowed down by wall friction.

Velocity of dispersed rising bubbles

The average velocity \bar{u} of the dispersed bubble rising in the condenser was graphically computed as described in Section 3.5.1. Particular care was taken to choose bubbles with similar diameters. For each operating condition, an appropriate sample size (number of bubbles) was decided based on statistical analysis. The results of this analysis are reported in Figure 6.11 for different operating conditions.

The effect of the pressure gradient is evident in Figures 6.11a and 6.11b. The total pressure gradient is known to increase with filling ratio and thus increase the average velocity \bar{u} for the same heat load. The standard deviation of the values computed at heat loads lower than 54 W for inclined operation at $FR = 40\%$ might justify the deviation from the expected behavior. The role of gravity on the dynamics of dispersed bubbles is suggested by the slight decrease in average velocities with increasing heat input and system temperature. The density difference between liquid and gas phase, and thus the buoyancy force pushing dispersed bubbles upwards towards the condenser U-turn, in fact decreases with temperature. Moreover, for the same filling ratio and heat loads, the average velocities relative to inclined operation are lower than those computed for the same conditions at vertical operation.

As shown in Figure 4.4b, the dominant frequency component for vertical operation at 60 % of charge reaches a local maximum at Q_{in} of 38 W, suggesting higher system stiffness and flow velocities. The average velocities \bar{u} of Figure 6.11a reach a maximum at the same value of heat load. Similarly, the effect of the local flow switch slightly decreases (Figure 6.9) for the same heat input. Thermal and flow dynamics data follow the same trends and thus confirm the strong coupling of thermal and flow-dynamics in the behavior on such systems.

6.4. Dynamics of circulating flow and flow reversals

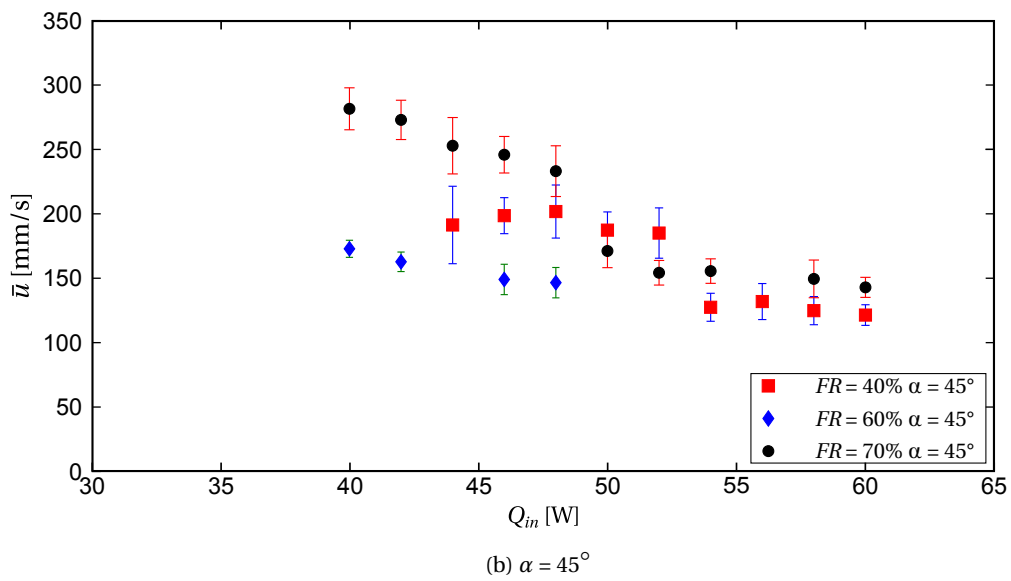
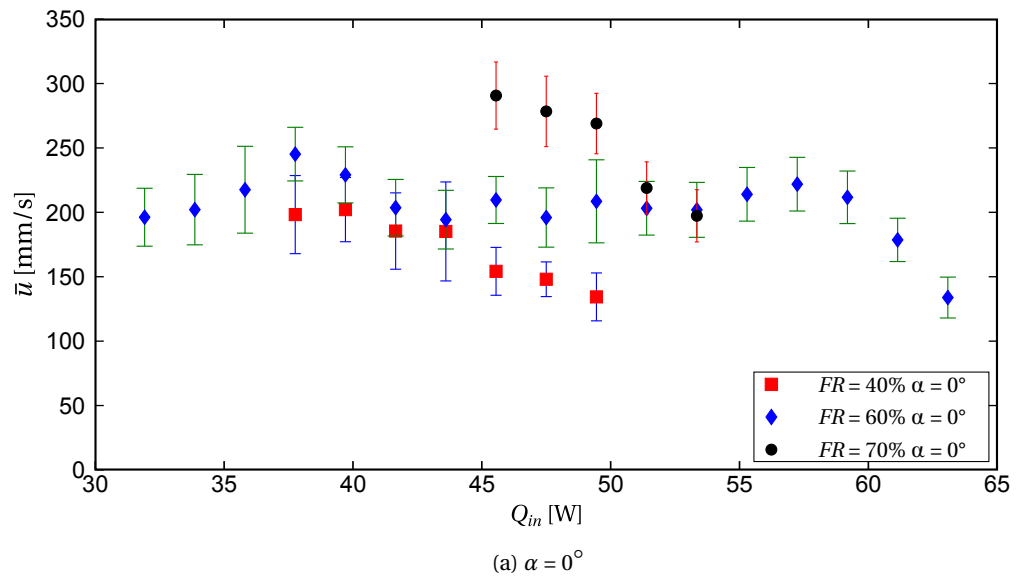


Figure 6.11: Average velocity \bar{u} of small (dispersed) bubbles rising the condenser up to the U-turn in circulating flow. (a) Vertical operation ($\alpha = 0^\circ$) and (b) inclined operation ($\alpha = 45^\circ$)

Velocity of Taylor bubbles

The local velocity of Taylor bubbles is seen to vary with time for all the analyzed conditions. This variation can be caused by the local direction switch, and changes of the Taylor bubble lengths due to evaporation and condensation. The latter results in a change in the shear force acting on the Taylor bubbles and thus their velocities.

The velocity profile $u(t)$ was computed for Taylor bubbles during circulating flow regime. Figure 6.12 reports velocity data and time-strips for vertical (VED) operation at a 60 % of charge for different heat loads. It can be seen that velocities reach nearly 0.8 m/s and the dynamics of the Taylor bubbles exhibits the effect of the local direction switch.

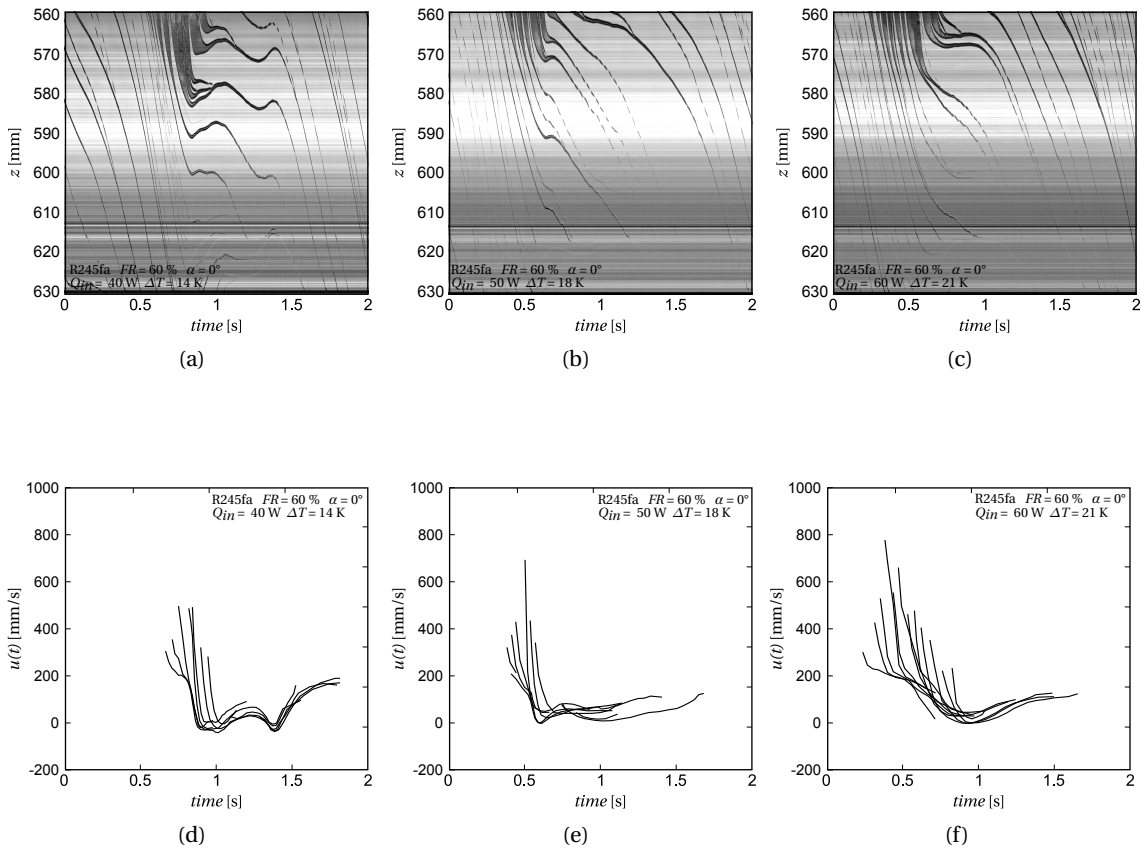


Figure 6.12: Velocity $u(t)$ of Taylor bubbles rising the condenser up to the U-turn in circulating flow. Time-strips (a)-(c) and relative velocity profile $u(t)$ (d)-(f) for CLPHP operating vertically at 60 % of charge under 40, 50 and 60 W heat input.

6.5 Gravity and flow pattern transition

By considering the mechanisms producing oscillating flow (Section 6.3), flow reversals (Section 6.4) and local flow direction switch (Section 6.4.3), with observations of the flow pattern transitions, confirmation of the role of gravity on the operation of the single loop CLPHP, as stated by Khandekar and Groll (2004), can be found.

The hypothesis that (a) the only axial forces acting on the fluid are *net gravity* and *shear stress*, and that (b) gravity supplies the impulse necessary for flow reversal are confirmed by the following insights:

1. When liquid accumulates in the evaporator U-turn, nucleation takes place in the two channels with a 180 degree phase shift, and the ensuing expansion of bubbles produces oscillatory flow.
2. Flow reversals are less frequent at high heat loads and finally stop at the critical heat load for transition to circulating flow. Local flow direction switch, on the contrary, is seen to occur for all heat loads but its effect fades with increasing heat input. At high system energies, the system is in fact stiffer thus requiring higher impulses to be diverted from the equilibrium condition.
3. At higher filling ratios, higher system energies are necessary to obtain unidirectional circulation. The difference between the mass in the descending and rising tubes is such that a small change in void fraction in one of the tubes produces the condition of Eq. 6.2. At filling ratios of 80 and 90 % the system directly moves from oscillating flow to unidirectional circulation.
4. *Counter-clockwise* circulation is preferred due to a possible lower frictional component produced by the channel surface structure.

6.6 Conclusions

Novel information on the two-phase flow dynamics are provided by synchronized thermal and visual investigation on a single loop CLPHP. The role of gravity on the system operation is assessed through the analysis of the net forces acting on the system. The mechanisms producing oscillatory and circulating flow and of their transition trends with heat load and filling ratio is here described, providing further evidence of the hypothesis that thermal induced forces produce the impulse necessary to produce and sustain flow motion in the single-turn CLPHP.

7 Conclusions and Recommendations

In the present study, an experimental investigation of the thermal and flow-dynamical behavior of a single-turn CLPHP was performed. High frequency temperature measurements and high-speed videos of the two-phase flow in the system channels were simultaneously recorded, for various operating conditions. New image-processing techniques were developed and applied to the videos in order to obtain qualitative and quantitative data about the flow dynamics which were then coupled with the thermal data. This provided novel details regarding the self-sustained two-phase flow in the single loop CLPHP. In particular the study achieved the following goals:

- A novel inspection of the two-phase flow patterns, through visual observations in the evaporator and condenser section of the device, was implemented. This focused on (a) identifying and classifying the main flow patterns observed, and (b) assessing their transition trends for different filling ratios and heat inputs. Flow pattern maps were built for vertical and inclined operation.
- The overall thermal resistance of the system was measured and correlated with the flow pattern results. Operation maps, composed of flow pattern and thermal resistance maps, were derived for vertical and inclined operation. The relationship between flow pattern and thermal performance was then qualitatively assessed.
- The thermal performance of the system was further investigated through the analysis of the high frequency temperature measurements, thus gaining a deeper understanding of the relationship between the flow pattern and the thermal behavior of the system. An investigation into the use of frequency data as a means to analyze the thermo-flow dynamics of the system was also carried out, by coupling thermal and flow-dynamic data with flow pattern and system performance.
- Local time-averaged heat transfer coefficients were predicted by developing a state-of-the-art *mechanistic* model for the evaporation of elongated bubbles in the CLPHP microchannels. The obtained local and averaged results were then used to qualitatively

assess and account for the heat transfer characteristics in the CLPHP evaporator U-turn for different flow patterns.

- The novel inspection technique developed here was used to obtain quantitative data about the two-phase flow-dynamics in order to substantiate theories related to system operation and performance. The net forces acting on the system could then be identified, thus revealing new details on the mechanisms producing slug-oscillation, flow circulation, flow reversals, and 'local flow direction switch' in the single loop CLPHP.
- Dedicated studies were carried out in order to identify the role of system inclination on its operation and performance, thus clarifying the role of gravity.

7.1 Main findings of the present study

Flow patterns: A time-strip image processing technique was applied to the high-speed videos recording the two-phase flow in the evaporator and condenser sections of the CLPHP at various operating conditions. Four distinct flow regimes were observed when varying *heat input*, *filling ratio*, and *orientation*, but universally defined transition boundaries could not be defined. Unidirectional circulating flow was attained at high heat loads with only a few cases where the system reverted to oscillating flow with increasing heat loads. The effect of filling ratio, and thus mass of the system, was observed at very high filling ratios where a direct transition from the oscillating regime to unidirectional circulation was observed. Finally, the orientation also played a role in the transition to unidirectional circulating flow. For vertical operation the critical heat load for transition to unidirectional circulation increased with filling ratio, whilst a trend for this transition could not be established for inclined operation.

Thermal performance: The coupled analysis of the measured thermal resistance with the flow pattern, here reported in the form of *operational maps*, confirmed the effect of the two-phase flow pattern on the system performance. Consistent with previous results, annular/semi-annular flow, developing in the evaporator during circulating flow, produced a significant improvement of the thermal performances. Low thermal resistances were in fact measured at high heat loads and low filling ratios. Low liquid inventory could yield lower thermal resistances but with the risk of evaporator dry-out. The latter reduced the 'pumping power' and the system thermal performance, as confirmed by the spectral data of the temperature oscillations. High liquid inventory, on the contrary, could produce slug-flow, thus increasing the rate of sensible heat transfer with respect to the other heat transfer modes. The predicted time-averaged heat transfer coefficients qualitatively confirmed the lower rates of sensible heat exchanged after transition to circulating annular/semi-annular flows.

Thermo-flow dynamics: The developed synchronized thermal and visual technique allowed investigation of the thermal and hydrodynamic behaviors of the single loop CLPHP by means of spectral analysis. The thermal behavior reported in the frequency spectra of the evaporator and condenser temperatures was coupled with the frequency spectra computed

for the intensity of the time-strip at the same locations, thus revealing a profound correlation between the two-phase flow pattern, the two-phase flow-dynamics and the thermal characteristics of the system during operation. Each flow pattern showed a characteristic frequency spectrum, which was present in the temperature data, in the intensity profile of the time-strip, and in the two-phase flow motion.

The displacement and the velocity of the liquid slug oscillating about the evaporator U-turn was graphically evaluated, and new insights on the transition to annular/semi-annular flow were gained. The latter was observed to be caused by the increase in nucleation intensity and evaporation rates with heat load, which in turn reduced the oscillation amplitudes of the liquid slug. The average velocity of the dispersed bubbles rising in the condenser during circulating flow was also graphically evaluated, confirming the effect of filling ratio, heat load and inclination on their dynamics.

Force balance during operation of the single loop CLPHP: The only (axial) forces acting on the fluid were observed to be *net gravity* and *frictional shear forces*. To obtain counter-clockwise flow motion in the loop, the average density in the left (*descending*) channel must be higher than the one in the right (*rising*) channel. In order to reverse the flow direction, this situation must be reversed by redistribution of the liquid-vapor in the device by events such as local nucleation in the left channel.

Experimental results suggested that, at low-medium heat fluxes, the oscillation of a liquid slug in the evaporator U-turn was produced by a 180 degree phase difference between the nucleation taking place in the two channels. At higher heat loads eventually, annular/semi-annular flow was attained and the two-phase flow started to circulate but flow reversals could still occur. This was due to the pressure in the system, such that two-phase flow instabilities could produce the local change in the void fraction necessary to reverse the flow direction. Increasing the heat load further, thus increasing the operating pressure, the system became stiffer and higher impulses were necessary to divert the system from its equilibrium condition and to permanently change the circulation direction. The latter could, in these conditions, be only locally changed, as happened for the 'local flow direction switch'.

The effect of filling ratio, and thus the compressible volume, was also observed to play a role in the flow pattern transition. Higher critical heat inputs were necessary to achieve unidirectional circulation when operating at low filling ratios. Moreover, no flow reversals were observed and the system naturally transitioned from oscillating to circulating regime as the heat input was increased for high filling ratios.

Role of gravity: Thermal and visual investigation carried out on the PHP when changing its orientation with respect to the vertical suggested a strong effect of the inclination angle on the system operation. The hypothesis of thermally induced forces producing two-phase oscillating flow was confirmed by the steep increase in the thermal resistance with increasing inclination angle (i.e. closer to the horizontal position), together with the diminishing gap of performance between vertical and near-horizontal operation with increasing heating power.

Moreover, the dominant oscillation frequencies measured for both thermal and displacement data were seen to decrease with the cosine of the inclination angle, thus with the value of the gravity force acting on the system. No flow motion was observed for the system when positioned horizontally.

7.2 Recommendations for future research

Within the scope of this study, novel information about the two-phase flow phenomena occurring during the operation of a single loop CLPHP was gathered. In particular, the experimental technique here implemented proved to be a very powerful tool for the coupled analysis of thermal and flow behavior in PHPs. However, the study highlighted new aspects that would require additional research to be done and these are presented below:

The approach proposed during this study could be applied to investigate the operation of a system with different characteristics, such as *multi-turn* PHPs. Data on the bubble dynamics and on the mechanisms producing self-sustained two-phase oscillating or circulating flows could be gathered, providing new insights on the motive force producing two-phase flow motion. The role of gravity, for instance, which is still largely debated in the literature, could be investigated when varying the channel geometry and the number of turns.

Moreover, applying the holistic approach which is nowadays successfully used in the assessment of microchannel flow boiling, a large database containing flow pattern data, frequency content of thermal and flow-dynamics, together with the two-phase flow velocities would help in the implementation of a comprehensive mechanistic model, to predict the performances of pulsating heat pipe coolers. In order to verify these models, flow visualization studies would provide quantitative data of the initial and equilibrium film thicknesses, required for the verification of the hypothesis of inertially dominated film laying, which is particularly relevant in the solution of the evaporation/condensation mechanisms occurring at the thin film liquid-vapor interface. The validation of the model would then be done primarily by comparing the results of the numerical simulation with frequency data obtained from the experimental studies. An experimental estimation of the heat transfer coefficients, attained by coupling temperature and pressure data of the working fluid with thermal maps of the surface under investigation, will provide new data regarding the relative contribution of sensible and latent heat in the overall heat and mass transfer during PHP operation.

A Uncertainty analysis

The estimation of the uncertainties of the experimental results adopted in this work refers to Kline and McClintock (1953) approach. The *uncertainty* of a measurement is the possible error that a value might have, thus the interval within which the true value is expected to lie. If we consider a variable x_i its uncertainty, represented as δX_i , is usually calculated as the norm of the bias or systematic error (B_i) and the precision or random error (P_i). In presence of n independent variables x_i , the effect of the uncertainty of a single variable on the quantity F is the partial derivative of F with respect to that single variable, multiplied by the uncertainty of that variable:

$$\delta F_{x_i} = \frac{\partial F}{\partial x_i} \delta x_i \quad (\text{A.1})$$

The maximum uncertainty of F is computed as the Euclidean norm of the individual uncertainties:

$$\delta F = \left(\sum_{i=1}^n \left(\frac{\partial F}{\partial x_i} \delta x_i \right)^2 \right)^{\frac{1}{2}} \quad (\text{A.2})$$

Equation A.2 can be applied only when the distribution of errors or uncertainties is Gaussian for all the independent variables x_i and these are provided at the same confidence level (2σ).

A.1 Uncertainty measurement

Table A.1 lists the experimental error for each type pf measurement, determined through calibration of the instrument or reported in the specifications.

Table A.1: Measurement errors of instrumentation

Quantity	Measurement error
Water side thermocouple	±0.1 K
Flow rate	±15 %
Test section thermocouple	±0.1 K
Voltage	±0.05 %
Current	±0.9 %
Absolute pressure	±1000 kPa f.s.
Filling Ratio	±5 %

Figures A.1a and A.1b show the calibration curves for one the thermocouples and the pressure sensor respectively. The equations applied for the correction of instrument raw signal S are also indicated.

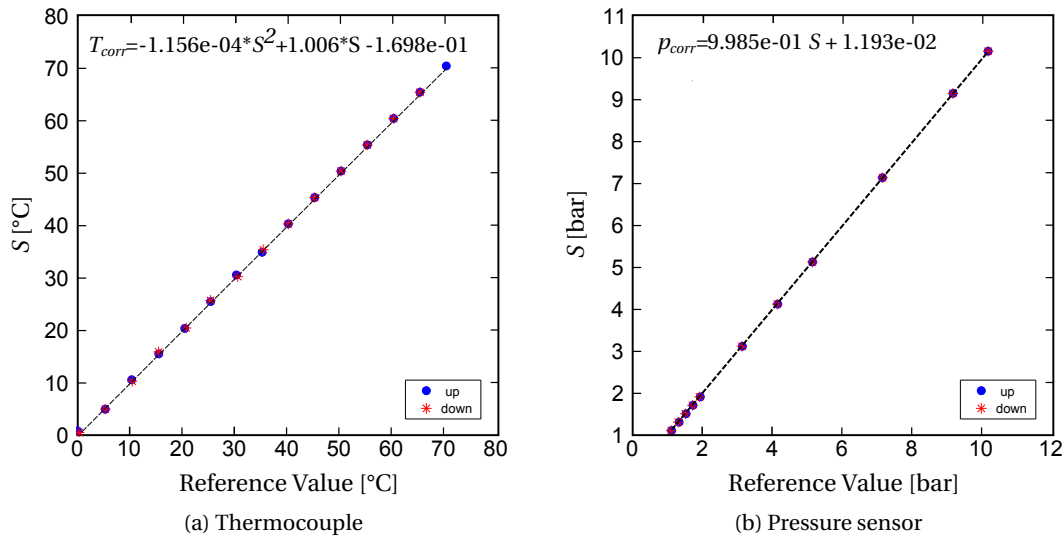


Figure A.1: Calibration curves for thermocouples (a) and pressure sensor (b).

A.2. Uncertainty propagation

The precision of each thermocouple was known to be the twice standard deviation from the steady-state value it measures repeatedly. Measurements under isothermal conditions, over a period of three minutes, were taken for temperatures within the system operating range. Figure A.2 shows the repeatability of the test-section thermocouples measurements at 23.5 °C.

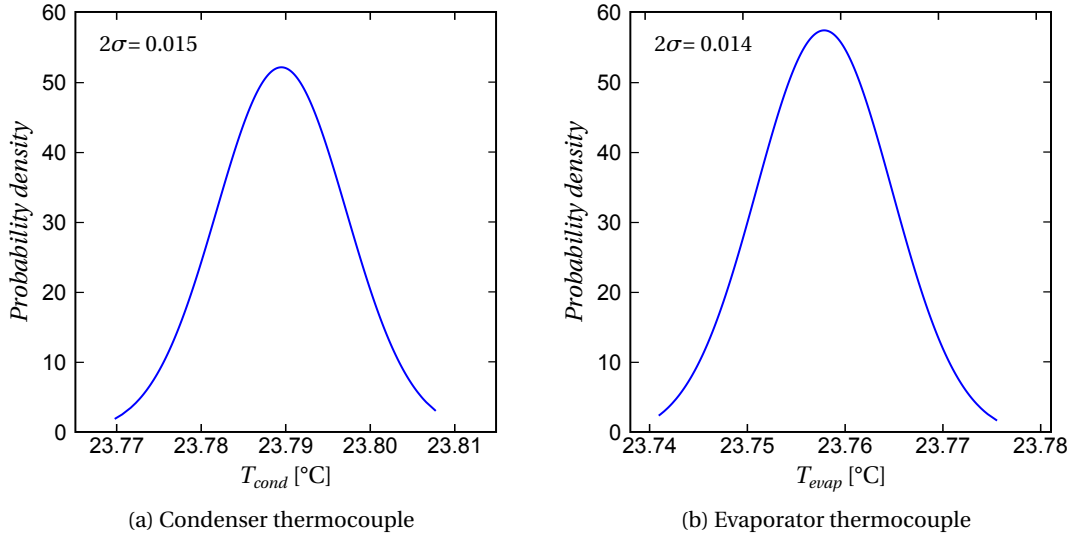


Figure A.2: Temperature measurements under isothermal conditions at 23.5 °C for the condenser (a) and evaporator (b) thermocouples.

A.2 Uncertainty propagation

A.2.1 Electrical Power

The electrical input power P_{el} uncertainty was calculated as:

$$\delta P_{el} = \left((V\delta I)^2 + (I\delta V)^2 \right)^{\frac{1}{2}} \quad (\text{A.3})$$

A.2.2 Heat Load water side

The heat load of the water side was measured in the primary water circuit as:

$$Q_{out} = \dot{m}_1 c_p \Delta T \quad (\text{A.4})$$

The resulting uncertainty was computed according to Eq. A.5, assuming an uncertainty of 0.1 % for the c_p of water.

$$\delta Q_{out} = \left(\left(\frac{\partial Q_{out}}{\partial \dot{m}} \delta \dot{m} \right)^2 + \left(\frac{\partial Q_{out}}{\partial c_p} \delta c_p \right)^2 + \left(\frac{\partial Q_{out}}{\partial \Delta T} \delta \Delta T \right)^2 \right)^{\frac{1}{2}} \quad (\text{A.5})$$

Appendix A. Uncertainty analysis

A.2.3 Input Heat Load

The net heat input Q_{in} was estimated as the mean value of the power supplied by the electrical heater P_{el} and the heat removed by the cooling circuit Q_{out} .

$$Q_{in} = \frac{P_{el} + Q_{out}}{2} \quad (\text{A.6})$$

with an uncertainty measured as:

$$\delta Q_{in} = \left(\left(\frac{1}{2} \cdot \delta(P_{el}) \right)^2 + \left(\frac{1}{2} \cdot \delta Q_{out} \right)^2 \right)^{\frac{1}{2}} \quad (\text{A.7})$$

A.2.4 Thermal resistances

The uncertainty of the overall thermal resistance R_{TOT} (Eq. 3.2) was computed as:

$$\delta R_{TOT} = \left(\left(\frac{1}{Q_{in}} \delta \Delta T \right)^2 + \left(\frac{\Delta T}{Q_{in}^2} \delta Q_{in} \right)^2 \right)^{\frac{1}{2}} \quad (\text{A.8})$$

The uncertainty of the R_{ratio} (Eq. 3.5) was computed as:

$$\delta R_{ratio} = \left(\left(\frac{1}{R_{TOT}} \delta R_{FR=00} \right)^2 + \left(\frac{R_{FR=00}}{R_{TOT}^2} \delta R_{TOT} \right)^2 \right)^{\frac{1}{2}} \quad (\text{A.9})$$

The uncertainty of resistance of the PHP effect defined by Eq. 3.4 was estimated as:

$$\delta R_{PHP} = \left(\left(\frac{1}{\left(\frac{1}{R_{TOT}} - \frac{1}{R_{FR=00}} \right)^2 \cdot R_{TOT}^2} \delta R_{TOT} \right)^2 + \left(\frac{1}{\left(\frac{1}{R_{TOT}} - \frac{1}{R_{FR=00}} \right)^2 \cdot R_{FR=00}^2} \delta R_{FR=00} \right)^2 \right)^{\frac{1}{2}} \quad (\text{A.10})$$

A.2.5 Image Processing

The resolution of the interface tracking processes was estimated to be 1 pixel, resulting in:

$$\begin{cases} \delta z = 0.080 \text{ mm} \\ \delta t = 0.003 \text{ s} \end{cases} \quad (\text{A.11})$$

The uncertainty of the velocity was computed as:

$$\delta u = \left(\left(\frac{1}{\Delta t} \delta z \right)^2 + \left(\frac{\Delta z}{\Delta t^2} \delta \Delta t \right)^2 \right)^{\frac{1}{2}} \quad (\text{A.12})$$

A.2. Uncertainty propagation

Table A.2 reports the uncertainties of the above mentioned quantities computed according to Eq. A.3 - A.12.

Table A.2: Uncertainty of measured quantities

Quantity	Measured uncertainty	
	min	max
P_{el}	1.00 %	
Q_{in}	4.56 %	12.51 %
R_{TOT}	6.64 %	18.7 %
R_{ratio}	6.85 %	18.89 %
R_{PHP}	12.02 %	28.15 %
u	3.00 %	

B Prediction of the heat transfer coefficient

From the analysis of the time-strip data, the time-averaged local heat transfer coefficient was numerically estimated utilizing the mechanistic model proposed by Thome et al. (2004). The *three-zone* flow boiling model takes into consideration the time variation of the heat transfer coefficient $h(z)$ during the passage by the location z of a triplet formed by a liquid slug, an evaporating vapor bubble and a vapor plug. The time-averaged heat transfer coefficient for one period τ was obtained from Eq. B.1:

$$h(z) = \frac{t_l}{\tau} h_l(z) + \frac{t_{film}}{\tau} h_{film}(z) + \frac{t_v}{\tau} h_v(z) \quad (\text{B.1})$$

In Eq. B.1 the local single-phase liquid $h_l(z)$ and vapor $h_v(z)$ heat transfer coefficients were computed utilizing the London and Shah correlation for laminar developing flow:

$$Nu_{lam}(z) = 0.455 \sqrt[3]{Pr} \frac{d_h Re}{L(z)} \quad (\text{B.2})$$

The heat transfer coefficient of the evaporating thin film was computed assuming 1D conduction across the stagnant liquid film:

$$h_{film}(z) = \frac{K_l}{\delta_0 - \delta_{end}} \ln \left(\frac{\delta_0}{\delta_{end}} \right) \quad (\text{B.3})$$

The initial thickness of the liquid film δ_0 was computed according to Eq. B.4 (Aussillous and Quere, 2000):

$$\frac{\delta_0}{d_h} = \frac{(0.67Ca^{(2/3)})}{(1 + 3.35Ca^{(2/3)})} \quad (\text{B.4})$$

The Capillary number defined in Eq. B.5 was computed according to the surface tension σ and the liquid dynamic viscosity μ_l evaluated at the local fluid saturation temperature, and

Appendix B. Prediction of the heat transfer coefficient

the vapor phase velocity .

$$Ca = \frac{\mu_l u_v}{\sigma} \quad (\text{B.5})$$

The vapor phase velocity u_v was computed from the evaporator time-strip data, as described in Section 3.5.1. For the oscillating flows, the time averaged absolute value of the liquid slug was chosen. For circulating semi-annular flows, the velocity of the small liquid slugs periodically appearing in the evaporator was used to compute the velocity of the vapor phase.

The variation of the film thickness was produced by vaporization and its final value δ_{end} depends on whether local dry-out occurs. The latter occurs when the liquid film thickness reaches its minimum, set to be equal to the channel wall surface roughness. Since the channel wall surface roughness could not be measured, as suggested by the model, its value was set to $1 \mu\text{m}$.

The time corresponding to the presence of liquid t_l or vapor t_v ($t_{film} + t_{dry}$) for the period τ was computed at each location z from the thresholding of the time-strip, as described in Section 3.5.1. The residence time of the elongated bubble t_{film} and of dry-out t_{dry} were then computed comparing the actual residence time t_v with the time necessary to evaporate the whole film $t_{dry,film}$ computed from Eq. B.6:

$$t_{dry,film}(z) = \frac{\rho_l \Delta h_{lv}}{q} [\delta_0 - \delta_{min}] \quad (\text{B.6})$$

Bibliography

- B. Agostini, M. Fabbri, J. E. Park, J. Thome, and B. Michel. State of the Art of High Heat Flux Cooling Technologies. *Heat Transfer Engineering*, 28(4):258–281, 2007.
- H. Akachi. Structure of a Heat Pipe, 1990.
- P. Aussillous and D. Quere. Quick deposition of a fluid on the wall of a tube. *PHYSICS OF FLUIDS*, 12(10):2367–2371, 2000.
- A. H. Beitelmal and D. Fabris. Servers and Data Centers Energy Performance Metrics. *Energy and Building*, 2014.
- N. Borhani, B. Agostini, and J.R. Thome. A Novel Time Strip Flow Visualisation Technique for Investigation of Intermittent Dewetting and Dryout in Elongated Bubble Flow in a Microchannel Evaporator. *International Journal of Heat and Mass Transfer*, 53:4809–4818, 2010.
- Q. Cai, R.-l. Chen, and C.-l. Chen. An Investigation of Evaporation, Boiling, and Heat Transfer Performance in Pulsating Heat Pipe. In *ASME Int. Mech. Engineering Congress & Exposition*, pages 99–104, 2002.
- Q. Cai, C. Chen, and J.F. Asfia. Operating Characteristic Investigations in Pulsating Heat Pipe. *Journal of Heat Transfer*, 128(12):1329, 2006. ISSN 00221481.
- P. Charoensawan and P. Terdtoon. Thermal performance of horizontal closed-loop oscillating heat pipes. *Applied Thermal Engineering*, 28(5-6):460–466, April 2008. ISSN 13594311.
- P. Charoensawan, S. Khandekar, M. Groll, and P. Terdtoon. Closed loop pulsating heat pipes Part A: parametric experimental investigations. *Applied Thermal Engineering*, 23:2009–2020, 2003.
- P. Cheng and H. Ma. A Mathematical Model of an Oscillating Heat Pipe. *Heat Transfer Engineering*, 32(11-12):1037–1046, October 2011. ISSN 0145-7632.
- K. H. Chien, Y. R. Chen, Y. T. Lin, C. C. Wang, and K. S. Yang. The Experimental Studies of Flat-Plate Closed-Loop Pulsating Heat. *11th IHPS*, pages 212–216, 2011.

Bibliography

- H. Colleen and S. Stephani. 3M, SGI and Intel showcase advanced cooling technology for the "data center of the future", April 2014.
- S.P. Das, V.S. Nikolayev, F. Lefevre, B. Pottier, S. Khandekar, and J. Bonjour. Thermally induced two-phase oscillating flow inside a capillary tube. *International Journal of Heat and Mass Transfer*, 53(19-20):3905–3913, September 2010. ISSN 00179310.
- S.P. Das, F. Lefevre, S. Khandekar, and J. Bonjour. Thermally Induced Oscillatory Two-Phase Flow in a Mini-Channel Towards Understanding Pulsating Heat Pipes. In *9th International Conference on Nanochannels, and Microchannels*, pages 1–6, 2011.
- R. Dijkstra. Power markets, Power prices & Data centers. Technical report, BroadGroup, 2012.
- R. T. Dobson. Theoretical and experimental modelling of an open oscillatory heat pipe including gravity. *International Journal of Thermal Sciences*, 43:113–119, 2004.
- European Centre for Ecotoxicology. JACC 044 : 1,1,1,3,3-pentafluoropropane (HFC-245fa) (CAS No. 460-73-1). Technical report, European Centre for Ecotoxicology, 2004.
- European Commission. http://ec.europa.eu/europe2020/europe-2020-in-a-nutshell/targets/index_en.html. Last access: 27.6.2014. Technical report, European Commission, 2010.
- M. Giovagnoni. *Analisi delle vibrazioni nei sistemi meccanici*. Edizioni Libreria Cortina, 2001.
- M. Groll and S. Khandekar. Pulsating heat pipes: progress and prospects. In *Proceeding of 3rd International Conference on Energy and Environment, Shanghai, China*, volume 3, pages 1–8, 2003.
- M. Groll and S. Khandekar. State of the Art on Pulsating Heat Pipes. In *Microchannels and Minichannels, Rochester, New York, USA*, 2004.
- V.A. Hemadri and S. Khandekar. Thermal Performance Characterization of Embedded Pulsating Heat Pipe Radiators by Infrared Thermography. In *6th ISMF*, number July, pages 11–15, 2009.
- C. Hohmann and P. Stephan. Microscale temperature measurement at an evaporating liquid meniscus. *Experimental Thermal and Fluid Science*, 26(2-4):157–162, June 2002. ISSN 08941777.
- B. Holley and A. Faghri. Analysis of pulsating heat pipe with capillary wick and varying channel diameter. *International Journal of Heat and Mass Transfer*, 48(13):2635–2651, June 2005. ISSN 00179310.
- D. Japikse. Advanced in thermosyphon technology. *Advances of Heat Transfer*, 9:1–111, 1973.
- Y. Joshi and P. Kumar. *Energy Efficient Thermal Management of Data Centers*. Springer, 2012.

- V.K. Karthikeyan, S. Khandekar, B.C. Pillai, and Pavan K. Sharma. Infrared thermography of a pulsating heat pipe: Flow regimes and multiple steady states. *Applied Thermal Engineering*, 62:470–480, 2014.
- S. Khandekar and M. Groll. On the Definition of Pulsating Heat Pipes: an Overview. In *5th Minsk International Seminar (Heat Pipes, Heat Pumps, Refrigerators)*, volume 3, 2003.
- S. Khandekar and M. Groll. An Insight into Thermo-Hydrodynamic Coupling in Closed Loop Pulsating Heat Pipes. *International Journal of Thermal Sciences*, 43:13–20, 2004.
- S. Khandekar and M. Groll. Insights into the performance modes of closed loop pulsating heat pipes and some design hints. In *18th National & 7th ISHMT-ASME Heat and Mass Transfer Conference, Guwahati, India*, 2006.
- S. Khandekar, M. Groll, P. Charoensawan, and P. Terdtoon. Pulsating heat pipes : Thermo-fluidic characteristics and comparative study with single phase thermosyphon enthalpy. In *12th International Heat Transfer Conference*, volume 4, pages 459–464, 2002a.
- S. Khandekar, M. Schneider, P. Schafer, R. Kulenovic, and M. Groll. Thermofluid dynamic study of flat-plate closed-loop pulsating heat pipes. *Microscale Thermophysical Engineering*, 6(4): 303–318, 2002b.
- S. Khandekar, P. Charoensawan, M. Groll, and P. Terdtoon. Closed loop pulsating heat pipes Part B: visualization and semi-empirical modeling. *Applied Thermal Engineering*, 23:2021–2033, 2003a.
- S. Khandekar, N. Dollinger, and M. Groll. Understanding operational regimes of closed loop pulsating heat pipes: an experimental study. *Applied Thermal Engineering*, 23(6):707–719, April 2003b. ISSN 13594311.
- S. Khandekar, S. Manyam, M. Groll, and M. Pandey. Two-phase flow modeling in closed loop pulsating heat pipes. In *13th IHPC*, volume 6, pages 0–7, 2004.
- S. Khandekar, A. P. Gautam, and P. K. Sharma. Multiple quasi-steady states in a closed loop pulsating heat pipe. *International Journal of Thermal Sciences*, 48(3):535–546, March 2009. ISSN 12900729.
- S. Khandekar, P.K. Panigrahi, F. Lefèvre, and J. Bonjour. Local Hydrodynamics of Flow in a Pulsating Heat Pipe: a Review. *Frontiers in Heat Pipes*, 1:1–20, 2010.
- J.S. Kim, N.H. Bui, J.W. Kim, J.H. Kim, and H.S. Jung. Flow visualization of oscillation characteristics of liquid and vapor flow in the oscillating capillary tube heat pipe. *Journal of Mechanical Science and Technology*, 17(10):1507–1519, 2003.
- S. J. Kline and F. A. McClintock. Describing Uncertainties in Single Sample Experiments. *Mechanical Engineering*, pages 3–8, 1953.

Bibliography

- L. Lin, R. Ponnappant, and Lelandt. Experimental Investigation of Oscillating Heat Pipes. *Journal of Thermophysics and Heat Transfer*, 15(4):395–400, 2001.
- S. Lips, A. Bensalem, Y. Bertin, V. Ayel, C. Romestant, and J. Bonjour. Experimental evidences of distinct heat transfer regimes in pulsating heat pipes (PHP). *Applied Thermal Engineering*, 30(8-9):900–907, June 2010. ISSN 13594311.
- M. Mameli, S. Khandekar, and M. Marengo. Flow Patterns and Corresponding Local Heat Transfer. In *29th National Heat Transfer Conference of Italy*, 2011.
- M. Mameli, M. Marengo, and S. Khandekar. Local heat transfer measurement and thermo-fluid characterization of a pulsating heat pipe. *International Journal of Thermal Sciences*, 75: 140–152, 2014.
- Y. F. Maydanik, V. I. Dmitrin, and V. G. Pastukhov. Compact cooler for electronics on the basis of a pulsating heat pipe. *Applied Thermal Engineering*, 29(17-18):3511–3517, December 2009. ISSN 13594311.
- McKinsey. The Carbon Impacts and Opportunities of Information and Communications. Technical report, The Climate Group, 2008.
- I. Mudawar. Assessment of high-heat-flux thermal management schemes. *IEEE Trans. on Components and Packaging Technologies*, 24:122–141, 2001.
- S. Nishio, S. Nagata, S. Baba, and R. Shirakashi. Thermal performance of SEMOS heat pipes. In *12th International Heat Transfer Conference*, pages 477–482, 2002.
- NIST. NIST Thermodynamic Properties of Refrigerants and Refrigerants Mixtures Data-base. Vers. 8.0. Technical report, Gaithersburg, MD, 2007.
- W. Qu and H.B. Ma. Theoretical analysis of startup of a pulsating heat pipe. *International Journal of Heat and Mass Transfer*, 50:2309–2316, 2007.
- D. Reay, P. Kew, and R. McGlen. *Heat Pipes. Theory, Design and Applications*. Elsevier, 2014.
- D. Sage, D. Prodanov, J.-Y. Tinevez, and J. Schindelin. Making Interoperability Between ImageJ and Matlab Possible. In *ImageJ User & Developer Conference (IUDC'12)*. Mondorf-les-Bains, Grand Duchy of Luxembourg, 2010.
- P. Sakulchangsattajai, P. Chareonsawan, T. Waowaew, P. Terdtoon, and M. Murakami. Mathematical modeling of closed-end pulsating heat pipes operating with a bottom heat mode. *Heat Transfer Engineering*, 29(3):239–254, 2008.
- S. Shafiee and E. Topal. When will fossil fuel reserves be diminished? *Energy Policy*, 37:181–189, 2009.
- G. Spinato, B. d'Entremont N. Borhani, and J. R. Thome. Time Strip Flow Visualization of Flow Patterns in a Closed Loop Pulsating Heat Pipe. In *5th International Conference of Heat Transfer and Fluid Flow in Microscale*, 2014.

- J.R. Thome, V. Dupont, and A. M. Jacobi. Heat transfer model for evaporation in microchannels. Part I: presentation of the model. *International Journal of Heat and Mass Transfer*, 47(14-16): 3375–3385, July 2004. ISSN 00179310.
- B.Y Tong, T.N Wong, and K.T Ooi. Closed-loop pulsating heat pipe. *Applied Thermal Engineering*, 21(18):1845–1862, December 2001. ISSN 13594311.
- U.S. Energy Information Administration. Other Gases: Hydrofluorocarbons, Perfluorocarbons, and Sulfur Hexafluoride. Technical report, U.S. Energy Information Administration, 2003.
- Van P. Carey. *Liquid-Vapor Phase-Change Phenomena: An Introduction to the Thermophysics of Vaporization and Condensation Processes in Heat Transfer Equipment*. Group, Taylor & Francis, 2008. ISBN 978-1591690351.
- S. Wang and S. Nishio. Heat transport characteristics in closed loop oscillating heat pipes. *2005 ASME Summer Heat Transfer Conference, San Francisco, CA*, pages 805–810, 2005.
- World Nuclear Association. Nuclear Power in Germany. Technical report, World Nuclear Association, April 2014.
- G. Xu, S. Liang, and M. Vogel. Thermal characterization of pulsating heat pipes. In *10th Intersociety Conference on Thermal and Thermomechanical Phenomena in Electronic Systems (ITHERM, 60)*, pages 552–556. IEEE, 2006. ISBN 0-7803-9524-7.
- J. L. Xu and X. M. Zhang. Start-up and steady thermal oscillation of a pulsating heat pipe. *Heat and Mass Transfer*, 41(8):685–694, March 2005. ISSN 0947-7411.
- J.L. Xu, Y.X. Li, and T.N. Wong. High Speed Flow Visualization of a Closed Loop Pulsating Heat Pipe. *International Journal of Heat and Mass Transfer*, 48:3338–3351, 2005.
- H. Yang, S. Khandekar, and M. Groll. Operational limit of closed loop pulsating heat pipes. *Applied Thermal Engineering*, 28(1):49–59, January 2008. ISSN 13594311.
- D. Yuan, W. Qu, and T. Ma. Flow and heat transfer of liquid plug and neighboring vapor slugs in a pulsating heat pipe. *International Journal of Heat and Mass Transfer*, 53:1260–1268, 2010.
- Y. Zhang and A. Faghri. Heat transfer in a pulsating heat pipe with open end. *International Journal of Heat and Mass Transfer*, 45:755–764, 2002.
- Y. Zhang and A. Faghri. Advances and Unsolved Issues in Pulsating Heat Pipes. *Heat Transfer Engineering*, 29(1):20–44, December 2008. ISSN 0145-7632.
- J. Zuo, L. R. Hoover, and A. L. Phillips. *Thermal challenges in next generation electronic systems*, chapter An integrated thermal architecture for thermal management of high power electronics. Millpress, 2002.

Curriculum Vitae

Personal information

Name Giulia Spinato
Date of birth November 25th, 1987
Nationality Italian

Education

2012 – 2014 Doctoral Student and Assistant, Laboratory of Heat and Mass Transfer, Swiss Federal Institute of Technology Lausanne (EPFL), Switzerland

2011 Master of Engineering in Mechanical Engineering and Minor in Energy, 5.71/6, Swiss Federal Institute of Technology Lausanne (EPFL), Switzerland

2009 Bachelor of Engineering in Mechanical Engineering, *cum laude*, University of Udine, Italy

Professional Experience

2012 – 2014 Swiss Federal Institute of Technology (EPFL), Laboratory of Heat and Mass Transfer, Lausanne, teaching assistant, research project developments, laboratory activities.

Feb. - Aug. 2011 ABB Switzerland, Corporate Research – Baden Dättwil, internship.

Aug. - Sept. 2010 Swiss Federal Institute of Technology (EPFL), Laboratory for Industrial Energy Systems, Lausanne, internship.

July - Aug. 2008 ENEL Brasil s.r.l., Rio de Janeiro, Brazil, internship.

Journal Publications

1. G. Spinato, N. Borhani, B. d'Entremont and J.R. Thome, Time Strip Flow Visualization of Flow Patterns in a Closed Loop Pulsating Heat Pipe. Submitted for review to *Experimental Thermal and Fluid Science*
2. G. Spinato, N. Borhani, B. d'Entremont and J.R. Thome, Time-Strip Visualization and Thermo-Hydrodynamics in a Closed Loop Pulsating Heat Pipe. Submitted for review to *Applied Thermal Engineering*

Conference Articles

1. G. Spinato, N. Borhani, B. d'Entremont and J.R. Thome, Time Strip Flow Visualization of Flow Patterns in a Closed Loop Pulsating Heat Pipe. *5th International Conference on Heat Transfer and Fluid Flow in Microscale*, April 2014, Marseille-France
2. H. Becker, G. Spinato and F. Marechal, A Multi-Objective Optimization Method to integrate Heat Pumps in Industrial Processes. *21st European Symposium on Computer Aided Process Engineering (ESCAPE-21)*, Chalkidiki, GREECE, Computer-Aided Chemical Engineering, 2011.